Geomechanical characterisation of organic-rich shale properties using small scale experiments and homogenisation methods

Majid Goodarzi

Submitted in fulfillment for the degree of Doctor of Philosophy in the Faculty of Science

School of Engineering
Newcastle University
Newcastle Upon Tyne, UK.
April 2018

Declaration

I hereby certify that this is my own work, except where otherwise acknowledged, and that it has not been submitted for a degree at this, or any other university.

Majid Goodarzi

Abstract

Shale, or mudstone, is the most common sedimentary rock. It is a heterogeneous, multi-mineralic natural composite consisting of clay mineral aggregates, organic matter, and variable quantities of minerals such as quartz, calcite, and feldspar. Determination of the mechanical response of shales through experimental procedures is a challenge due to their heterogeneity and the practical difficulties of retrieving good-quality core samples. Therefore, in recent years extensive research has been directed towards developing alternative approaches for the mechanical characterisation of shale rocks.

In this study, a nanoscale mechanical mapping technique called PeakForce QNM® has been combined with imaging and chemical analysis in order to investigate the mechanical response of each constituent of the shale microstructure. Isotropic elastic behaviour was observed for silt inclusions while a highly anisotropic response was found in the clay matrix. Organic matters with different levels of thermal maturity were investigated and the elastic moduli were determined. These information are essential and useful in order to predict or understand the macroscopic mechanical response of shale rocks. Indentation testing was then carried out in order to scale up the nano-mechanical measurements. This test allows for generating data related to the mechanical behaviour of shale rocks from shale cuttings. Shale samples with a range of mechanical behaviour, from soft to hard, and mineralogical compositions were used in these tests. Issues related to indentation testing such as loading and unloading rate, tip shape and creep behaviour were studied. The capabilities and limitations of this test applied to shale rock were further clarified. Aside from these experimental studies, the Micromechanical modelling (rock physics), a mathematical description of composite-like material, was theoretically and practically studied as an alternative approach for predicting the elastic response of shale rocks. The limitations and the ranges of applicability of the micromechanical formulations were evaluated using direct numerical modelling of shale microstructure. Suitable formulations for homogenisation of shale composite structure were determined. Finally, the data obtained in the nano-scale experiments, as input data, and the results of indentation testing, as the validation data sets, were adopted for these mathematical formulations.

In the last step, numerical modelling of indentation test was undertaken to back-calculate the plastic response of shale samples using the load-displacement curves obtained from this test. The recently developed Material Point Method has been implemented to simulate the large deformation that can occur when pressing the indenter into the shale surface. The non-uniqueness problem of the indentation curve for pressure-sensitive materials was addressed using two different indenter geometries. Inverse analysis was conducted simultaneously until a set of parameters was found matching both experimental curves.

Acknowledgments

First of all, I would like to thank my supervisory team, Dr. Mohamed Rouainia and professor Andrew C. Aplin for giving me this opportunity to pursue my doctoral degree at Newcastle University. During the time of my study, I have always been receiving their support in both scientific and personal issues, particularly Mohamed whom I am still consulting with at my new position. Without them, I would have not been able to conduct this research. They guided me through this study, criticised me constructively, connected me with suitable research partners, kept me in the right direction and gave me the opportunity to express and peruse my research ideas. I would also like to sincerely thank Dr. Pablo Cubillas for providing me with the opportunity to use the AFM laboratory at Durham University and his vital help with the AFM experiments and also Dr. Jingsheng Ma for providing the stochastic model of porous rock. I wish to express my sincere appreciation to Mr. Leon Bowen at Durham University and Mr. Philip Green at Newcastle University for their cooperation and involvement in sample characterisation, preparation and imaging. Aside from these important personnel, I would like to acknowledge all the parties participating in the GASH consortium for providing funding for this research. Moreover, I am grateful to our industrial partners at SGS Horizon BV and Micro Materials LTD for their enormous help with indentation tests.

Finally, I want to thank my best friends who have been an important part of my life during this study, Ciprian B. Spatar, Thomas Rexer, Seyedhamid Karimi, Reza Amozgar and Hossein Mahdavinezhad. No word can express my deep gratitude for what my family, particularly my wife Banafsheh, has done for me and the support that I have received all these years, and for that I am always grateful for their unconditional love and support.

Contents

List of Figures

List of Tables

Chapter 1

General introduction and objectives

1.1 Background

Mudstone is the most abundant sedimentary rock and forms almost 70% of sedimentary basins (Aplin and Macquaker, 2011). The sudden increase in the oil/gas price in the past couple of years has significantly accelerated research interest in these rocks due to the possibility of directly exploiting oil/gas from these sediments (Alexander, 2011; Bowker, 2007). In parallel, the recent concept of carbon capture and storage (CCS) has added another boost to the research communities on shale rocks. Briefly, the CCS process consists of capturing waste CO_2 from major CO_2 production sources such as fossil fuel power plants, and storing it in geological formations with the aim of preventing large amount of CO_2 from being released into the atmosphere. The sealing capacities of shale deposits has made the storage of captured CO_2 in certain formations possible (Khosrokhavar *et al.*, 2014; Watts, 1987). In addition, shale rocks contain important information related to the geological and environmental conditions of their deposition time (Macquaker, 1994).

Shale rock formations are highly heterogeneous and the variability in both composition and origin of the sediments can be seen spatially and vertically. This heterogeneity propagates to a much smaller scale of a few nanometers (Aplin and Macquaker, 2011). In fact, the shale rock can be defined as a multi-mineralic natural composite consisting of clay mineral aggregates, organic matter, and variable quantities of minerals such as quartz, calcite, and feldspar. Although this variability was initially controlled by sedimentation conditions, they could be altered during diagenesis (Pedersen and Calvert, 1990). For example, bacterial activity may result in the dissolution of some minerals along with the precipitation of new ones (Curtis, 1995; Macquaker *et al.*, 2014). The continuous process of sedimentation increases the depth of layers and consequently their pressures and temperatures. More mineral transformation and textural change can be induced under these conditions. High pressure in the sediments can significantly compact the muds and reduce their porosity.

Considering shale formations either as a cap rock for carbon capture and storage or as an unconventional oil/gas resource requires comprehensive petrophysical characterisation of the formation. Part of this characterisation consists of the mechanical response of the rock. This is considered to be highly important for well-bore stability, hydraulic fracturing and the estimation of the sealing capability of the rock. However, the heterogeneity of the mudstone, hinders a reliable characterisation and the rapid change in mineral compositions and porosity in shale layers significantly changes the mechanical response. Another factor which contributes to the complexity of the mechanical behaviour, is the organic matter. The relatively soft response of this component and their lens shape can be very influential on the mechanical properties of shales (Vernik and Nur, 1992; Ortega *et al.*, 2009; Vernik and Milovac, 2011). Furthermore, compared to other types of rocks, it is even more difficult to retrieve core samples with good quality from shale layers in order to conduct conventional mechanical tests. This is partly due to the chemical and mechanical instability of shales (Kumar *et al.*, 2012). Even in-situ methods, such as well sonic log, are incapable of accurately capturing the mechanical properties in the direction parallel to the well axis (Abousleiman *et al.*, 2009).

The above mentioned challenges have motivated researchers to design alternative methods to estimate the mechanical response of shale rocks. One approach towards the characterisation of shale rocks is to adopt small scale experiments on shale cuttings, which are widely available. The instrumented indentation test, which has been used in many engineering applications for the characterisation of the mechanical response of materials at small scale, has also been recently adopted in the shale industry. In this test, a sharp indenter is pushed into the material surface and the load-displacement response is used to estimate the elastic and plastic properties of the material (Oliver and Pharr, 1992, 2004; Mondal *et al.*, 2007; Dean *et al.*, 2013; Epshtein *et al.*, 2015). The speed and simplicity of this technique have made it an interesting tool. On the other hand, the strong correlation between shale behaviour and their mineralogical composition was the main motivation behind the attempts to relate the micro and macroscopic behaviour to nano-scale compositions. From this perspective, shales were assumed to be a composite material and mathematical correlations have been established to connect macroscale to microscale (Hornby *et al.*, 1994; Jakobsen *et al.*, 2003; Ortega *et al.*, 2007, 2010; Sayers, 2013a). These mathematical relations between the macro and micro scales are generally known as homogenisation methods, which have been widely adopted in composite and material engineering (Hill, 1965; Mori and Tanaka, 1973; Zaoui, 2002). In this framework, the shale is assumed to be a composite formed of a porous clay along with several silt mineral inclusions. The porous clay plays the role of a background matrix which engulfs all the silt mineral inclusions, which have random spatial and orientational distributions (Abou-Chakra Guery *et al.*, 2010; Goodarzi *et al.*, 2016). This definition of the shale matrix, which only refers to the porous clay phase and will be used in this study as well, is slightly different from some studies, in which the whole microstructure of shale is called the shale matrix (eg. Ettehadtavakkol and Jamali, 2016; Davudov and Moghanloo, 2017). In addition, the porous clay is also assumed to be a composite consisting of clay particles, pores and in some cases organic matter (see e.g. Chapter 4). The clay particles are also referred to as the solid unit of clay in some studies, as it is claimed that this unit is an agglomerate of clay particles rather than a single particle (e.g. Babko and Ulm (2008)). In the following, both terms, solid unit of clay and clay particle, are used and they can be considered the same unless otherwise is expressly stated.

The indentation test was implemented in the shale industry to solve the problem of a shortage of intact core samples. Ulm and Abousleiman (2006), Babko and Ulm (2008), Abousleiman *et al.* (2009) and Kumar *et al.* (2012, 2015) undertook indentation tests on shale cuttings prepared parallel and perpendicular to the bedding direction. For some samples the elastic modulus results were compared with the Ultra-sonic Pulse Velocity (UPV) test obtained on core samples and good agreement was observed. This can be justified with the fact that the elastic deformation in this test is relatively small, compared to core sample mechanical testings, therefore the obtained elastic moduli are therefore comparable with dynamic (acoustic) elastic properties. The high accuracy of the indentation test allows for very small penetration (e.g. 100 nm) allowing different constituents of a composite to be separately evaluated (Constantinides and Ulm, 2007, 2013; DeJong and Ulm, 2007; Epshtein *et al.*, 2015). In order to provide better understanding of the mechanical response of the shale's clay matrix, Babko and Ulm (2008) tested shale samples using very small penetrations. Other researchers adopted the same strategy to solve the challenging properties of organic matter (Zeszotarski *et al.*, 2003; Zargari *et al.*, 2013). Abedi *et al.* (2016) tried to combine a grid-based indentation test with Energy-dispersive X-ray spectroscopy imaging to generate a micron-scale mechanical map of the shale microstructure. Using indentation testing on heterogeneous materials to estimate properties of different phases may violate the assumption of infinite half-space beneath the indenter required in the interpretation of indentation results.

Very recently, a non-destructive technology has been introduced, known as Peak Force Quantitative Nano-mechanical Mapping® (QNM), in which a nanoscale tip is used to extract the elastic response at the resolution of a few nanometers (Trtik *et al.*, 2012). This new method provides the opportunity to better evaluate the mechanical response of problematic constituents such as organic matter (Eliyahu *et al.*, 2015, Emmanuel *et al.*, 2016a, 2016b; Goodarzi *et al.*, 2017). Despite all these efforts, there is still the need for more studies in order to reach a better understanding of the accuracy, limitations and capabilities of these methods. In addition, the relationship between the obtained elastic properties in this technique with the static and dynamic elastic moduli measured on core samples has to be evaluated.

The homogenisation technique, or effective-medium modelling, is a mathematical description, in which the macroscopic response of a composite is defined as a function of the properties and the volume fractions of the constituents and their interactions with each other. The difference between several existing homogenisation formulations originates in the assumptions and simplifications that have to be made about the constituent's properties, shape and interactions in order to derive the solution. This approach was initially adopted for shale rocks in a study by Hornby *et al.* (1994). They investigated shale as a two level composite. In the first level, there are clay particles and voids (normally filled with water) which form a porous matrix and homogenisation was performed on these phases to estimate the elastic constants of the porous clay. In the second level, mineral inclusions, such as carbonate and quartz, are distributed through this porous medium representing the shale's matrix. In order to reproduce the anisotropy of shale rocks, the assumption of an elliptical shape for clay particles was considered. Several studies adopted the same assumptions and improved it by including the organic matter into the shale microstructure. For instance, in some studies, kerogen was considered as elliptical inclusions in the shale structure (Zhu *et al.*, 2012; Qin *et al.*, 2014), and others combined kerogen with clay particles to form the initial constituent of porous clay (Ortega *et al.*, 2009; Li *et al.*, 2015). Some studies also proposed that kerogen be considered as the main background matrix for the shale microstructure (Vernik and Landis, 1996; Bayuk *et al.*, 2008). It can be seen that no general approach was proposed. Aside from using different assumptions on the role of kerogen in shale microstructure, different values for the elastic modulus of the kerogen constituent have also been adopted in these studies. The clay properties and their shape were also not unique and generally accepted (Jakobsen *et al.*, 2003; Vasin *et al.*, 2013; Sayers, 2013a; Guo *et al.*, 2014; Goodarzi *et al.*, 2017). For instance, Ortega *et al.* (2007) observed a significant anisotropy in the porous clay matrix, which has a reverse correlation with its porosity. They concluded that the clay particles are intrinsically anisotropic, unlike Hornby *et al.* (1994) who assumed that clay particles are isotropic.

Three main issues emerge from a detailed review of studies which have dealt with homogenisation methods for shale rocks. First, suitable homogenisation formulations for shale microstructure are not well established, which is partly due to the fact that shale microstructure is too complex to be described by the simplified models that have been assumed in homogenisation techniques. This fact can be seen in some three dimensional scans of shale microstructure (Kanitpanyacharoen *et al.*, 2011; Chalmers *et al.*, 2012; Vasin *et al.*, 2013; Chen *et al.*, 2015). Second, the mechanical response of clay particles, as the most important elementary building block of shale, is not well constrained. Third, the role and properties of the organic matter in shale microstructure are not well quantified. These two latter problems are expected as neither clay particles nor kerogen can be found in large scale in order to determine their properties by direct conventional measurement techniques. In fact, homogenisation itself is widely used as an indirect method to back-calculate clay parameters from large scale measurements such as UPV test on shale core samples or clay-water mixture (Hornby *et al.*, 1994; Ortega *et al.*, 2007). On the other hand, there are almost generally accepted elastic parameters for shale mineral inclusions such as carbonate, quartz and pyrite which are obtained using conventional mechanical tests on macro-scale samples (Mavko *et al.*, 2009).

Almost all of the studies, previously discussed, have been focused on the elastic response of shale rocks. However, engineering practice, such as hydraulic fracturing or CCS, requires information regarding the elastoplastic response of shale rocks. From the limited studies on core samples, it is well established that shales are elastically anisotropic. The compressional strength is found to be almost identical in both parallel and perpendicular to bedding direction but this will reduce if the loading is inclined due to weak bedding planes (Ewy *et al.*, 2010; Cho *et al.*, 2012; Meier *et al.*, 2015). An attempt to adopt the homogenisation technique for the plastic behaviour of shales has been carried out by a few researchers (Abou-Chakra Guery *et al.*, 2008a, 2008b; Lin *et al.*, 2012; Shen *et al.*, 2012, 2013). In order to achieve a closed form solution, they assumed the shale response to be isotropic in both elastic and plastic states, which significantly deviates from the real behaviour. In addition, the pores have to be assumed as spherical isolated voids, which is not the case for the porosity in shale rocks (see e.g. Goodarzi *et al.*, 2016). Another way is to use the indentation test to obtain information about plastic material parameters. This requires a numerical modelling tool to simulate the indentation test, as has already been widely used in material engineering (Lee *et al.*, 2010; Rauchs and Bardon, 2011; Sarris and Constantinides, 2013). A problem with this approach is that for pressure-sensitive materials, such as soils and rocks, having a minimum of two plasticity parameters, cohesion and angle of internal friction, the indentation curve is not unique and infinite combinations of the plastic parameters can produce the same load-displacement curve (Tho *et al.*, 2004). Some studies attempted to address this problem using different indenter geometries thus creating different load-displacement curves (Min *et al.*, 2004). Promising results have been reported by Seltzer *et al.* (2011) on ceramic materials; however, to the best of the author's knowledge, the applicability of this method in the field of shale rocks has never been investigated.

1.2 Motivation, objectives and thesis structure

The main motivation of this PhD study can be summarised as the investigation of the feasibility of using shale cuttings to enable a greater understanding of the mechanical response of shales. Different shale samples with a wide range of porosity, mineralogical compositions, and organic matter content have been selected for this purpose. A series of experiments including shale characterisation, nano-scale mechanical tests and indentation tests have been conducted. Moreover, a comprehensive theoretical and numerical modelling work has been considered that includes a detailed investigation of homogenisation techniques and their application to shale along with numerical simulations of the indentation test. The scope of this study is considered in the range of experiments and techniques that are also available for industries in order to produce attractive ideas and approaches for the related industries. The results generated within this thesis are expected to greatly contribute to the topic of the mechanical characterisation of shale layers, which is considered to be of high importance for shale oil/gas and carbon capture and storage projects.

The objectives of the thesis can be summerised in four major steps:

1- Nano-scale direct mechanical experiments on shale's microstructure in order to expand our understanding on the in situ mechanical behaviour of each single constituents.

2- Conducting comprehensive indentation test on different well-characterised shale samples. The aim of these experiments was to assess the capabilities and limitations of indentation method in shale rocks and to highlight the major gap that needs to be filled within the literature. In addition, a reliable data set could be generated for the next steps.

3- Theoretical and practical evaluation of micromechanical (Rock physics) modelling in order to be used as a alternative or auxiliary approach for shale mechanical characterisation. Determination of the accuracy and the range of applicability for this approach.

4- Evaluating the possibility of using numerical simulation of indentation test for characterising elastoplastic behaviour of shale rocks. A robust numerical tool should be developed for this purpose.

The thesis is structured in four main chapters from Chapter 2 to 5. Each main chapter covers one of the objectives and consists of an introduction, which provides a detailed background of the topic along with the current literature, and contains a discussion and summary highlighting the key findings. Finally, a conclusion with a summary of all the findings from each chapter and suggestions for some areas of future work is provided.

In Chapter 2, the focus is on nano-scale mechanical mapping of shales. The novel method of PeakForce QNM® is adopted in this study. Several samples with organic content and different maturity levels have been selected. Thin sections were prepared parallel and perpendicular to the bedding direction. The mechanical response of the clay matrix and mineral inclusions were studied in both directions. Then, the organic matter was analysed in order to generate high quality measured data for the elastic modulus of this constituent. During the mechanical mapping, the sample's surfaces were also scanned using imaging and chemical analysis techniques, in order to accurately correlate the measured mechanical properties to their corresponding constituents.

In Chapter 3, the scale of measurement was increased in order to study the mechanical response of the whole shale microstructure using the indentation test for this purpose. The same samples used in the previous chapter were first characterised in terms of their mineralogical compositions and porosity. Extensive indentation tests were then conducted on these samples, under different conditions and tip geometries. Issues related to indentation testing on shale samples were highlighted and the capabilities and limitations of this test were evaluated.

In Chapter 4, homogenisation techniques applied to shale rocks are considered. A detailed explanation of the basis of these methods was provided. Numerical modelling has then been undertaken on simplified shale microstructures in order to demonstrate the performance of the different homogenisation formulations [1]. The most suitable formulation was identified and used in conjunction with the experimental results obtained in Chapters 2 and 3 to predict the elastic response of the shale samples. The performance of the homogenisation method in predicting the elastic constants of shale rocks was evaluated using the available data in literature along with the data sets obtained in this work [2] [3].

In Chapter 5, the elastoplastic behaviour of shale was investigated at the scale of a few microns. The load-displacement curves obtained from the indentation tests conducted with both

---

[1] Goodarzi M., Rouainia M., Aplin A.C. 2016. Numerical evaluation of mean-field homogenisation methods for predicting shale elastic response. *Computational Geoscience*.

[2] Goodarzi M., Rouainia M., Aplin A.C., Cubillas P., de Block M. 2017. Predicting the elastic response of organic-rich shale using nanoscale measurements and homogenisation methods. *Geophysical Prospecting*.

[3] Goodarzi M., Rouainia M., Aplin A.C., Cubillas P. 2016. Multiscale study on elastic response of organic-rich Shale. Fifth EAGE Shale Workshop: Quantifying Risk and Potential, 2-4 May, Catania, Italy.

the sharp edge Berkovich and the spherical indenters were considered. A numerical tool was developed to simulate the indentation test involving frictional contact and large deformations in the body mass [4]. A computer code was developed based on the novel material point method (MPM) and used to simulate indentation tests from which the elastic parameters of the samples were directly extracted. In addition, an inverse analysis was conducted in order to back calculate the plastic material parameters of the samples by comparing the numerical load-displacement responses with the experimental results obtained using both Berkovich and the spherical indenters.

---

[4] Goodarzi M., Rouainia M. 2017. Modelling slope failure using a quasi-static MPM with a non-local strain softening approach. *Procedia Engineering*, **175**, 220-225.

References

Abedi S., Slim M., Hofmann R., Bryndzia T., Ulm F.J. 2016. Nanochemo-mechanical signature of organic-rich shales: a coupled indentation–EDX analysis. *Acta Geotechnica*.

Abou-Chakra Guery A., Cormery F., Shao F., Kondo D. 2010. A comparative micromechanical analysis of the effective properties of a geomaterial: effect of mineralogical compositions. *Computers and Geotechniques*, **37**, 585-593.

Abou-Chakra Guery A., Cormery F., Shao J.F., Kondo D. 2008a. A micromechanical model of elastoplastic and damage behavior of a cohesive geomaterial. *International Journal of Solids Structure*, **45**(5), 1406-1429.

Abou-Chakra Guery A., Cormery F., Shao J.F., Kondo D. 2008b. A micromechanical model for the elasto-viscoplastic and damage behavior of a cohesive geomaterial. Physics and Chemistry of the Earth, Parts A/B/C, **33**(1), S416-S421.

Abousleiman Y., Tran M., Hoang S., Ortega J.A., Ulm F.J. 2009. Geomechanical field characterization of the two prolific U.S. mid-West gas plays with advanced wire-line logging tools. SPE Annual technical conference and exhibition, New Orleans, Louisiana, USA. SPE 124428.

Aplin A.C., Macquaker H.S. 2011. Mudstone diversity: Origin and implications for source, seal, and reservoir properties in petroleum systems. *Association of Petroleum Geologists Bulletin*, **95**, 2031-2059.

Alexander T. 2011. Shale gas revolution. *Oilfield review*, **23**, 40-55.

Bayuk I.O., Ammerman M., Chesnokov E.M. 2008. Upscaling of elastic properties of anisotropic sedimentary rocks. *Geophysical Journal International*, **172**, 842–860.

Bobko C., Ulm F.J. 2008 The nano-mechanical morphology of shale. *Mechanics of Material*, **40**, 318-337.

Bowker K.A. 2007. Barnett Shale gas production, Fort Worth Basin: Issues and discussion. *American Association of Petroleum Geologists Bulletin*, **91**, 523-533.

Chalmers G.R., Bustin R.M., Power I.M. 2012. Characterization of gas shale pore systems by porosimetry, pycnometry, surface area, and field emission scanning electron microscopy/transmission electron microscopy image analyses: examples from the Barnett, Woodford, Haynesville, Marcellus and Doig units. *The American Association of Petroleum Geologists Bulletin*, **96**(6), 1099-1119.

Chen L., Zhang L., Kang Q., Viswanathan H.S., Yao J., Tao W. 2015. Nanoscale simulation of shale transport properties using the lattice Boltzmann method: permeability and diffusivity.

Scientific Reports, **5**(8089).

Cho J.W., Kima H., Jeon S., Min K.B. 2012. Deformation and strength anisotropy of Asan gneiss, Boryeong shale, and Yeoncheon schist. *International Journal of Rock Mechanics and Mining Sciences*, **50**, 158-169.

Constantinides G., Ulm F.J. 2007. The nanogranular nature of C-S-H. *Journal of the Mechanics and Physics of Solids*, **55**, 64-90.

Constantinides G., Ulm F.J. 2013. On the use of nanoindentation for cementitious materials. *Materials and Structures*, **36**, 191-196.

Curtis C.D. 1995. Post-depositional evolution of mudstones l: early days and parental influences. *Journal of the Geological Society*, **152**, 577-586.

Davudov D., Moghanloo R.G. 2017. Scale dependent pore and hydraulic connectivity of shale matrix. *Energy Fuels*.

Dean J., Bradbury A., Aldrich-Smith G., Clyne T.W. 2013. A procedure for extracting primary and secondary creep parameters from nanoindentation data. *Mechanics of Materials*, **65**, 124-134.

DeJong M., Ulm F.J. 2007. The nanogranular behavior of C-S-H at elevated temperatures (up to 700 C). *Cement and Concrete Research*, **37**, 1-12.

Eliyahu M., Emmanuel S., Day-Stirrat R.J., Macuulay C. 2015. Mechanical properties of organic matter in shales mapped at the nanometer scale. *Marine and Petroleum Geology*, **59**, 294-304.

Emmanuel S., Eliyahu M., Day-Stirrat R.J., Hofmann R., Macaulay C.I. 2016a. Impact of thermal maturation on nano-scale elastic properties of organic matter in shales. *Marine and Petroleum Geology*, **70**, 175-184.

Emmanuel S., Eliyahu M., Day-Stirrat R.J., Hofmann R., Macaulay C.I. 2016b. Softening of organic matter in shales at reservoir temperatures. *Petroleum Geoscience*.

Epshtein S.A., Borodich F.M., Bull S.J., 2015. Evaluation of elastic modulus and hardness of highly inhomogeneous materials by nanoindentation. *Applied Physics A*, **119**, 325-335.

Ettehadtavakkol A., Jamali A. 2016. Measurement of shale matrix permeability and adsorption with canister desorption test. *Transport in Porous Media*, **114**(1), 149-167.

Ewy R.T., Bovberg C.A., Stankovic R.J. 2010. Strength anisotropy of mudstones and shales. 44^{th} US Rock Mechanics Symposium and 5^{th} U.S.-Canada Rock Mechanics Symposium, held in Salt Lake City, UT June 27-30.

Goodarzi M., Rouainia M., Aplin A.C. 2016. Numerical evaluation of mean-field homogenisation methods for predicting shale elastic response. *Computational Geoscience*.

Goodarzi M., Rouainia M., Aplin A.C., Cubillas P., de Block M. 2017. Predicting the elastic response of organic-rich shale using nanoscale measurements and homogenisation methods. *Geophysical Prospecting*.

Guo Z.Q., Li X.Y., Liu C. 2014. Anisotropy parameters estimate and rock physics analysis for the Barnett Shale. *Journal of Geophysics and Engineering*, **11**(6), 065006.

Hill R. 1965. A self-consistent mechanics of composite materials. *Journal of Mechanics and Physics of Solids*, **13**, 213-222.

Hornby B.E., Schwartz L., Hudson J. 1994 Anisotropic effective medium modeling of the elastic properties of shales. *Geophysics*, **59**, 1570-83.

Jakobsen M., Hudson J.A., Johansen T.A. 2003. T-matrix approach to shale acoustics. *Geophysical Journal International*, **154**, 533-558.

Kanitpanyacharoen W., Wenk H.R., Kets F., Lehr C. and Wirth R. 2011. Texture and anisotropy analysis of Qusaiba shales. *Geophysical Prospecting*, **59**, 536-556.

Khosrokhavar R., Griffiths S., Wolf K.H. 2014. Shale gas formations and their potential for carbon storage: opportunities and outlook. *Environmental Processes*.

Kumar V., Sondergeld C.H., Rai C.S., 2012. Nano to macro mechanical characterization of shale. SPE Annual technical conference and exhibition, San Antonio, Texas, USA. SPE 159804.

Kumar V., Sondergeld C., Rai C.S. 2015. Effect of mineralogy and organic matter on mechanical properties of shale. *Interpretation*, **3** (3), SV9-SV15.

Lee J.H., Kim T., Lee H. 2010. A study on robust indentation techniques to evaluate elastic–plastic properties of metals. *International Journal of Solids and Structures*, **47**, 647-664.

Li Y., Guo Z.Q., Liu C., Li X.Y., Wang G. 2015. A rock physics model for the characterization of organic-rich shale from elastic properties. *Petroleum Science*, **12**, 264-272.

Lin J., Xie S.Y., Shao J.F., Kondo D. 2012. A micromechanical modeling of ductile behavior of a porous chalk: Formulation, identification, and validation. *International Journal for Numerical and Analytical Methods in Geomechanics*, **36**, 1245-1263.

Macquaker J.H.S. 1994. A lithofacies study of the Peterborough Member, Oxford Clay Formation (Jurassic), UK: an example of sediment bypass in a mudstone succession. *Journal of the Geological Society of London*, **151**, 161-172.

Macquaker J.H.S., TAYLOR K.G., KELLER M., POLYA D. 2014. Compositional controls on early diagenetic pathways in fine-grained sedimentary rocks: Implications for predicting unconventional reservoir attributes of mudstones. *American Association of Petroleum Geologists Bulletin*, **98**, 587-603.

Mavko G., Mukerji T., Dvorkin J. 2009. The rock physics handbook. Cambridge University Press.

Meier T., Ryback E., Backers T., Dresen G. 2015 Influence of Bedding Angle on Borehole Stability: A Laboratory Investigation of Transverse Isotropic Oil Shale. *Rock Mechanics and Rock Engineering*, **48**(4), 1535-1546.

Min L., Wei-min C., Nai-gang L., Ling-Dong W. 2004. A numerical study of indentation using indenters of different geometry. *Journal of Material Research*, **19**(1), 73-78.

Mori T., Tanaka K. 1973. Average stress in matrix and average elastic energy of materials with misfitting inclusions. *Acta Metallurgica*, **21**.

Mondal P., Shah S.P., Marks L. 2007. A reliable technique to determine the local mechanical properties at the nanoscale for cementitious materials. *Cement and Concrete Research*, 37, 1440-1444.

Oliver W.C., Pharr G.M. 1992. An improved technique for determining hardness and elastic modulus using load and displacement sensing indentation experiments. *Journal of Materials Research*, **7**, 1564-83.

Oliver W.C., Pharr G.M. 2004. Measurement of hardness and elastic modulus by instrumented indentation: advances in understanding and refinements to methodology. *Journal of Materials Research*, **19**(1), 3-20.

Ortega J.A., Ulm F.J., Abousleiman Y.N. 2007. The effect of the nanogranular nature of shale on their poroelastic behavior. *Acta Geotechnica*, **2**, 155-182.

Ortega J.A., Ulm F.J., Abousleiman Y. 2009. The nanogranular acoustic signature of shale. *Geophysics*, **74**(3), D65-D84.

Ortega J.A., Ulm F.J., Abousleiman Y. 2010. The effect of particle shape and grain-scale properties of shale: A micromechanics approach. *International Journal of Numerical and Analytical Method in Geomechanics*, **34**, 1124-1156.

Pedersen T.F., Calvert S.E. 1990. Anoxia vs. Productivity: What controls the formation of organic-carbon-rich sediments and sedimentary rocks?. *American Association of Petroleum Geologists Bulletin*, **74**, 454-466.

Qin X., Han D., Zhao L. 2014. Rock physics modeling of organic-rich shales with different maturity levels. *SEG Technical Program Expanded Abstracts*, 2952-2957.

Rauchs G., Bradon J. 2011. Identification of elasto-viscoplastic material parameters by indentation testing and combined finite element modelling and numerical optimization. *Finite Elements in Analysis and Design*, **47**, 653-667.

Sarris E., Constantinides G. 2013. Finite element modeling of nanoindentation on C–S–H:

Effect of pile-up and contact friction. *Cement and Concrete Composites*, **36**, 78-84.

Sayers C.M. 2013a. The effect of anisotropy on the Young's moduli and Poisson's ratios of shales. *Geophysical Prospecting*, **61**, 416-426.

Sayers C.M. 2013b. The effect of kerogen on the elastic anisotropy of organic-rich shales. *Geophysics*, **78**(2), D65-D74.

Seltzer R., Cisilino A.P., Frontini P.M., Mai Y.W. 2011. Determination of the Drucker–Prager parameters of polymers exhibiting pressure-sensitive plastic behaviour by depth-sensing indentation. *International Journal of Mechanical Sciences*, **53**, 471-478.

Shen W.Q., Shao J.F., Kondo D., Gatmiri B. 2012. A micro–macro model for clayey rocks with a plastic compressible porous matrix. *International Journal of Plasticity*, **36**, 64-85.

Shen W.Q., Kondo D., Dormieux L., Shao J.F. 2013. A closed-form three scale model for ductile rocks with a plastically compressible porous matrix. *Mechanics of Materials*, **59**, 73-86.

Tho K.K., Swaddiwudhipong S., Liu Z.S., Zeng K., Hua J. 2004. Uniqueness of reverse analysis from conical indentation tests. *Journal of Material Research*, **19**(8), 2498-2502.

Trtik P., Kaufmann J., Udo V. 2012. On the use of peak-force tapping atomic force microscopy for quantification of the local elastic modulus in hardened cement paste. *Cement and Concrete Research*, **42**, 215-221.

Ulm F.J., Abousleiman Y. 2006. The nanogranular nature of shale. *Acta Geotechnica*, **1**, 77-88.

Vasin R.N., Wenk H.R., Kanitpanyacharoen W., Matthies S., Wirth R. 2013. Elastic anisotropy modeling of Kimmeridge shale. *Journal of Geophysical Research: Solid Earth*, **118**, 3931-3956.

Vernik L., Milovac J. 2011. Rock physics of organic shales. *The Leading Edge*, **30**, 318-323.

Vernik L., Nur A. 1992. Ultrasonic velocity and anisotropy of hyrdocarbon source rocks. *Geophysics*, **57**(5), 727-735.

Watts N.L. 1987. Theoretical aspects of cap-rock and fault seals for single- and twophase hydrocarbon columns. *Marine and Petroleum Geology*, **4**, 274-307.

Zargari S., Prasad M., Mba K.C., Mattson E.D. 2013. Organic maturity, elastic properties, and textural characteristics of self resourcing reservoirs. *Geophysics*, **78**(4), D223–D235.

Zaoui, A. 2012. Continuum micromechanics: survey. *Journal of Engineering Mechanics*, **128**(8), 808-816.

Zeszotarski J.C., Chromik R.R., Vinci R.P., Messmer M.C., Michels R., Larsen J.W. 2004. Imaging and mechanical property measurements of kerogen via nanoindentation. *Geochimica et Cosmochimica Acta*, **68**, 4113-4119.

Zhu Y., Xu S., Payne M., Martinez A., Liu E., Harris C., Bandyopadhyay, K. 2012. Improved rock-physics model for shale gas reservoirs. 82nd SEG Meeting Expanded Abstracts 0927.

Chapter 2

Nanoscale mechanical mapping of shales using PeakForce QNM$^{\circledR}$ test

2.1 Introduction

The strong correlation between the macroscopic elastic response and yield strength of mudrocks with their compositions have been widely observed in different experimental studies (Sone and Zoback, 2013a, 2013b; Rybacki *et al.*, 2015). These observations suggest that the overall mechanical behaviour of these natural nano-composite materials originates from their different constituents and also their microstructure. Therefore, obtaining data on the mechanical response of these rocks at submicron scale could pave the way to better understand or predict the macroscale behaviour.

Shale rocks' constituents range from few microns to few nanometers. Some of these components such as quartz, calcite and pyrite grains can be found in larger scale, which makes it possible to adopt conventional rock mechanics tests to extract their mechanical properties. On the other hand, organic matter presents in a scale of few nano to few microns in intergranular pore space. Thus, their mechanical behaviour is poorly constrained. The same problem also exists for the solid unit of porous clay which makes it almost impossible to conduct direct mechanical measurement on it. Most of the studies so far have used nanoindentation test to observe the micromechanical response of shale rocks. The statistical analysis of the extracted data through the nanoindentation test with the resolution of few microns, can only define the shale microstructure as a softer and a stiffer phases. The softer phase can be attributed to the mixture of organic matter and porous clay. However, the stiffer phase is related to the response of all types of silt mineral grains in shale microstructure (Ulm and Abousleiman, 2006; Babko and Ulm, 2008). Few researchers also tried to target a big piece of organic matter and conduct nanoindentation tests on it (Zeszotarski *et al.*, 2004; Ahmadov *et al.*, 2009; Zargari *et al.*, 2013). Theoretically, this measurement might have error due to the fact that the organic matter size is not big enough to satisfy the assumption of infinite half-space, which is used in the derivation of the equations of indentation test.

The recently developed mode of the atomic force microscopy (AFM) technique, called PeakForce Quantitative Nanomechanical Mapping®, provides this possibility to obtain data related to the Young's modulus on a material surface. In this test, an AFM probe is tapped over the surface and the elastic response of the sample is extracted using the generated force-separation curve (Pittenger *et al.*, 2010). The resolution of data extraction depends on the probe tip radius, which is usually around few nanometers. Unlike the nanoindentation test, the PeakForce QNM® is a non-destructive test with much higher resolution. Young *et al.* (2011) conducted several measurements of Young's modulus on different polymers and compared the results with the elastic modulus obtained by indentation test. Their study confirmed the reasonable capability and accuracy of this new method. Trtik *et al.* (2012) adopted this technique to map the local elastic modulus in hardened cement paste. A clear image of Young's modulus with a resolution of much smaller than the size of constituents was generated, which was also compatible with the observed phases in back-scattered electron (BSE) imaging. The same approach was applied on a shale thin section by Eliyahu *et al.* (2015) and Emmanuel *et al.* (2016a, 2016b). Different components of shale including relatively softer areas which were defined with Young's moduli less than 25 GPa, clay matrix, and quartz and pyrite grains, were distinguishable on the Young's modulus map. However, the absolute values obtained on stiff grains did not matched with the well-known properties frequently reported in literature (Lide, 2004). They justify these differences with the limitation in the reliable range of the adopted AFM tip. Additionally, the softer areas, detectable with low values of Young's modulus (<25 GPa), were considered to be related to organic matter, based on carbon analysis on the target area. It is worth noting that the induced elastic deformation in this test is quite small as it is a non-destructive test; therefore, it can be said that the measured Young's modulus could be correlated with the value obtained by dynamic (acoustic) testing.

In this paper, a comprehensive study on the elastic response of shale microstructure will be conducted using the PeakForce QNM®. The Young's modulus map of shale will be generated parallel and perpendicular to bedding direction, which provides valuable data on the origin of macroscopic anisotropy. The mechanical response of slit inclusions will also be observed by several measurements on different grains. Additionally, different shale samples will be tested with the main objective of constraining the mechanical response of organic matter. All the target areas for mechanical measurement will be mapped by back-scattered electron (BSE) imaging and energy dispersive X-ray spectroscopy (EDS), to more confidently correlate the measured moduli to their corresponding constituents. This study can provide further critical data required for rock physics modelling of shales.

2.2 PeakForce Quantitative Nanomechanical Mapping®

Since shales are mainly formed of particles ranging in size from smaller than 1 microns to a few tens of microns (see Figure 2.1), a high resolution technique is required to measure the mechanical properties of individual particles or constituents in situ. Conventional small-scale mechanical testing methods such as indentation can extract discontinuous data, but only at a resolution of at least several microns. In contrast, the recently developed PeakForce QNM® is a non-destructive method which measures the elastic response of a material surface with a resolution of a few nanometres. In this mode, an AFM probe is tapped over the surface (using a sinusoidal signal) and the peak force applied on the surface is used as a feedback parameter to track the scanned surface (i.e. the peak force is continuously monitored and kept constant during scanning) (Figure 2.2).

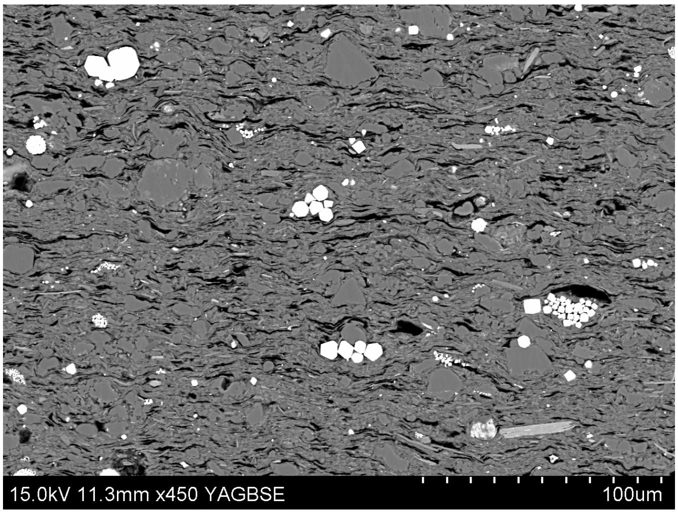

Figure 2.1: High quality BSE image of shale microstructure.

The mechanical response of the sample is extracted using the generated force-separation curve (one for every approach-withdraw cycle). The reduced Young's modulus can be calculated by fitting the Derjaguin-Muller-Toporov (DMT) model for contact mechanics on the curve obtained through the retracting stage of the tip movement (see Figure 2.3). According to this model, the relationship between peak force (F_{PF}), adhesion force (F_{Adh}) and the reduced Young's modulus (E^*) is as follows:

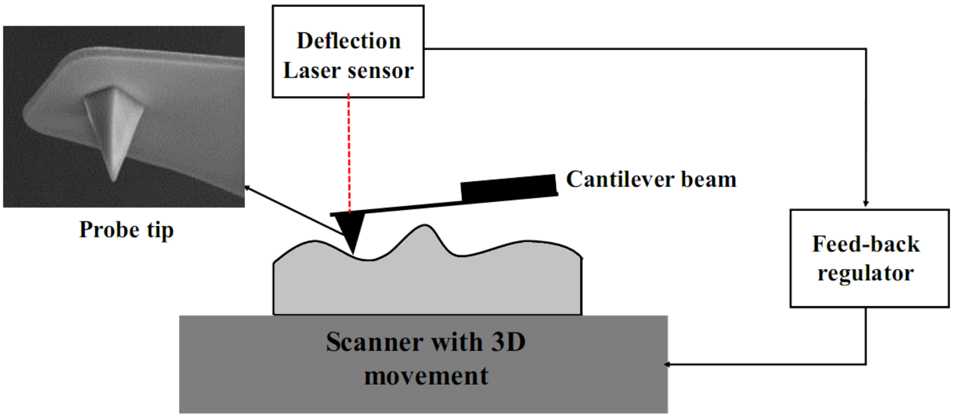

Figure 2.2: Schematic diagram of PeakForce QNM® system.

$$F_{PF} - F_{Adh} = \frac{4}{3}E^*\sqrt{R(d-d_0)^2} \tag{2.1}$$

where R is the tip radius, d_0 is surface rest position and (d-d_0) is the sample deformation. The modulus obtained from Eq. (2.1) can be related to the sample's elastic response as:

$$E^* = \left(\frac{1-\nu_s^2}{E_s} + \frac{1-\nu_{tip}^2}{E_{tip}}\right)^{-1} \tag{2.2}$$

where E is the Young's modulus, ν is the Poisson's ratio and subscripts s and tip represent the sample and tip, respectively.

In order to achieve reliable quantitative data, several calibration procedures should be performed. First, the effective tip radius is determined by probing a tip evaluation sample made of polycrystalline titanium standard coating (Figure 2.4). This standard sample has very small sharp roughness. The edges are much sharper than the tip. Therefore, they do not allow the tip to map the surface and instead the tip maps itself. Second, the cantilever spring constant which is the stiffness of the beam against bending, needs to be known. This value is often provided by the manufacturer. However, it can also be measured by pressing the tip against a very stiff sapphire sample. Third, the deflection of the cantilever beam is measured using a laser beam in term of voltage. This deflection contains information about the applied force (F_{PF}) and also the deformation of the sample underneath the tip (d-d_0). In order to calibrate the system and separate these factors, the tip is pushed against a sapphire sample, which serves as a surface with approximately infinite stiffness. Now, the so-called deflection sensitivity, S (m/Voltage), can be calibrated as all the deformation can be considered to occur in the cantilever.

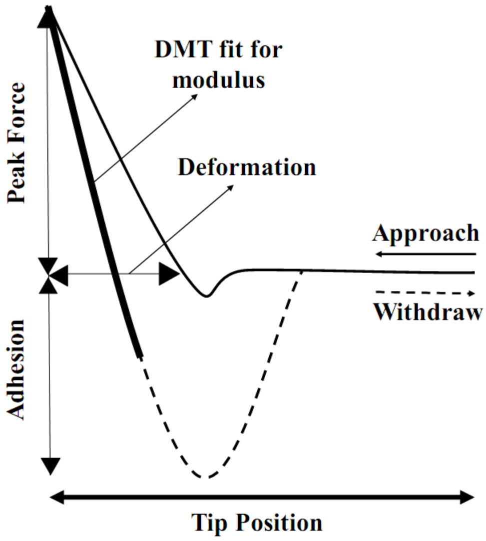

Figure 2.3: Schematic diagram of a generated force-separation curve for a single tapping of the PeakForce QNM® (Modified from Pittenger *et al.*, (2010)).

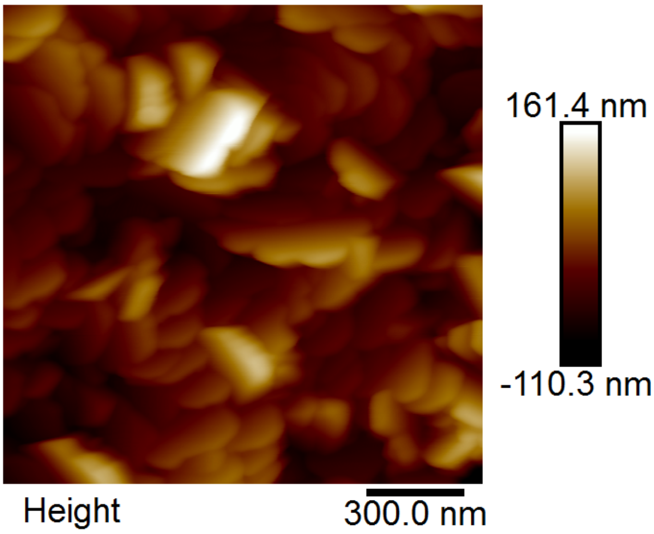

Figure 2.4: The surface map of polycrystalline titanium standard coating sample being normally used for tip radius measurement.

Once the deflection sensitivity is calibrated, the applied peak force and the sample deformation can be calculated as:

$$F = k \times S \times D \tag{2.3}$$

$$d = z - S \times D \tag{2.4}$$

where D is the deflection of the beam, z is the vertical scanner move and k is the spring constant for the cantilever (Figure 2.5).

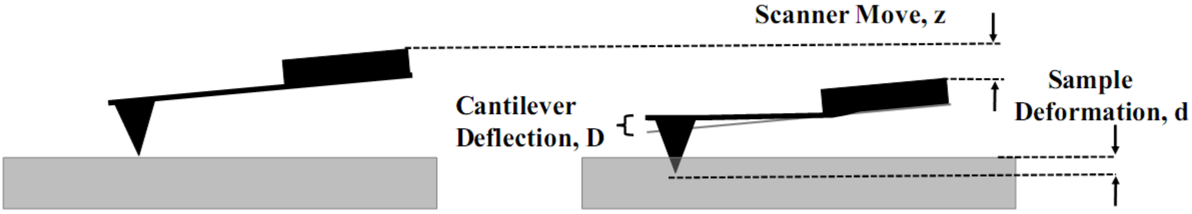

Figure 2.5: Schematic diagram of deformations in both cantilever and sample.

The final stage of the calibration is to evaluate the quantitative results of the PeakForce QNM® against a sample with known mechanical properties. A standard highly ordered pyrolytic graphite sample (HOPG-12M, Bruker) with Young's modulus of 18 GPa can be considered for this purpose.

2.3 Sample preparation

The sample preparation is an essential step to conduct successful PeakForce QNM® or indentation tests. The contact area of the indenter with the sample is a key parameter to estimate the mechanical properties accurately which is calculated based on the geometry of the tip and also the penetration depth. As soon as the tip touches the surface, the displacement sensors are activated and the penetration depth is measured. The estimation of contact area is based on two main assumptions: the tip axis is vertical and the sample surface is perfectly flat and horizontal. Any deviation from these assumptions can lead to inaccurate estimation of the contact area and consequently the measured properties (Saber-Samandari and Gross, 2009). When the tip touches a steep surface, more displacement is required to generate the same contact area as a flat horizontal surface. Although the contact area is the same, due to higher recorded deformation, a fictitious low modulus will be calculated.

It is less tedious to prepare a well-polished surface when the sample is made of one material, such as the pyrolytic graphite sample, which is used for the calibration. However, shale samples contain very hard grains embedded in much softer clay-kerogen matrix. The conventional mechanical polishing pulls out some of those grains and makes it difficult to prepare a smooth surface. In addition, through mechanical polishing, softer constituents such as clay and kerogen can be pushed over silt grains and roughly cover them as dirt. This reduces the quality of high resolution imaging or mechanical measurement. In this study, two steps of polishing were considered for sample preparation. In the first step, hand polishing using a diamond impregnated cloth was carried out. Shale cuttings were mounted on glass on both directions parallel and perpendicular to bedding and hand polished to reach the desired thickness. In the second step, in order to avoid artifacts such as grain plucking, samples were polished using argon broad ion beam (BIB) in the GATAN 691 Precision Ion Polishing System (PIPS^{TM}) (Amirmajdi *et al.*, 2009). To do so, discs with 2.5 mm in diameter were cut out of the hand polished sections with GATAN 601 Ultrasound Disc Cutter using water emulsion of boron nitrate powder as a saw. These discs were inserted into the PIPS^{TM} chamber and bombarded with Ar ions in a vacuum (10^{-2} Pa) for 6 hours (angle 3^o, 5 kV, 1-20 μA). It should be noted that it is more comfortable to work with these small discs due to very small space in the chambers of AFM, indentation and Ar ion milling apparatuses. Figure 2.6 shows a well-polished disc prepared based on the above mentioned steps.

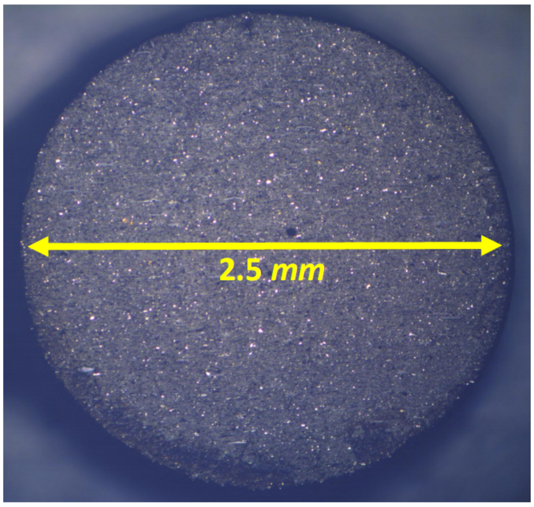

Figure 2.6: A polished disc-shaped shale sample.

2.4 Results and discussion

A high-resolution mechanical measurement such as PeakForce QNM® technique can unlock some of the mysteries about the macroscopic mechanical behaviour of shales. Here, the focus is on anisotropy of shale rocks by mapping the Young's modulus at different directions at the scale of few nanometers, to better understand the major source of anisotropy at macro scale. Additionally, the mechanical properties of organic matter and its roll in the microstructure of shale composite have been a serious challenge for rock physics modelling. This AFM mode provides us with the possibility of high resolution in-situ measurements which could help to expand the current available data based on small-scale mechanical response of shale rocks.

Organic-rich shale samples with different thermal maturity level were selected for this study. Additionally, both BSE and EDS analyses were carried out on the target areas for the nanoscale mechanical mapping to further facilitate the post-processing analyses of the data.

2.4.1 Nanoscale anisotropy of shale

The objective of this section is to estimate the elastic response of different constituents in shale composite at nanoscale. These components cover different range of moduli from softer component such as organic matter (<25 GPa), to stiffer grains such as pyrite (265 GPa) (Abou-Chakra Guery *et al.*, 2010; Bass, 1995; Whitaker *et al.*, 2010; Eliyahu *et al.*, 2015). It is of great importance to select a suitable tip with appropriate spring constant to capture the required range of moduli. A diamond tip with a relatively high spring constant of 272 Nm^{-1} (DNISP; Bruker) was selected for this study. To the best of our knowledge, this tip assembly has the range of measurement up to 80 GPa, which is the highest range available in the market (Bruker's Application Note 128). The tip radius was also measured around 40 nm using polycrystalline titanium standard coating sample.

The standard HOPG-12M was used as the last step of calibration of the tip to determine the best set of parameters which are required to be selected for this nanomechanical test such as tip oscillated frequency and the applied peak force. After several trials and errors, the values of 1 kHz and 50-150 nN were considered for the oscillation frequency of the tip and the peak force, respectively. These settings generated 1-2 nm indentation depths on the sample.

Figure 2.7 shows the reduced modulus map over HOPG-12M sample, the histogram and the normal probability distribution function (PDF) of the measured data. The mean value of 20.58 GPa was determined for this data set. Considering a Poisson's ratio of 0.3 for HOPG-12M, the Young's modulus can be obtained as 18.7 GPa, which is quite close to the nominal value of 18 GPa reported by the manufacturer. The above mentioned details will be used in the rest of this study for diamond tip. In addition, it should be noted that due to very high elastic stiffness of diamond (E>1000 GPa) (Mavko *et al.*, 2009), the deformation of the diamond tip will be ignored in the calculation of Young's modulus of samples (see Eq. 2.2).

In addition to the mechanical map, topography of the surface was also measured through this test. This data is very critical to identify the fictitious values resulted from topographical features. For instance, the pattern of roughness on the HOPG-12M sample can be clearly identified on the map of elastic modulus (Figure 2.7). In order to better correlate the measured mechanical properties to different phases, more analyses including BSE and EDS need to be conducted on

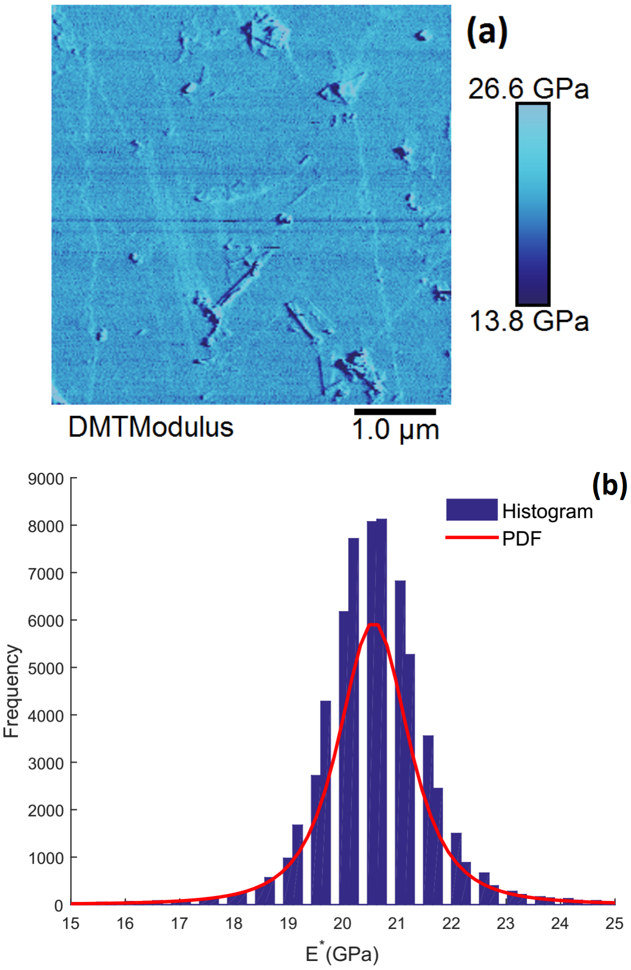

Figure 2.7: Reduced modulus map (a) and its histogram (b) on the HOPG-12M standard sample.

the selected area to generate map of elemental and phase distribution. Samples were viewed in BSE mode with the following settings: 4.1 mm WD, 1.5-3.0 kV accelerating voltage, 2-4 nA beam current, using through-the-lens detector for better spatial resolution. The Microanalysis settings for the EDS collection were set at 300 μm dwell time, 15 kV accelerating voltage and 4 nA filament current.

Figure 2.8c shows the elastic modulus map obtained on a 25×25 μm^2 area on the shale sample perpendicular to bedding direction. Two types of grains with different and relatively high stiffness (>50 GPa), and also areas with very low stiffness (<30 GPa) can be clearly recognised in this image. As part of the data analysis, it was initially assumed that the stiffer grains represent pyrite (and were later identified as such from the EDS analysis (2.8b). An average value above 100 GPa was measured on pyrite grains which is lower than the reported values of 265 GPa in the literature (Whitaker *et al.*, 2010). The main reason for this deviation is that the reliable range of measurable elastic modulus for the diamond tip is less than 80 GPa (Pittenger *et al.*, 2010). The mean value of the measured reduced modulus over the grains corresponding to quartz in the EDS analysis (2.8b) is around 75 GPa, lower than the value reported in Heyliger *et al.* (2003) but between the values reported by Elihayu *et al.* (2015), 63 ± 8 GPa, and Mavko *et al.* (2009), 77-95 GPa. Again, it is difficult to rely on the quantity of this result because of the reliable range of the tip. However, the quality of these data will be later investigated to better understand the in-situ mechanical response of stiff grains in shale composite.

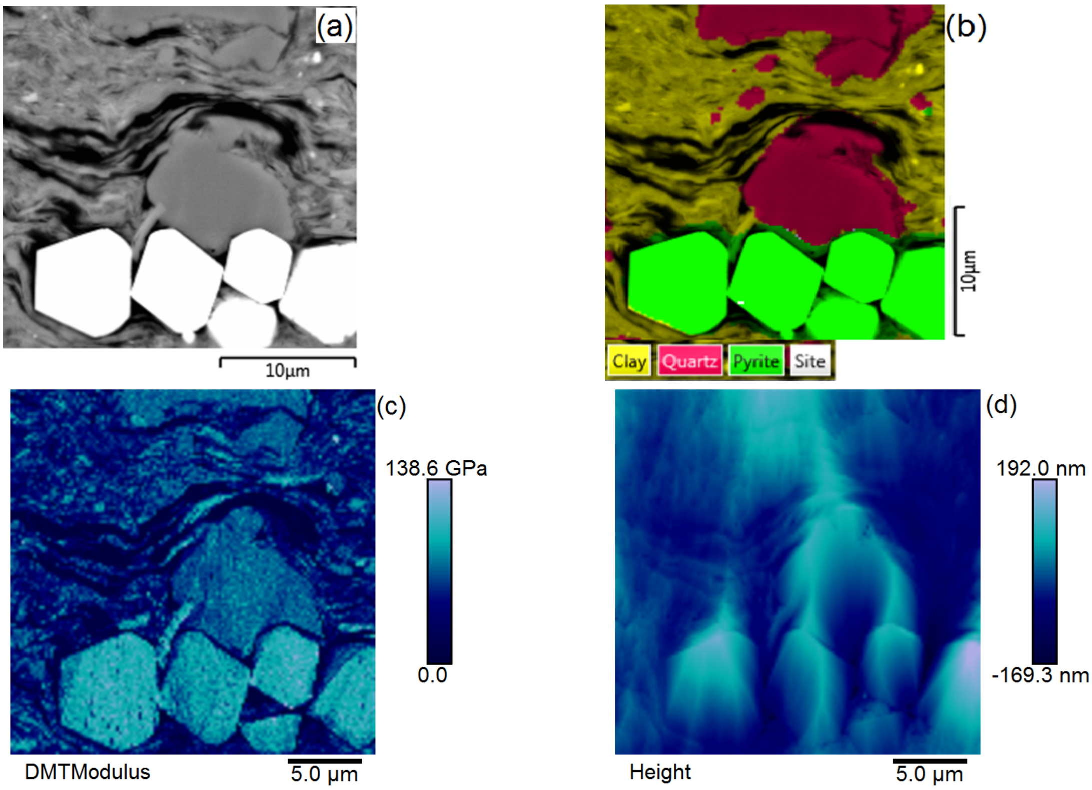

Figure 2.8: Different analyses on a target area perpendicular to the bedding direction. (a): SEM image using back scattered electron imaging, (b): Chemical analysis using energy dispersive spectrometry, (c): Reduced modulus map using PeakForce QNM®, and (d): Topography map taken during mechanical mapping.

As discussed before, it is difficult to prepare very perfect smooth surface on shale samples and the roughness may yield unreliable data. Comparing the mechanical and the topographical maps (Figure 2.8c and 2.8d), it can be concluded that some soft areas, defined by Young's moduli less than 25 GPa, are correlated with abrupt trench on the sample. In fact, unlike the interpretation made by Eliyahu *et al.* (2015), not all the soft regions can be attributed to organic matter and a careful comparison between both the mechanical and topographical images is required to locate real soft phases in the mechanical image. Such comparison revealed the fact that the presence of the organic matter phase in the shale composite is not similar to other inclusions such a quartz and pyrite. This phase is deeply mixed within the clay matrix rather than existing as isolated grains with different values less than 10 GPa for its stiffness. This is an important consideration in rock physics models to account for the role of organic matter in the overall mechanical response of shales. The mechanical response of organic matter will be profoundly studied in the next section.

As the macroscopic response of shales is highly anisotropic, it is of interest to look at anisotropy at the nanoscale. Figure 2.9 shows the reduced modulus map of sections both parallel (E_1^*) and perpendicular (E_3^*) to bedding direction. Two target areas were selected on both images that contained clay matrix and quartz grains. The measured data in these areas were extracted and subjected to statistical analysis. Figure 2.10 illustrates the histogram and normal curve on the data and the mean values and standard deviations (SD) are provided in Table 2.1.

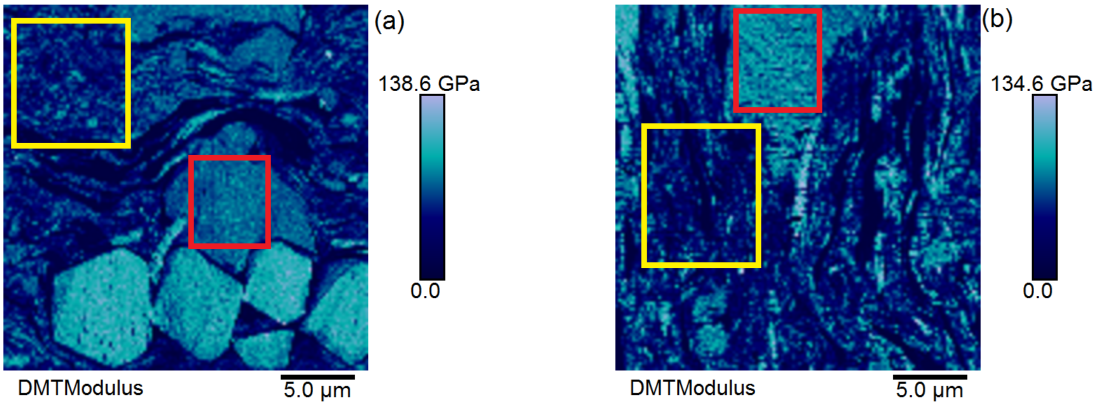

Figure 2.9: Yellow boxes are the target areas for clay matrix and red boxes are the target areas for quartz on sections perpendicular (a) and parallel (b) to bedding direction.

The mean values obtained on quartz grains are almost identical, producing an anisotropy ratio (E_1^*/E_3^*) around 0.95. The presented measurements were taken from two different grains with unknown orientations. However, this result was confirmed using several measurements on different randomly selected grains. The isotropic elastic response of stiff grains observed in-situ in shale microstructure is not exactly matched with the measurements on big crystal which showed anisotropy in different mechanical properties (Heyliger *et al.*, 2003; Timms *et al.*, 2010). For instance, an anisotropy ratio of 1.3 was reported on Young's modulus of monocrystal α-quartz (McSkimin *et al.*, 1965; de Boer *et al.*, 1966; Heyliger *et al.*, 2003; Calderon *et al.*, 2007). This could be very important in rock physics modelling, where some assumptions have to be made about the mechanical behaviour of each individual component of rocks.

The clay matrix, on the other hand, shows significant anisotropy in these two sections, with a ratio around 1.45. This high anisotropy is almost in the range of the reported anisotropy

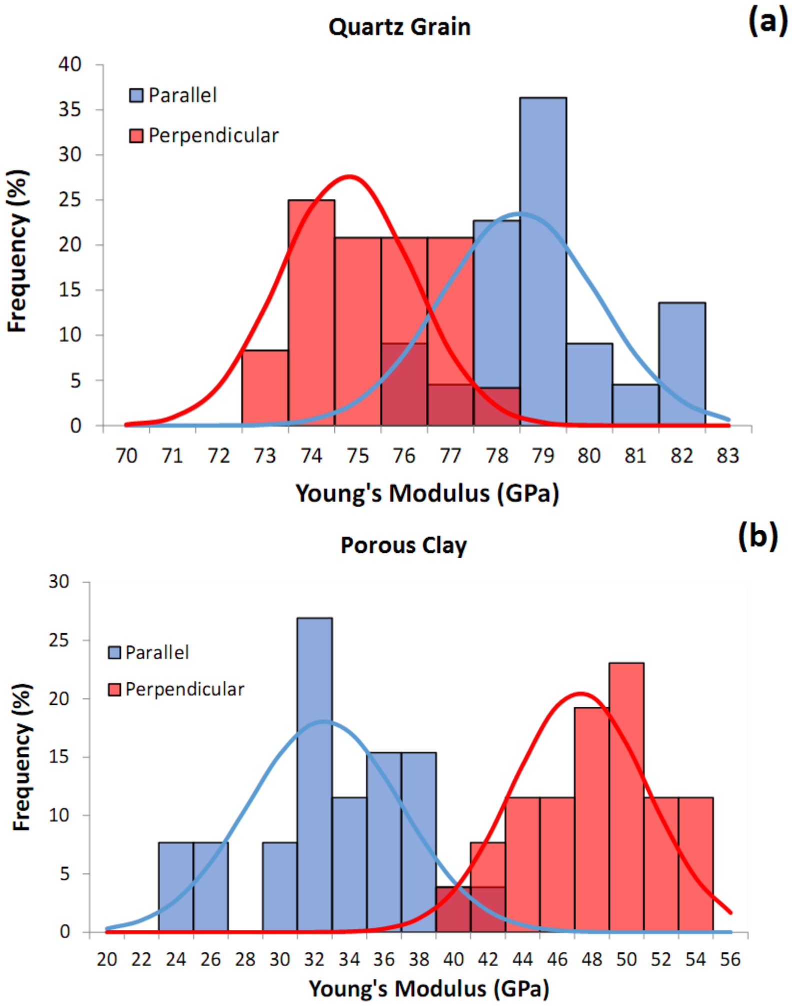

Figure 2.10: Histogram and normal curve of the measured reduced moduli on quartz grain (a) and clay matrix (b) in both sections parallel and perpendicular to bedding direction.

on core-scale shale samples (Ulm and Abousleiman, 2006). This comparison provides more support for the theory proposed by Ortega *et al.* (2007), about the origin of shale anisotropy in which the solid unit of clay was assumed to be the main source of anisotropy. Additionally, the values obtained on the clay matrix are higher than the properties assumed for a solid unit of clay in several studies (Hornby *et al.*, 1994; Ortega *et al.*, 2007; Mavko, 2009), but they are within the range of the properties reported for clay particles (Wang *et al.*, 2001). Eliyahu *et al.* (2015) reported 29±1 GP on the clay matrix, while they did not consider the direction of the section in their study. Considering Poisson's ratio of 0.3, this value is almost identical with the measured data on the section parallel to bedding, which is 29.6 GPa (see Table 2.1). Further study is required to understand what type of microcomponent of shale matrix, a clay sheet, agglomerate of clay particles or porous clay, was being touched by the tip.

Table 2.1: Results of statistical analysis on the data related to clay matrix and quartz grains.

Parameters	Reduced modulus on sections				Anisotropy ratio ($\frac{E_1^*}{E_3^*}$)
Direction	Parallel to bedding (E_3^*)		Perpendicular to bedding (E_1^*)		
Data	Mean (GPa)	SD	Mean (GPa)	SD	
Quartz grains	78.5	1.7	74.75	1.43	0.95
Porous clay	32.5	4.41	47.3	3.88	1.45

2.4.2 Elastic response of organic matter

The volume fraction of organic matter in shales with the potential of hydrocarbon source rock can vary significantly from less than 1 % to more than 40 % (Vernik and Nur 1992). Due to the relative softness of this phase, the mechanical behaviour of shale is greatly influenced by even a small amount of this constituent (Vernik and Milovac, 2011; Sayers, 2013; Kumar *et al.*, 2015). However, a wide range of measured elastic properties was reported for organic matter which could consequently lead to difficulties in implementation of rock physics models. For instance, Zeszotarski *et al.* (2004) performed nanoindentation tests on kerogen in Woodford shale. An isotropic behaviour was observed and if Poisson's ratio is assumed to be 0.3, then the Young's modulus is estimated to be 11.5 GPa. The same approach was adopted by Kumar (2012) and Zargari *et al.* (2013), who generated values of less than 2 GPa for highly porous kerogen. Vernik and Nur (1992) used the thin-layer composite concept and back-analysed the mechanical properties of kerogen, concluding that kerogen is isotropic with values of 8 GPa and 0.28 for the Young's modulus and the Poisson's ratio, respectively. Yan and Han (2013) used effective medium theory and back-calculated the Young's modulus of 4.5, 6.42, 10.7 GPa for immature, mature and over-mature organic matter, respectively. Eliyahu *et al.* (2015) performed the PeakForce QNM® tests with an atomic force microscope to make nanoscale measurements of the Young's modulus of organic matter in a shale thin section. Results ranged from 0-25 GPa with a modal value of 15 GPa. Emmanuel *et al.* (2016a, 2016b) studied the effect of thermal maturity and temperature on kergen's mechanical behaviour and found out that increase in thermal maturity increases the kerogen's elastic modulus; however, an increase in temperature reduces this parameter.

In this section, the main focus of the mechanical measurement is on organic matter. This component, which can be identified as dark areas in SEM images (see Figure 2.1), normally does not appear as large grains similar to silt inclusions, but it is found mixed within the matrix in the form of narrow strips. Therefore, it is more difficult to manually extract and interpret the data measured on this phase. In order to address this problem, statistical analysis will be performed on the experimental data obtained on the whole section in order to estimate the properties of organic matter. In addition, the fictitious low values of the observed elastic modulus, produced as a result of existing holes and cracks on the surface, will be carefully investigated in order to avoid any influence on the estimated properties of organic matter.

An organic-rich shale with 11.8 weight % of total immature organic matter (R_o=0.53%) was considered. A section was prepared perpendicular to bedding, to have a higher chance to encounter all the phases particularly organic matter, during the measurement. For each target area, all the measured data were extracted and and plotted as frequency histogram. A probability distribution function is required to be fitted over the histogram in order to analyse the data. As there are phases with different stiffness in shale's microstructue, the histogram has more than one peak and a simple normal distribution cannot represent the data set. In order to tackle with this bimodal histogram, the commercial software MATLAB was adopted to generate a Kernel probability distribution function over the histogram. It should be noted that the PDF is used to capture the moduli related to the peaks of frequency systematically rather than the exact values of frequency. Figure 2.11 shows the reduced Modulus (E^*) map for two target areas along with their histograms. It can be observed that both sections show a clear peak at low values of elastic modulus, which can be attributed to kerogen embedded in the shale's microstructure. Interestingly, the first peaks in both sections are at the value of 6.45 GPa, which confirms the consistency in the measurements. This value corresponds to a Young's modulus of 5.9 GPa if the Poisson's ratio is assumed to be 0.3.

In order to increase the level of confidence that the target areas in Figure 2.11 contain kerogen and the measured low values of elastic response are related to this phase, EDS analysis can be performed to detect any carbon anomaly on the sections. A wide area around the section illustrated in Figure 2.11b, was analysed for carbon content. Figure 2.12 shows both SEM image and carbon analysis. Large areas of carbon concentration were detected by EDS analysis which match perfectly with both the dark area on SEM image and low value of elastic modulus on the mechanical map (see Figure 2.11b).

Another problem which might be considered to be influential on the produced histogram is the sharp concavities on the sample surface, that can produce fictitious low values of elastic modulus. It is of interest to make sure these unrealistic data does not contribute to the first peak

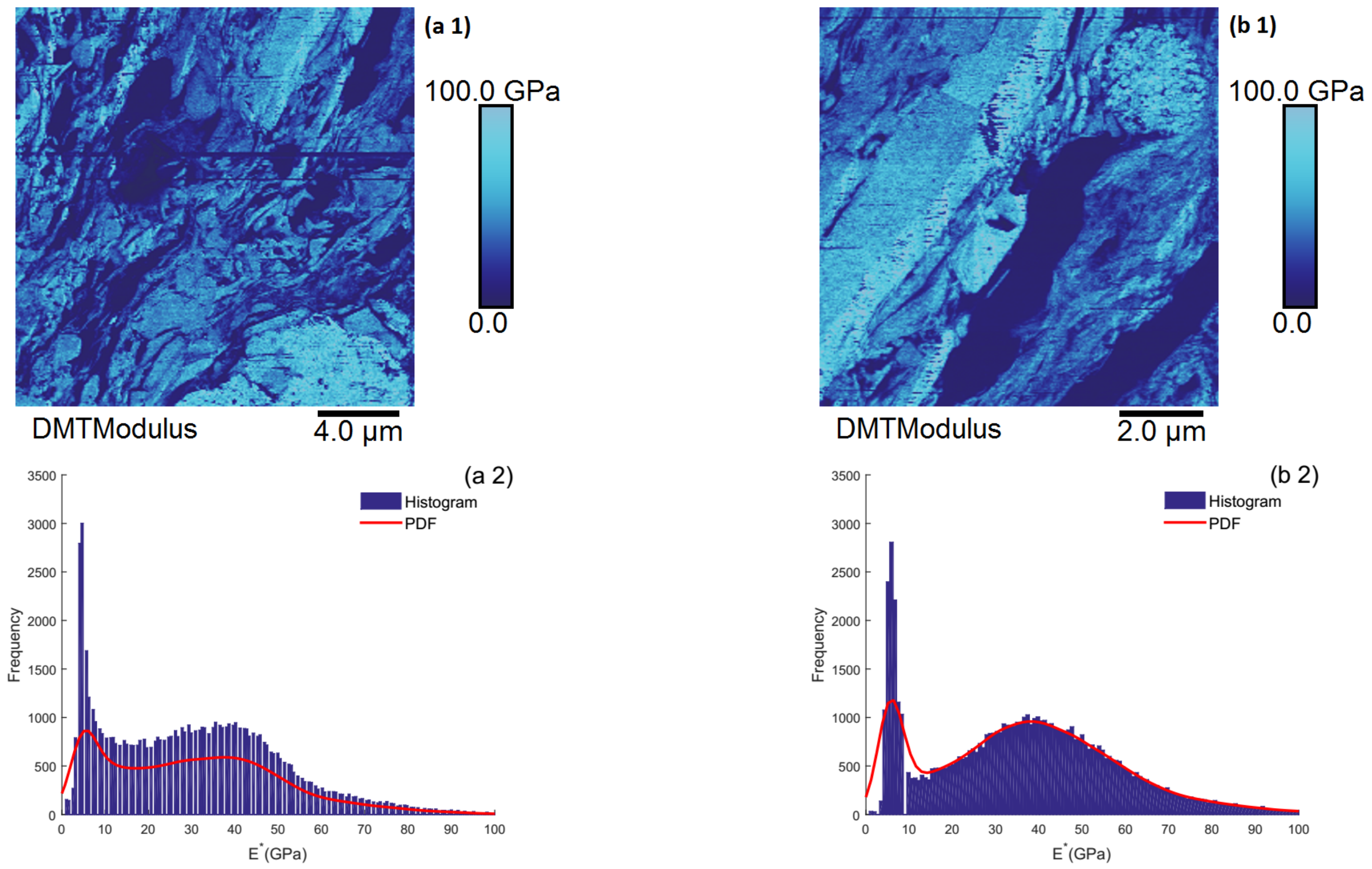

(a)

(b)

Figure 2.11: Reduced modulus maps (a 1 and b 1) and their histogram (a 2 and b 2) on an immature shale sample.

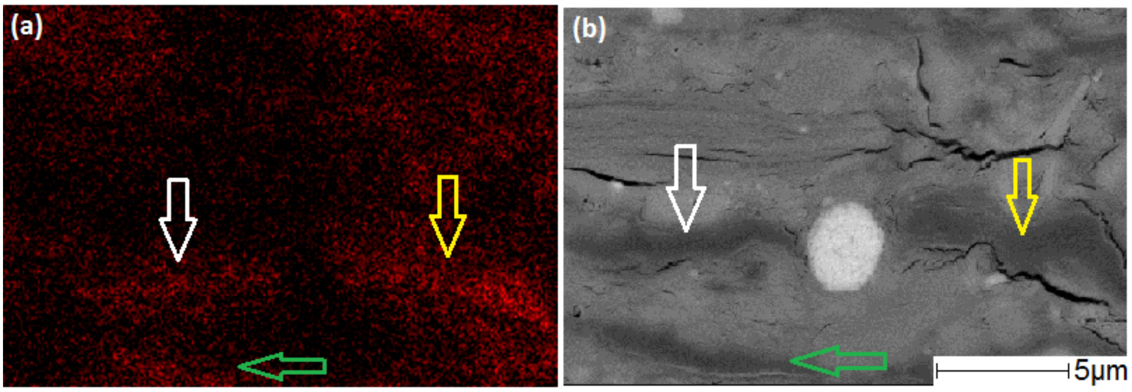

Figure 2.12: EDS carbon analysis (a) and SEM (b), for the area around the section presented at 2.11b (Each set of arrows shows the associated carbon anomaly between the two images).

being observed in the histograms. Figure 2.13 shows the topographical image of the section presented in Figure 2.11a. A cavity with sharp slope is clearly recognised on this section, which could have been formed as a result of silt inclusions being pulled out through the publishing procedure. Two cross sections over this hole were considered and the measured elastic moduli were extracted (Figure 2.14). As it can be observed, the measured property over the cavity is less then 2 GPa which is much lower than the value of 6.45 GPa for the first peak in Figure 2.11a. Such comparison provides more ground for the fact that the first peaks in the presented histograms are related to organic matter in the shale microstructure.

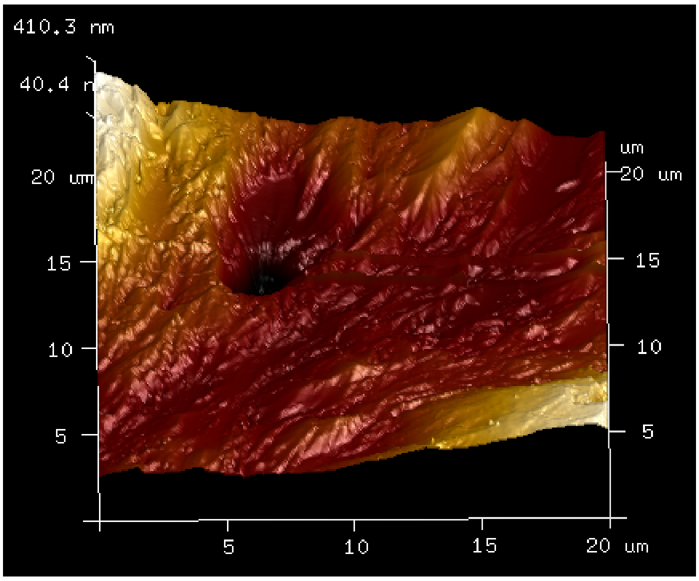

Figure 2.13: Three dimensional topographical image of the sample surface presented at Figure 2.11a.

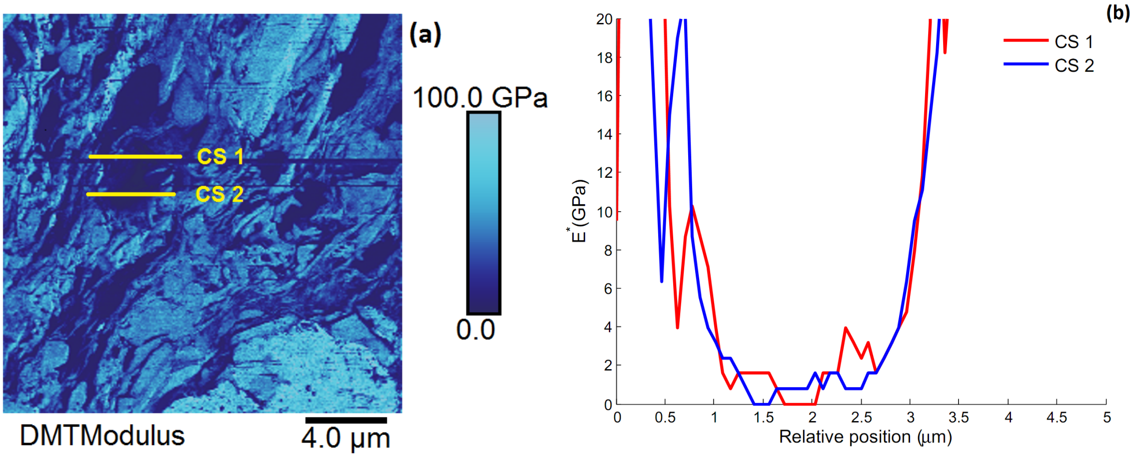

Figure 2.14: Measured reduced elastic moduli (a) and the values on two cross sections (b) over the area with severe concavity (Only values up to 20 GPa were shown for cross sections).

In order to observe the effect of thermal maturity level on the mechanical response of organic matter, a shale with 5.95 weight % of total organic carbon and mature kerogen (R_o=0.89%) was also considered for nanomechanical mapping. Figure 2.15 shows a mapping section on this samples along with the histogram of reduced elastic modulus. Again, a peak for a relatively soft phase (around 9 GPa) can be seen, which could relate to kerogen. However, the peak is not as clear as the one for immature sample (see Figure 2.11). The reason could be because of small patch of kerogen in the shale matrix, which makes the measurement less accurate. This issue was also noticed by Zargari *et al.* (2013), when they tried to locate kerogen patch for nanoindentation test in mature samples.

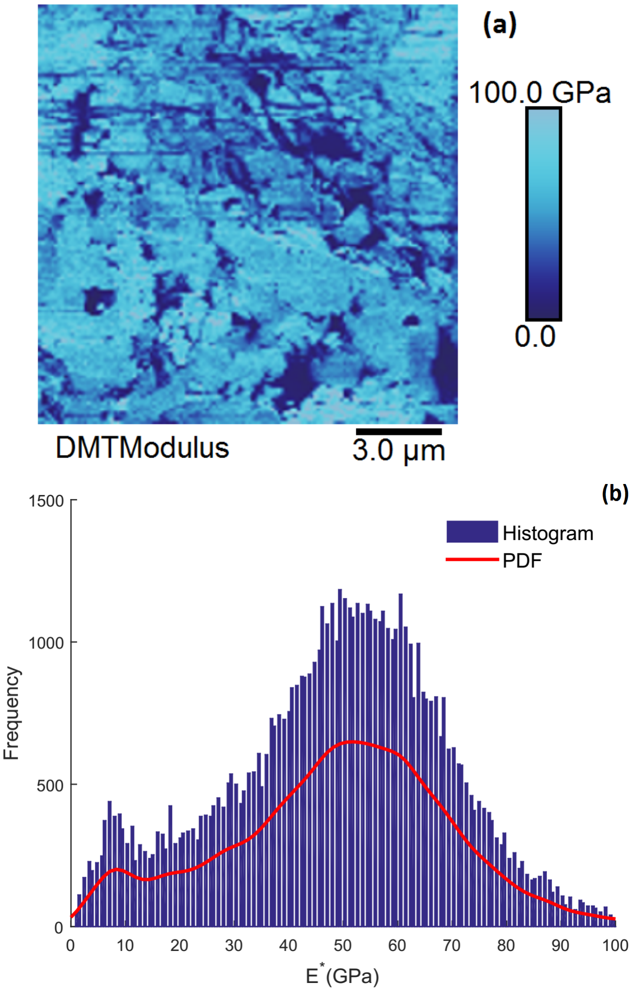

Figure 2.15: Reduced modulus map (a) and its histogram (b), on a mature shale sample.

Unlike nanoindentation tests in which the resolution of measurement is around several microns, the PeakForce QNM® measurements can be focused on much smaller area with a sharp tip which can generate a resolution as small as 10 nm. Therefore, stiff silicon nitride tip (Tap525; 119 Bruker) was selected which has the accurate range of 1-30 GPa. Considering Young's modulus of less than 15 GPa, frequently being reported for kerogen (Zeszotarski *et al.*, 2004; Ahmadov *et al.*, 2009; Zargari *et al.*, 2013), this tip has a quite suitable range for measurement on this phase. The spring constant for this cantilever was measured around 80 Nm^{-1} which is lower than the value of 272 Nm^{-1}, being measured for the diamond tip. The nominal value of tip radius was reported by the manufacturer as 8 nm; however, the measurement performed by probing the tip evaluation sample made of polycrystalline titanium standard coating showed a value of 13.5 nm. In comparison to diamond tip with a tip radius of 40 nm, the silicon nitride tip increases the resolution of imaging and consequently reduces the error caused by inclination of the surface. An area with a dimension less than 5 μm was scanned using a silicon nitride tip. Figure 2.16 shows the results for this new test in which a very clear peak can be identified for the organic matter phase. The reduced elastic modulus corresponding to the peak value is around 11 GPa. However, unlike the diamond tip which could be assumed to be rigid, the silicon nitride tip is much softer and its deformation should be taken into account (see Eq. 2.2). Considering the values of 310 Nm^{-1} and 0.27 for E_{tip} and v_{tip} (Bruker's Application Note 128), respectively, the reduced modulus, $\mathrm{E}_s/(1-\mathrm{v}_s^2)$, for kerogen in this sample can be calculated as 11.37 GPa. Therefore, assuming the Poisson's ratio of 0.3 for mature kerogen, the Young's modulus will be 10.35 GPa.

Previous studies on the elastic response of organic matter have been mainly based on nanoindentation tests along with reverse analysis using rock physics modelling (Vernik and Nur, 1992; Ahmadov *et al.*, 2009; Zargari *et al.*, 2013). One problem associated with nanoindentation measurement is that patches of kerogen in the shale microstructure have a limited size, normally less than 20 μm (see Figure 2.1), which does not satisfy the assumption of infinite half space required for the calculation of the indention modulus. In addition, formulating a rock physics model requires several assumptions concerning shale microstructure and the mechanical properties of the constituents. Any possible error originated from these assumptions will be accumulated in the back-calculated mechanical properties of kerogen. As nanoscale mechanical mapping does not suffer from these mentioned problems, it is of interest to compare its results with previous studies. Table 2.2 provides a summary of the kerogen elastic properties obtained in this study along with the reported values in literature. It can be concluded that the PeakForce QNM® measurements on kerogen is quite consistent with the previous studies; however, there are still differences in kerogen properties obtained through different techniques and it is not an easy task to prove which measurement method provides the most accurate values.

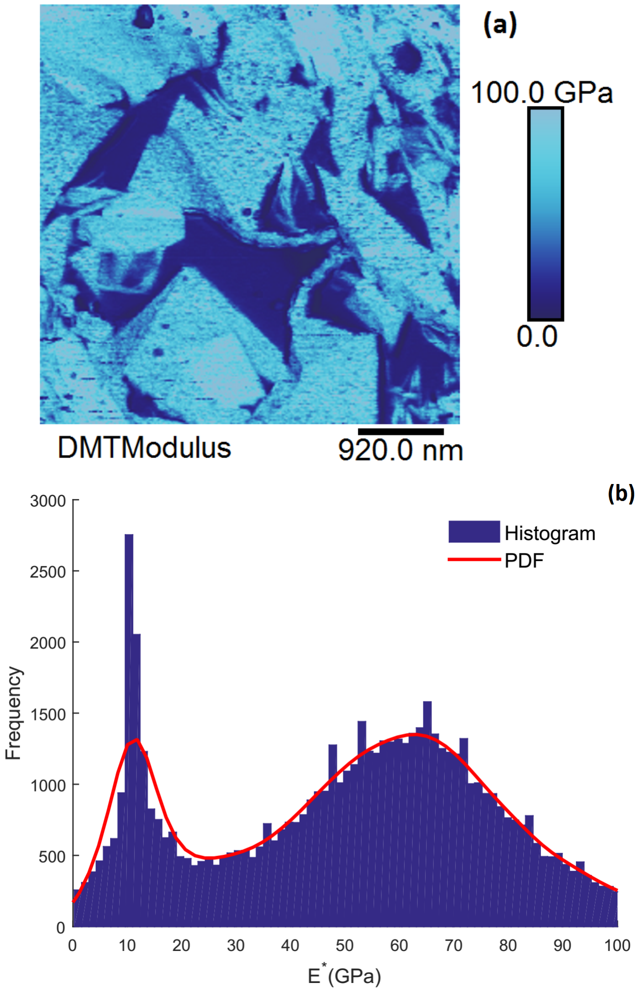

Figure 2.16: Reduced modulus map (a) and its histogram (b) on a mature shale sample.

2.5 Summary and Conclusions

In this study, the recently developed PeakForce QNM® technique, which allows for mechanical measurements with resolutions of less then several nanometres, was adopted to study the elastic response of shale rocks at sub-silt size scale. Two different probes known as diamond and stiff silicon nitride tips were used in this study. The diamond tip is the stiffest tip on the market which provides the possibility of measurements on silt inclusions. However, the stiff silicon nitride probe has a more suitable range of measurement (<30 GPa) for organic matter and also a much sharper tip, which consequently increases the resolution of data acquisition. The system was calibrated in several steps to ensure the accuracy of measurements including a final stage of calibration over a standard sample with known mechanical properties. Shale thin sections were prepared in both parallel and perpendicular to bedding direction. Two stages of polishing including hand polishing using a diamond impregnated cloth and argon broad ion beam milling were applied to smoothen thin sections as much as possible.

Table 2.2: Summary of kerogen elastic modulus obtained through different methods.

Reference	Formation	Method	R_o (%)	Thermal Maturity	E (GPa)	ν
This study	Posidonia Shale	PeakFroce QNM®	0.53 0.89	Immature Mature	5.9 10.35	0.3 0.3
Vernik and Nur (1992)	Bakken	Rock physics	—	—	8	0.28
Yan and Han (2013)	Green River shale	Rock physics	— —	Immature Mature	4.5 6.4	0.28 0.28
Lucier *et al.* (2011)	Haynesville	Rock physics	2.5	Overmature	10.7	0.28
Zeszotarski *et al.* (2004)	Woodford	Indentation	—	Immature	9.7	0.3
Ahmadov (2011)	Bazhenov Lockatong	Indentation	— —	— —	5.4 10.8	0.3 0.3
Kumar (2012)	Woodford Woodford Kimmeridge	Indentation	0.51 6.36 0.53	Immature Overmature Immature	7.9 13.9 4.9	0.3 0.3 0.3

In the first step, the nanomechanical mapping was compared with SEM and EDS images in order to confidently correlate the mechanical measurements to different constituents. The capability of diamond tip to capture the differences in the mechanical properties of shale's constituents was clearly confirmed. The properties being measured on two areas on quartz grains and porous clay in both sections were extracted manually and compared. High level of anisotropy, comparable to core scale anisotropy, was observed over the porous clay. Unlike many studies on large scale quartz minerals which showed noticeable anisotropy in its elastic properties, the nanoscale mechanical mapping showed an almost isotropic elastic modulus. The absolute measured values over stiff grains such as pyrite and quartz are still less then the reported values in the literature. This could be justified by the maximum limit of 80 GPa for the range of applicability of the diamond tip.

In the second step, the measurements were focused on the kerogen phase which is deeply mixed within the clay matrix. Two shale samples with different thermal maturity levels were considered. As the kerogen exists in shale matrix as small pieces or narrow strips, the measured data cannot be manually extracted in a correct way. Statistical analysis was adopted to analyse all the acquired data using MATLAB. A clear peak at the value of 6.4 GPa was observed in the histogram of the reduced elastic modulus for the immature shale sample. As the kerogen content in the mature sample appears in much smaller pieces, sharper tip of stiff silicon nitride was used to map this phase. The first peak in the histogram of the reduced elastic modulus corresponded to 11.37 GPa. It can be concluded that the elastic stiffness of kerogen increases with the thermal maturity level. In addition, the measurements in this study were consistent with the previously reported values for elastic modulus of kerogen obtained through nanoindentation test and rock physics modelling.

To conclude, the PeakForce QNM® technique was shown to be a useful tool in order to generate both quantitative and qualitative information regarding the elastic response of shale's constituents. It was observed that the elastic moduli of organic matters, which play a critical role in macroscopic shale behaviour, can be evaluated with this technique. However, because organic matters cover different range of chemical substances, it is important to conduct the nanomechanical measurement on different shale samples' in order to produce a complete data set for the elastic properties of organic matters. Such data is essential to develop rock physics (homogenisation) models for predicting the mechanical response of shales. This point will be deeply studied and discussed in Chapter 4.

References

Abou-Chakra Guery A., Cormery F., Shao F., Kondo D. 2010. A comparative micromechanical analysis of the effective properties of a geomaterial: effect of mineralogical compositions. *Computers and Geotechniques*, **37**, 585-593.

Ahmadov R., Vanorio T., Mavko G. 2009. Confocal laser scanning and atomic-force microscopy in estimation of elastic properties of the organic-rich Bazhenov Formation. *The Leading Edge*, **28**, 18-23.

Ahmadov, R. 2011. Microtextural Elastic and Transport Properties of Source Rocks. PhD Thesis, Stanford U., Stanford, California, USA.

Amirmajdi O.M., Ashyer-Soltani R., Clode M.P., Mannan S.H., Wang Y., Cabruja E., Pellegrini G. 2009. Cross-section preparation for solder joints and MEMS device using argon ion beam milling. *IEEE Transactions on electronics packaging manufacturing*, **32**(4), 265-271.

Bass J.D. 1995. Mineral Physics and Crystallography. In: A Handbook of Physical Constants, Ahrens T J (ed.), AGU Reference Shelf.

Bobko C., Ulm F.J. 2008. The nano-mechanical morphology of shale. *Mechanics of Material*, **40**, 318-337.

Bruker's Application Note 128. Quantitative mechanical property mapping at the nanoscale with PeakForce QNM. https://www.bruker.com/products/surface-analysis/atomic-force-microscopy/afm-application-notes.html

de Boer K., Jansen A.P.J., van Santen R.A., Watson G.W., Parker S.C. 1996. Free-energy calculations of thermodynamic, vibrational, elastic, and structural properties of α-quartz at variable pressures and temperatures. *Physical Review B*, **54**, 826.

Calderon E., Gauthier M., Decremps F., Hamel G., Syfosse G., Polian A. 2007. Complete determination of the elastic moduli of α-quartz under hydrostatic pressure up to 1 GPa: an ultrasonic study. *Journal of Physics: Condensed Matter*, **19**(43).

Eliyahu M., Emmanuel S., Day-Stirrat R.J., Macuulay C. 2015. Mechanical properties of organic matter in shales mapped at the nanometer scale. *Marine and Petroleum Geology*, **59**, 294-304.

Emmanuel S., Eliyahu M., Day-Stirrat R.J., Hofmann R., Macaulay C.I. 2016a. Impact of thermal maturation on nano-scale elastic properties of organic matter in shales. *Marine and Petroleum Geology*, **70**, 175-184.

Emmanuel S., Eliyahu M., Day-Stirrat R.J., Hofmann R., Macaulay C.I. 2016b. Softening of organic matter in shales at reservoir temperatures. *Petroleum Geoscience*.

Heyliger P., Ledbetter H., Sudook K. 2003. Elastic constants of natural quartz. *Acoustical Society of America*, **114**(2), 644-650.

Hornby B.E., Schwartz L., Hudson J. 1994. Anisotropic effective medium modeling of the elastic properties of shales. *Geophysics*, **59**, 1570-83.

Kumar V. 2012. Geomechanical Characterization of Shale Using Nano-indentation. MSc dissertation, University of Oklahoma.

Kumar V., Sondergeld C., Rai C.S. 2015. Effect of mineralogy and organic matter on mechanical properties of shale. *Interpretation*, **3**(3), SV9-SV15.

Lide D.R. 2004. Handbook of chemistry and physics. CRC Press.

Lucier A. M., Hofmann R., Bryndzia L.T. 2011. Evaluation of variable gas saturation on acoustic log data from the Haynesville Shale gas play, NW Louisiana, USA. *The Leading Edge*, **30**, 300-311.

Mavko G., Mukerji T., Dvorkin J. 2009. The Rock Physics Handbook. Cambridge University Press.

McSkimin H.J., Andreatch P., Thurston R. 1965. Elastic moduli of quartz versus hydrostatic pressure at 25^o and - 195.8^oC. *Journal of Applied Physics*, **36**, 1624.

Ortega J.A., Ulm F.J., Abousleiman Y.N. 2007. The effect of the nanogranular nature of shale on their poroelastic behavior. *Acta Geotechnica*, **2**, 155-182.

Pittenger B., Erina N., Su C. 2010. Quantitative Mechanical Property Mapping at the Nanoscale with PeakForce QNM, Bruker Corporation Application Note AN128.
http://nanoscaleworld.bruker-axs.com/nanoscaleworld/media/p/418.aspx

Rybacki E., Reinicke A., Meier T., Makasi M., Dresen G. 2015. What controls the mechanical properties of shale rocks? – Part I: Strength and Young's modulus. *Journal of Petroleum Science and Engineering*, **135**, 702-722.

Saber-Samandari S., Gross K.A. 2009. Effect of angled indentation on mechanical properties. *Journal of the European Ceramic Society*, **29**(12), 2461-2467.

Sayers C.M. 2013. The effect of kerogen on the elastic anisotropy of organic-rich shales. *Geophysics*, **78**(2), D65-D74.

Sone H., Zoback M.D. 2013a. Mechanical properties of shale-gas reservoir rocks - Part 1: Static and dynamic elastic properties and anisotropy. *Geophysics*, **78**(5), D381-D392.

Sone H., Zoback M.D. 2013b. Mechanical properties of shale-gas reservoir rocks - Part 2: Ductile creep, brittle strength, and their relation to the elastic modulus. *Geophysics*, **78**(5), D393-D402.

Timms N.E., Healy D., Reyes-Montes J.M., Collins D.S., Prior D.J., Young R.P. 2010.

Effects of crystallographic anisotropy on fracture development and acoustic emission in quartz. *Journal of Geophysical Research: Solid Earth*, **115**(B7).

Trtik P., Kaufmann J., Udo V. 2012. On the use of peak-force tapping atomic force microscopy for quantification of the local elastic modulus in hardened cement paste. *Cement and Concrete Research*, **42**, 215-221.

Ulm F.J., Abousleiman Y. 2006. The nanogranular nature of shale. *Acta Geotechnica*, **1**, 77-88.

Vernik L., Nur A. 1992. Ultrasonic velocity and anisotropy of hyrdocarbon source rocks. *Geophysics*, **57**(5), 727-735.

Vernik L., Milovac J. 2011. Rock physics of organic shales. *The Leading Edge*, **30**, 318-323.

Wang Z., Wang H., Cates M.E. 2001. Effective elastic properties of solid clays. *Geophysics*, **66**(2), 428-440.

Whitaker M.L., Liu W., Wang L. Li B. 2010. Acoustic Velocities and Elastic Properties of Pyrite (FeS2) to 9.6 GPa. *Journal of Earth Science*, **21**, 792-80.

Yan F., Han D., 2013. Measurement of elastic properties of kerogen. 83rd SEG Annual Meeting.

Young T.J., Monclus M.A., Burnett T.L., Broughton W.R., Ogin S.L., Smith P.A. 2011. The use of the PeakForceTM quantitative nanomechanical mapping AFM-based method for high-resolution Young's modulus measurement of polymers. *Measurment Science and Technology*, **22**.

Zargari S., Prasad M., Mba K.C., Mattson E.D. 2013. Organic maturity, elastic properties, and textural characteristics of self resourcing reservoirs. *Geophysics*, **78**(4), D223-D235.

Zeszotarski J.C., Chromik R.R., Vinci R.P., Messmer M.C., Michels R., Larsen J.W. 2004. Imaging and mechanical property measurements of kerogen via nanoindentation. *Geochimica et Cosmochimica Acta*, **68**, 4113-4119.

Chapter 3

Characterisation of shale cuttings: petrophysical properties and mechanical response

3.1 Introduction

The most traditional approach in geomaterials for characterising the mechanical response of rocks, is retrieving core samples from the desired depth and conducting conventional rock mechanics' tests such as uniaxial, triaxial and Brazilian tests. However, in the case of shales, as the most common sedimentary rock, there are relatively few laboratory-based studies where mechanical data have been measured on samples which have been well-characterised in terms of mineralogy and microstructure. In part, this is due to the chemical and mechanical instability of shales, which means that it is challenging and expensive to retrieve good quality core samples for undertaking conventional rock mechanics experiments (Kumar, 2012). Furthermore, because shales are heterogeneous on many scales (Aplin and Macquaker, 2011) and these heterogeneities vary significantly, it is difficult to extrapolate the data obtained from few core samples to the whole shale deposition (see Rybacki *et al.*, 2015). These problems, along with the incapability of well sonic log to measure the properties in the direction of parallel to the well, put serious challenge to mechanical characterisation of shale rocks, particularly the level of anisotropy (Abousleiman *et al.*, 2009).

In the past two decades, the use of instrumented indentation test has been one of the attractive topics in different engineering fields in which the mechanical characterisation of small volumes is of interest. Although this technique was initially developed to test metals and thin films (Oliver and Pharr, 1992, 2004), it was later adopted for inhomogeneous materials: tissues, biomaterials and cementitious composites (Constantinides and Ulm, 2003; Kruzic *et al.*, 2009; Duan *et al.*, 2015; Epshtein *et al.*, 2015). The high precision of indentation tests provides the opportunity to perform the test with very small penetration depths ($<$100 nm) on grid-based patterns to assess the mechanical response of different phases in a composite (Constantinides and Ulm, 2007; DeJong and Ulm, 2007; da Silva *et al.*, 2013; Bennett *et al.*, 2015). The speed and simplicity of this technique have made it an interesting tool for the shale industry. However, relatively few studies have been conducted on the possibility of using the indentation test on shale rocks. In some studies, indentation tests were conducted on shale samples with the highest possible load to measure the elastic response of the whole shale composite and good agreements were obtained between these results and elastic moduli obtained by Ultra-sonic Pulse Velocity (UPV) tests on core samples (Kumar, 2012; Kumar *et al.*, 2012; Abousleiman *et al.*, 2009). This is an important observation which reveals that perhaps, due to small elastic deformation in indentation tests, the measured elastic modulus shows more correlation with dynamic (acoustic) elastic modulus than the elastic modulus obtained from static test, such as uniaxial compression test. Therefore, when the term elastic modulus is used in this chapter, it refers to the measured modulus under small elastic deformation such as UPV test or indentation.

In addition to force controlled indentation testing, displacement controlled tests with very small penetration depths made it possible for the very first time to extract data on the mechanical response of the clay matrix (Ulm and Abousleiman, 2006). This new data set obtained by statistical analysis on the indentation results, provided valuable information on the source of anisotropy in clayey rocks. For instance, Babko and Ulm (2008) concluded that the intrinsic anisotropy of the solid unit of the clay matrix plays the major role in the macroscopic anisotropy of shale rocks. This was in contradiction with previous studies in which the solid unit of clay matrix was considered to be isotropic (Hornby *et al.*, 1994; Jakobsen *et al.*, 2003). Additionally, several researchers adopted this technique to measure the elastic modulus of the kerogen. Large pieces of kerogen were located using SEM imaging, then displacement controlled indentation was conducted on them (Zeszotarski *et al.*, 2004; Zargari *et al.*, 2013).

In this chapter, several shale samples are characterised in terms of mineralogy, porosity and total organic carbon (TOC). These information are critical to better understand the sources that control the macroscopic mechanical response of shales. In addition, such data provide the essential input parameters required for homogenisation models. Indentation tests are then performed on these samples in both parallel and perpendicular to bedding direction. Conducting indentation tests requires consideration of different details such as maximum load, loading rate, tip shape and load holding time. These factors will be investigated to further clarify their effects on the final results. The load-displacement-time curve for each indent is extracted and used to determine the elastic moduli and creep response of samples. Finally, the possible correlations between the mechanical response of the samples with their microstructural characterisation will be discussed to make some suggestion for performing indentation tests on shale rocks.

3.2 Indentation test: theory and details

The indentation tests generate mechanical properties of materials from their surface response. An indenter with known mechanical properties is pushed into a material surface with unknown properties. The continuous loading and unloading curves versus displacement and time are extracted to determine different mechanical parameters. In order to measure the mechanical properties at such small-scales accurately, both load and displacement are recorded very precisely with the accuracy of nanonewton (nN) and picometer (pm), respectively. Figure 3.1 shows a typical indentation machine equipped with an anti-vibration table and an isolation box to avoid any vibration effects coming from the ground/air and to increase the thermal stability of the system during the test.

Figure 3.1: A typical set up of an indentation machine.

3.2.1 Indentation test theory

The indentation test and its theory was initially presented by Oliver and Pharr (1992). In summary, while the force being applied, both the elastic and plastic response of the sample contribute to the displacement being recorded by the indenter. However, when the force is retracted only the elastic component of the recorded displacement is regained. Two material properties known as the indentation modulus (M) and hardness (H) can be calculated using the recorded load-displacement curve along with the deformation of the surface. For this purpose, the load-displacement curve is characterised in terms of P_{max} and h_{max}, which are the maximum force and the maximum penetration, respectively, and h_f which is the unrecoverable part of the total penetration. Moreover, the unloading curve related to elastic behaviour is also defined by its slope S. Figure 3.2 shows a load-displacement curve and the impression on the samples along with their characteristic parameters.

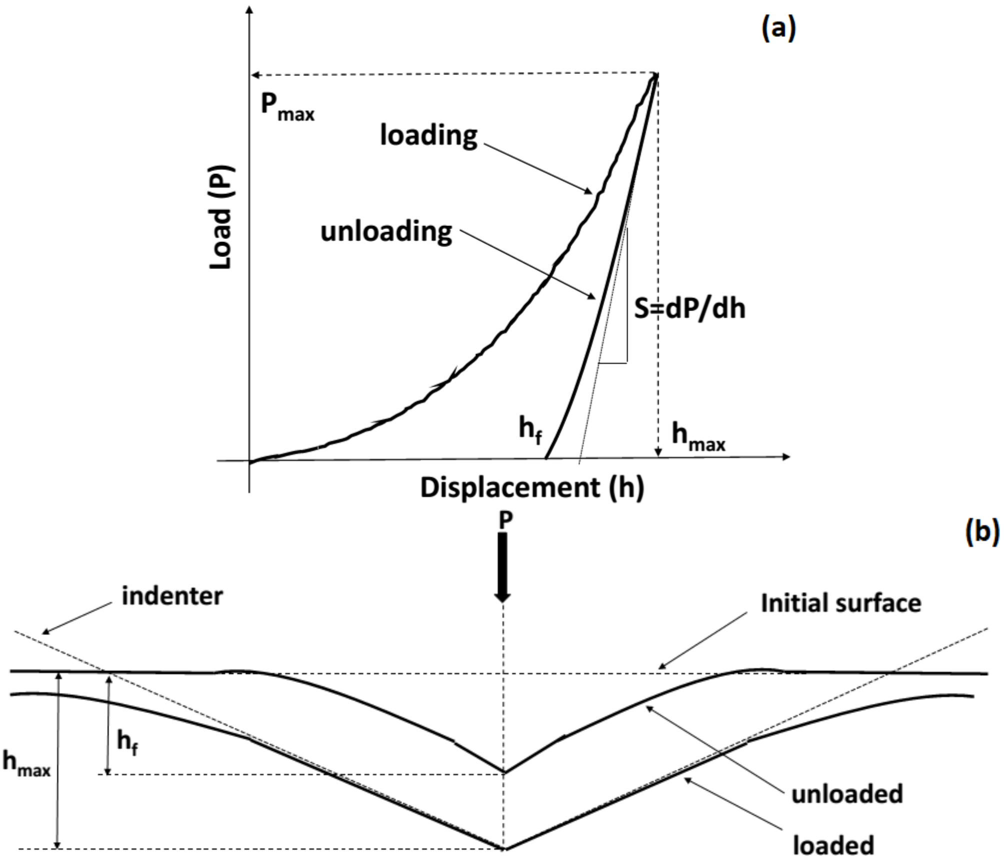

Figure 3.2: Load-displacement curve (a) and sample surface deformation during loading and unloading stages (b).

In order to calculate the material properties from indentation data, the slope of the unloading curve and contact area have to be determined. A power law relationship can be fitted over the unloading curve as:

$$P = \alpha(h - h_f)^m \tag{3.1}$$

The power law exponent, m, usually changes in the range of 1.2-1.6. The so-called contact stiffness, S can now be determined as:

$$S = \left.\frac{dP}{dh}\right|_{h_{max}} \tag{3.2}$$

The contact area (A$_c$) between the indenter and the sample surface depends on the indenter shape, and both penetration and residual depths. Theoretically, different shapes with axisymmetric geometry can be used for the indenter. However, Berkovich, cone and sphere indenters are commonly used due to better performance on standard samples (Figure 3.3).

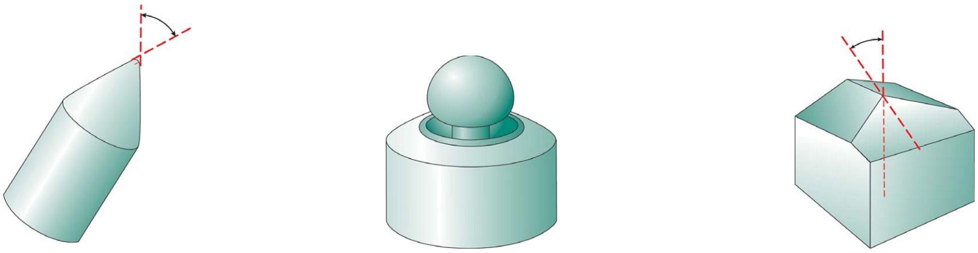

(a) Cone (b) Sphere (c) Berkovich

Figure 3.3: Different popular indenters used in indentation tests.

The relationship between indentation modulus (M), also known as reduced modulus (E*), with the contact area and the contact stiffness is:

$$M = \beta \frac{\sqrt{\pi}}{2} \frac{S}{\sqrt{A_c}} \tag{3.3}$$

$$M = \left(\frac{1 - \nu_s^2}{E_s} + \frac{1 - \nu_{tip}^2}{E_{tip}} \right)^{-1} \tag{3.4}$$

where β is a correction factor related to the tip shape, E is the Young's modulus, ν is the Poisson's ratio and subscripts s and tip represent the sample and tip, respectively. Tips are usually made of diamond with E=1141 GPa and ν=0.07. This elastic modulus is very high in comparison to the conventional samples, so the effect of tip deformation on the indentation modulus can be ignored. Defining material properties in Voigt notation (Eq. 3.5), the indentation modulus can be written as following for isotropic ($C_{11} = C_{33}; C_{12} = C_{13}; C_{44} = C_{66}$) and transversely isotropic materials (Delafargue and Ulm, 2004):

$$\begin{bmatrix} C_{11} & C_{12} & C_{13} & 0 & 0 & 0 \\ C_{12} & C_{11} & C_{13} & 0 & 0 & 0 \\ C_{13} & C_{13} & C_{33} & 0 & 0 & 0 \\ 0 & 0 & 0 & C_{44} & 0 & 0 \\ 0 & 0 & 0 & 0 & C_{44} & 0 \\ 0 & 0 & 0 & 0 & 0 & C_{66} \end{bmatrix} C_{66} = 0.5(C_{11} - C_{12}) \tag{3.5}$$

$$M = \frac{E}{1-\nu^2} = \frac{C_{11}^2 - C_{12}^2}{C_{11}} \tag{3.6}$$

$$M_3 = 2\sqrt{\frac{C_{11}C_{33} - C_{13}^2}{C_{11}}(\frac{1}{C_{44}} + \frac{2}{\sqrt{C_{11}C_{33}} + C_{13}})^{-1}} \tag{3.7}$$

$$M_1 = \sqrt{\frac{C_{11}^2 - C_{12}^2}{C_{11}}\sqrt{\frac{C_{11}}{C_{33}}}M_3} \tag{3.8}$$

where M_3 is the indentation modulus when the indenter is parallel to the axis of symmetry, and M_1 is the indentation modulus when the indenter is perpendicular to the axis of symmetry. For sedimentary rocks, the axis of symmetry is perpendicular to bedding direction. Therefore, M_3 is the modulus on section prepared parallel to bedding and M_1 is the modulus on sections prepared perpendicular to bedding.

The so-called hardness parameter which contains both the elastic and plastic response of the sample is defined as:

$$H = \frac{P_{max}}{A_c} \tag{3.9}$$

Generally, indentation tests are performed in high number to generate a good statistical description of the measured properties. The load-displacement curves are analysed automatically and calculated modulus and hardness are provided. However, all the data including load, displacement and time can also be recorded. For more description and details about the theory of indentation testing, readers are referred to Hay and Pharr (2000) and Oliver and Pharr (2004).

3.2.2 Effect of Poisson's ratio

The elastic property measured for the material beneath the indenter is an overall response. This means that the calculated modulus, for the simplest case of isotropic material, is a function of both Young's modulus and Poisson's ratio (see Eq. 3.6). Usually, in order to convert this measured modulus to Young's modulus, a Poisson's ratio has to be assumed for the material. Figure 3.4 shows the change in indentation modulus versus Poisson's ratio for two shale samples for which the mechanical properties have been well-characterised in both parallel and perpendicular directions to bedding (Hornby, 1998). With a simple calculation, it can be said that values of Poisson's ratio in the range 0.05-0.35, only change the calculated reduced elastic modulus by less than 12%.

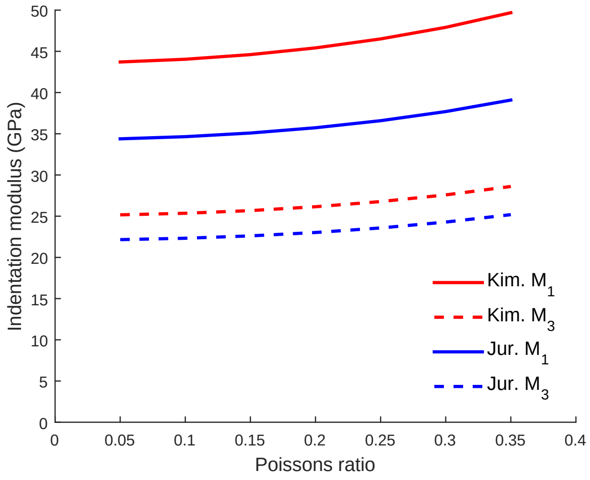

Figure 3.4: Indentation moduli versus Poisson's ratio for Kimmeridge (Kim.) and Jurassci (Jur.) shales.

In addition, shale is isotropic on the plane of bedding so the material response beneath the indenter is symmetric. However, when the indenter penetrates into a section perpendicular to bedding, two different Poissons's ratios are acting in different directions. One is related to the lateral response in a direction parallel to the plane of symmetry and the other is related to the lateral response in the direction perpendicular to the plane of symmetry. This means that the material response around the indenter is not symmetric. In order to avoid the mentioned problems about assuming a Poisson's ratio for the tested material, the indentation moduli are always reported in this study.

3.2.3 Time dependent response

The high accuracy and sensitivity of indentation machines allow for investigation of the time-dependent response of materials, also called creep. The applied load on the indenter can be kept constant at any level of loading to let the materials deform under constant loading. This capability has been used in different engineering applications to evaluate creep response in composites, polymers and glass (Beake *et al.*, 2007; Bell *et al.*, 2008; Dean *et al.*, 2013). The information obtained through this stage of the test is deformation versus time. Several relationships have been proposed to fit on this data and represent the creep of the sample (Chudoba and Richter, 2001; Cheng *et al.*, 2005; Beake, 2006). Eq. 3.10 originally proposed by Chudoba and Richter (2001) has proven to fit on creep indentation data very well for many different materials (Beake, 2006; Bell *et al.*, 2008).

$$\Delta h = A \ln(Bt + 1) \tag{3.10}$$

where Δ h is change in the position of the indenter, t is time, A and B are the material constants which can be used to compare creep response of different materials.

3.2.4 Thermal-drift calibration

The objective of thermal drift calibration is to correct the measured displacement for any small amount of thermal expansion or contraction of samples or machine. This correction is performed for every single indent. The procedure is that the load is kept constant at the end of the unloading stage for a fixed period of time, for example 50 s, and any displacement is measured during this time. The rate of thermal-drift is then calculated as the ratio of displacement to time. Imagine a rate of -0.05 nm/s was obtained for thermal drift. Then, a displacement recorded at 10 s into the test should be corrected by +0.5 nm. This calibration should be applied to all the recorded displacements in the test.

Hay and Pharr (2000) recommended that this constant loading stage for thermal-drift should be performed at low values of load, for example 10% of the maximum load, to reduce the effect of the time-dependent response on the measured rate. Therefore, this approach is commonly used for materials with very low or no time-dependent behaviour. For samples with noticeable creep, they proposed to place the sample into machine for a longer period of time to allow thermal equilibrium in the whole system. In addition, the temperature of the testing environment should be kept constant during the test.

As shale rocks exhibit significant creep response (Sone and Zoback, 2013; Mishra and Verma, 2015), the thermal-drift correction is not applicable for these rocks. Therefore, this correction will not be applied on the data, and all the displacement that occurs at the constant loading stages is assumed to be creep. In this study, the indentation tests are performed with a machine equipped with an isolation box with the best possible control over room temperature to avoid any thermal effect on the measured displacements.

3.3 Sample description

In this study, two sets of samples are considered to better cover different ranges of variability in mechanical and petrophysical properties of shale rocks. The first set of samples were selected from Posidonia shales with different maturity levels and also very different silt inclusion levels from 40 % to more than 80 % of volumetric silt grains. The second set of samples were all retrieved from a single well in the Toarcian shales of the Paris Basin at relatively similar depths. They have the same maturity level but contain different volume fractions, less than 40%, of mainly quartz inclusions.

3.3.1 Posidonia Shale

The Posidonia shale formation from the Lower Saxony Basin is a fine grained calcareous shale which contains a high amounts of organic matter, type II kerogen. This formation is among the earliest hydrocarbon-producing basins in the Europe and is now considered as one of the most important source rocks in Western Europe (Bruns *et al.*, 2013; Mathia, 2014). Here, three samples were selected from different boreholes, known as Wickensen, Harderode and Haddessen located in the Hils half-graben.

The mineralogical information of the samples were determined using X-ray powder diffraction (XRPD). In order to conduct XRPD measurement, the samples are ground in a mill with ethanol. The pastes are then spray dried to produce random powders. Figure 3.5 shows a typical XRPD output analysis. Table 3.1 provides the mineralogical information obtained through XRPD and some other petrophysical characterisations.

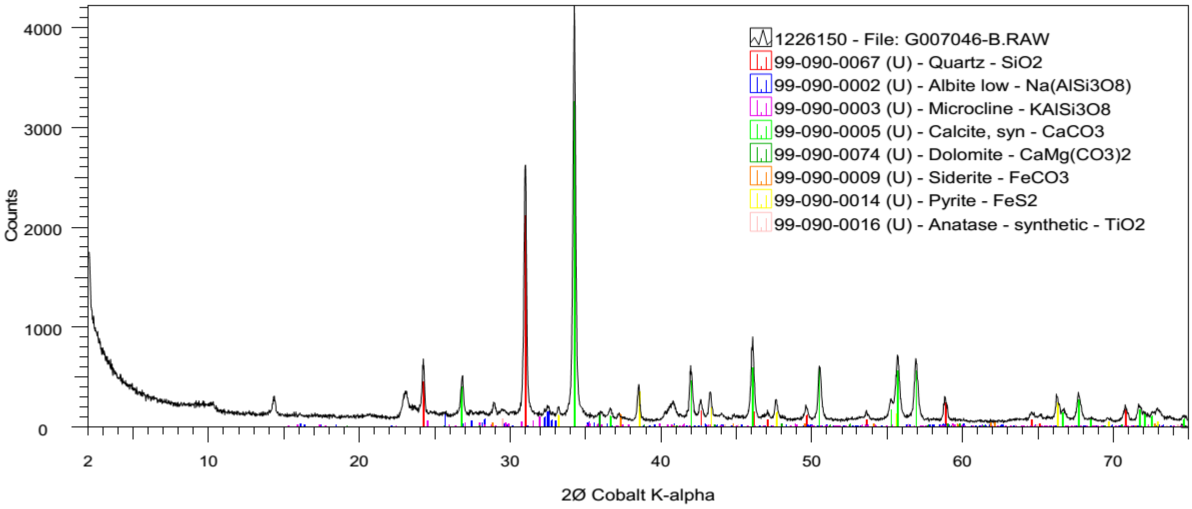

Figure 3.5: The output result for XRPD analysis of sample Har-46.

Table 3.1: Shale mineralogy in weight %.

Sample	Wic-29	Har-46	Had-27
Quartz	11.82	15.42	2.73
Feldspar	2.82	4.21	3.02
Calcite	33.78	40.72	14.55
Dolomite	0.88	1.31	63.6
Pyrite	4.59	4.6	5.37
Muscovite	0.35	2.16	0.58
I+I/S-ML	21.08	17.68	6.05
Chlorite(Tri)	1.62	0.84	0.58
Kaolinite	11.29	7.24	1.17
TOC	11.8	5.95	2.3
Vitrinite reflectance (Ro %)	0.53	0.89	1.45
Grain density, ρ_g (g/m^3)	2.263	2.538	2.898
Porosity, ϕ	10.3	4.8	7.3

The weight % data obtained by XRPD can be converted to volume fraction using the available grain densities in the literature (Mavko *et al.*, 2009). In addition, the kerogen volume fraction can now be determined as: 1−(total volume of grains+porosity). Table 3.2 summarises the calculated volumetric mineralogy for the Posidonia shale samples.

Table 3.2: Shale mineralogy in volume %.

Sample	Wic-29	Har-46	Had-27
Quartz	9.05	14.05	2.77
Feldspar	1.97	3.66	2.76
Calcite	25.3	36.3	14.43
Dolomite	0.62	1.11	59.56
Pyrite	1.85	2.22	2.88
Total silt inclusions	38.79	57.34	82.4
Total clay minerals	26.04	25.26	8.46
Kerogen	24.87	12.6	1.84

When such comprehensive characterisation is not available, empirical relationships have also been used in literature (Vernik and Nur, 1992; Carcione, 2000) in order to estimate the volumetric kerogen from the measured TOC in weight %. It is of interest to assess the accuracy of such empirical equations using the correct calculated volumetric kerogen. Eq. 3.11 was suggested by Vernik and Milovak (2011) for this purpose.

$$V_k = \frac{TOC\rho_b}{C_k\rho_k}; \quad \rho_b = (1-\phi)\rho_g \tag{3.11}$$

where C$_k$ is an empirical coefficient usually considered to be 0.75-.85, depending on maturity level, ρ_b is the bulk density, ρ_g is the grain density, ϕ is the porosity of the sample, ρ_k is the kerogen density and V_k is the volumetric kerogen content.

Considering suitable densities and empirical coefficients for each level of maturity, the kerogen volume fraction can be estimated for each sample (Table 3.3). The empirically estimated values for volumetric kerogen are almost equal to the calculated ones except for sample Had-27. In this sample, the calculated kerogen volume fraction is less than its weight %, which implies that the calculated value is incorrect. This might be due to the fact that the concentrations of both kerogen and clay mineral are very low and any small error in TOC measurement or XRPD data for clay particles can significantly affect the remaining volume left for kerogen in the calculation.

Table 3.3: Comparison of the calculated and empirically estimated kerogen volume fraction (Values of ρ_k and C_k were extracted from Okiongbo *et al.* (2005) and Vernik and Milovak (2011)).

Sample	Maturity	ρ_b	ρ_k	C_k	empirically estimated V_k	Calculated V_k
Wic-29	Immature	2.03	1.25	0.75	25.5	24.87
Har-46	Mature	2.41	1.3	0.8	13.8	12.55
Had-27	Over mature	2.68	1.4	0.85	5.2	1.84

3.3.2 Toarcian shales of the Paris Basin

The Toarcian shales of the Paris Basin are the lateral equivalent of the Northern European Posidonia shale, consisting of a sequence of marine shales deposited in the Tethys Ocean during the Early Jurassic. The Toarcian shales are rich in organic material and have shale oil potential (Jarvie, 2012). Our samples come from the Couy-1 well, which was drilled in 1986- 1987. Toarcian shales are located between 210 m and 355 m (Pradier and Gauthier, 1987).

Core samples of the Toarcian shales were selected from different depths based on the quality of the samples. The recently developed Quantitative Evaluation of Minerals by Scanning electron microscopy (QEMSCAN) analysis, was used to determine the mineralogy of the selected samples. QEMSCAN is an automated mineralogy method that combines electron microscopy with energy dispersive x-ray spectroscopy for quantitative mineralogical analysis of the rock sample. The system directly measures the volumetric portion of each mineral in the analysed section. The volume fractions obtained over both sections parallel and perpendicular to bedding might be slightly different, so the averaged values were reported here. Figure 3.6 shows digital mineralogical image generated by QEMSCAN analysis. It should be noted that QEMSCAN cannot differentiate between organic matter and porosity due to the very low density of this phase. Therefore, the TOC needs to be analysed separately. Table 3.4 provides information including: mineralogical description, TOC, Tmax index and bulk density for the selected samples. It should be noted that in order to convert the TOC in weight % to kerogen volume %, the empirical formula (Eq. 3.11), which was assessed in the previous section, was adopted. The values of Tmax are less than 435 which implies that the shale samples are immature. Therefore, the empirical coefficient of α was considered to be 0.75 and a value of 1.25 g/cm^3 was selected for kerogen density.

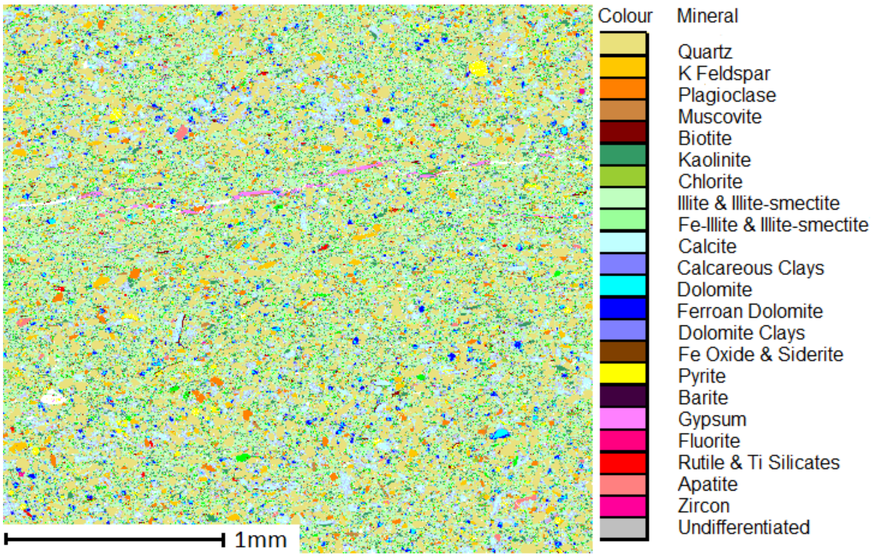

Figure 3.6: QEMSCAN image based on combination of SEM and EDS digital images.

Table 3.4: Rock-eval and volumetric mineralogical data for the Toarcian shale samples.

Sample ID	2	6	8	10
Quartz	29.33	6.5	9.28	25.63
Calcite	0.8	7.4	9.6	5.84
Pyrite	0.3	1.11	6.05	2.69
Feldspar	3.55	0.21	0.58	2.6
Dolomite	1.45	2.7	1.59	1.14
Total silt inclusions	35.43	17.92	27.1	37.9
Kerogen, V_K	3.2	5.6	19.5	3.2
Porous Clay	61.32	87.68	53.4	58.9
Tmax	432	430	419	432
TOC (Weight %)	1.13	1.98	7.5	1.13
Bulk density,ρ_b (g/m^3)	2.65	2.67	2.45	2.66
Depth (m)	224.9	340	347.5	202.5

3.4 Indentation test: analysis and results

For each shale sample, two sections, parallel and perpendicular to bedding, were prepared. The procedure for sample polishing and surface preparation is the same as in the AFM test and was described in the previous chapter. Tests were performed using the Berkovich and also sphere indenters, along with a force-controlled condition with the maximum possible load on the machine. Such a high load was applied in order to create the maximum possible contact area and to obtain the best surface response of the whole shale composite. The tests were performed on a grid, with 100 μm distance between each indent. This distance is required to avoid any interaction between two disturbed zones beneath each indent. In addition, due to the complex nature of shale, even at the scale of a few microns, a large number of indents must be conducted in order to obtain a robust statistical description of the mechanical response.

3.4.1 Posidonia Shale

The indentation test procedure involves several details which need to be carefully considered in order to achieve reliable results. For instance, maximum displacement/loading, type of indenter, loading/unloading rate, load holding time, etc. As mentioned before, the maximum load, 500 mN in this case, was applied to better capture the response of the overall microstructure of the shale samples. Theoretically, indentation can be conducted with any tip shape; however, the geometry of the tip might affect the frictional force along the contact surface, which could slightly change the load-displacement curve. This issue will be investigated using two indenters, Berkovich and sphere. It is normal procedure to hold the load at the peak for a few seconds before the unloading stage. This is considered to allow the system to reach equilibrium, thermally and mechanically. In addition, a loading/unloading rate has to be defined for the machine in such a way that every single indent does not take too long and also to allow the system to remain in a quasi-static loading condition. As shale rocks are known for their time-dependent behaviour, a sensitivity analysis has to be performed initially to clarify any possible effect of these rates on the final results.

It was considered to conduct the associated tests for a sensitivity analysis on one shale disc to minimize the effect of local variability in shale mechanical properties. Indentation testing was carried out with immediate reloading after reaching the maximum load and also with 10 s and 120 s of holding time at 500 mN load. In addition, different loading rates of 50 mN/s and 16.667 mN/s were considered. Table 3.5 summarises the results of all tests. It can be concluded that the indentation test is robust enough and not noticeably sensitive to the chosen parameters.

Slight change, in the results can be attributed to the natural heterogeneity of shale itself. An important observation is that, although shale shows significant creep response under constant maximum load and this creep may compact the clay matrix, the observed elastic response during unloading almost remains constant. In fact, the elastic modulus is not significantly dependent on the creep history. This is an important observation which allows for accurate measurement of both elastic response and creep behaviour at the same time through one set of tests.

Table 3.5: Sensitivity analysis on indentation test.

Sample ID	Loading rate (mN/s)	Unloading rate (mN/s)	Holding time (s)	Indenter	Modulus, M (GPa)
Wic-29	50	50	0	Berkovich	14.95±1.9
Wic-29	50	50	10	Berkovich	14.10±0.8
Wic-29	16.667	50	10	Berkovich	14.68±0.4
Har-46	50	50	10	Berkovich	26.90±1.8
Har-46	50	50	120	Berkovich	27.17±1.4
Had-27	50	50	120	Berkovich	39.50±6.0
Had-27	50	50	120	Sphere	39.00±8.2

Indentation testing on composite-like materials are challenging, especially if the goal is to capture the overall mechanical response of the composite. In fact, the ideal condition is when the contact area is much larger than the size of each constituent. In such condition, the indentation load-displacement curve should be reproducible. Figure 3.7 illustrates the load-displacement curves for the three shale samples. It can be clearly observed that almost all the indents on sample Wic-29 and Har-46 are consistent, which leads to more reliable statistical description. However, the load-displacement curves for sample Had-27 are more scattered, leading to a higher standard deviation (SD).

In order to better understand the distribution of measured properties, the histogram of indentation moduli were also produced (Figure 3.8). Unlike the samples of Wic-29 and Har-46 which show clear peaks and almost normal distributions on the measured elastic moduli, the data on sample Had-27 are not concentrated around a specific value and are distributed over a wide range. In fact, the measured properties in the last sample are not concentrated around any specific values. Therefore, it can be concluded that the measured properties for this sample are less accurate. This problem can be attributed to the small contact area during the test in comparison to the size of the sample's micro-components. Figure 3.9 shows the microscopic image of the indented areas. It is obvious that the indentation contact area is not large enough to fully affect the overall microstructure of the sample Had-27. However, the averaged values, obtained through several sets of indentation tests on different sections of this sample, are still quite consistent (see Table 3.5).

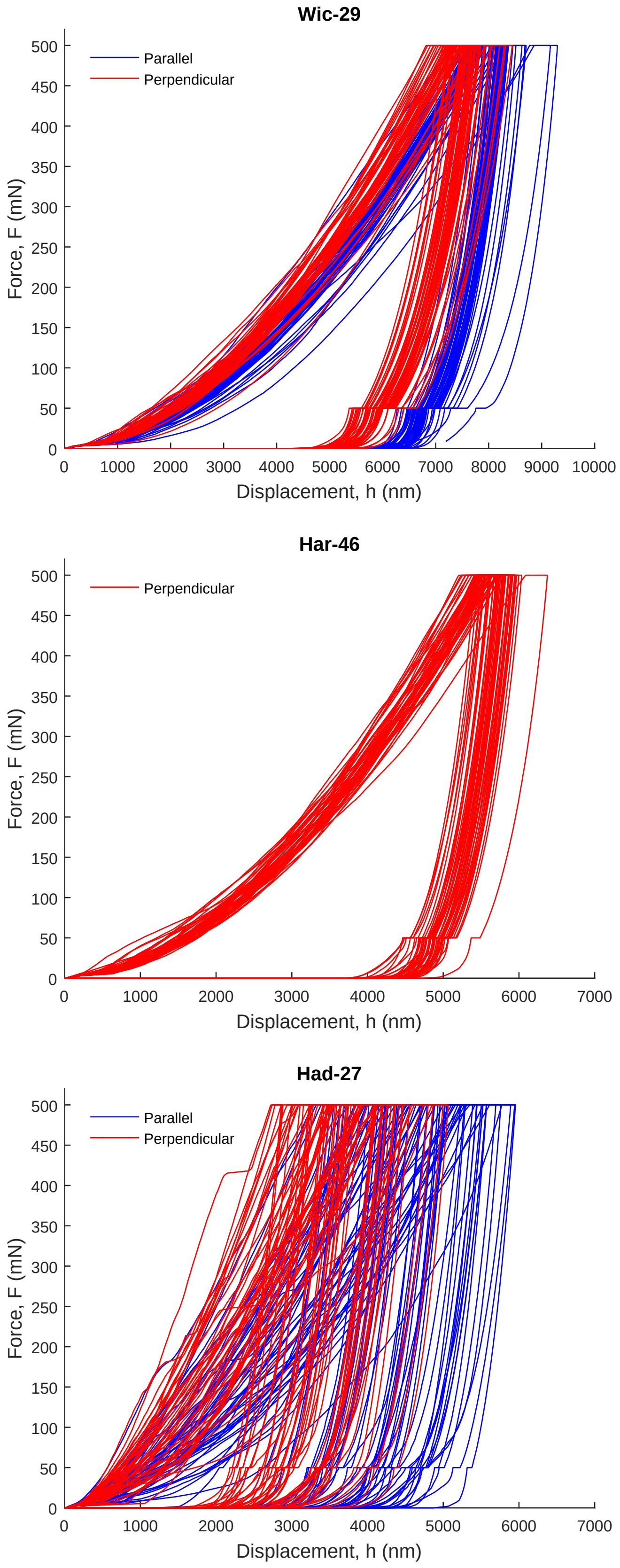

Figure 3.7: Load-displacement curves for the three Posidonia shales on sections parallel and perpendicular to bedding.

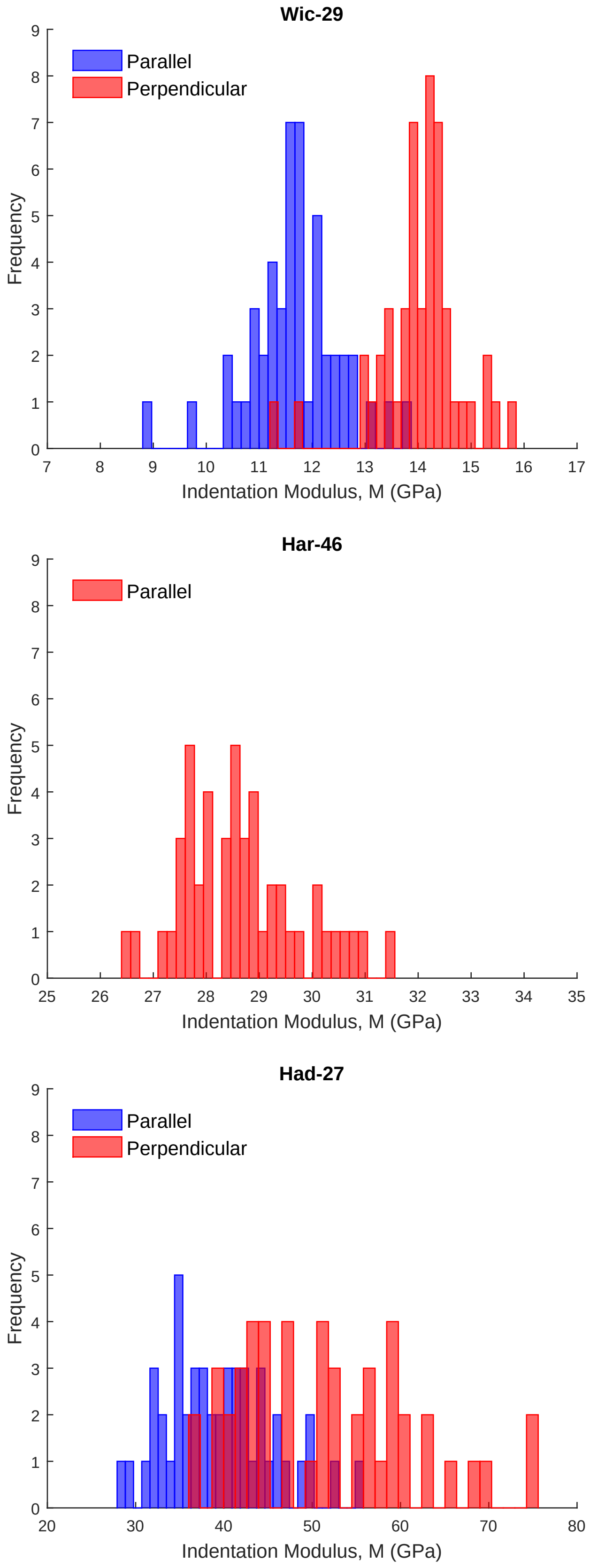

Figure 3.8: Histogram of indentation modulus of Posidonia Shale samples.

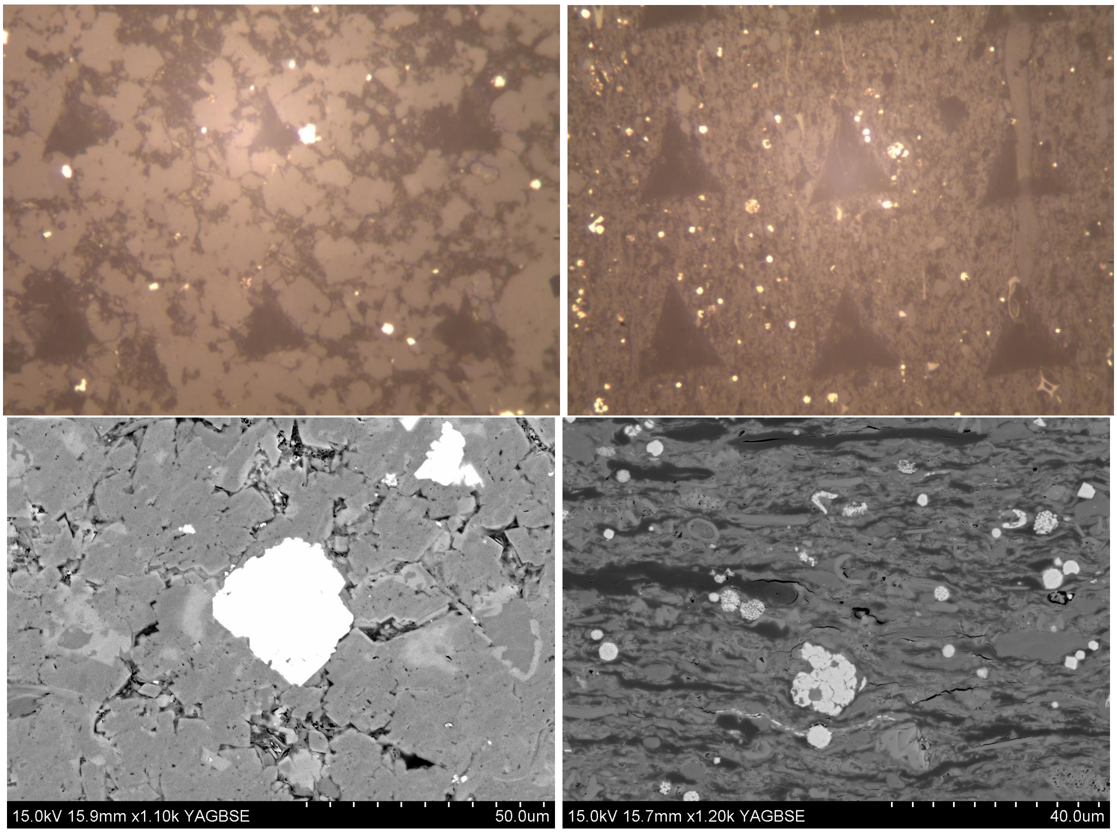

Figure 3.9: Microscopic and SEM images on sample Wic-29 (right), and Har-27 (left) (The distance between the centres of two adjacent indents is 100 μm).

The final indentation modulus and hardness of Posidonia shale samples, obtained from a total number of 49 indents on a square pattern, are provided in Table 3.6 and 3.7. Considering the indentation results and mineralogical information (Table 3.1), it can be concluded that an increase in TOC can significantly alter the mechanical properties. In addition, the observed thin layered shape of organic matter in SEM images, has led to a general conclusion that an increases in the kerogen content of a sample, enhances the anisotropy ratio (Vernik and Nur, 1992). However, the results obtained on Posidonia shale samples do not confirm this conclusion.

It is worth noting that the hardness measured on sample Wic-29 on the section perpendicular to bedding, is smaller than the value obtained for the section parallel to bedding. This slight error might be due to surface roughness, which consequently produces some error in the estimation of contact area. Figure 3.10 shows the microscopic image of this sample. It can be seen that the axis of the microscope is not completely perpendicular to the sample surface which can be interpreted as a slight inclination on the surface. This error has little effect on the indentation modulus. The reason is that the contact area is directly used in the hardness formula (see Eq. 3.9), while its square root appears in the calculation of the indentation modulus (see Eq. 3.3), which consequently reduces any adverse effect of an error in the estimation of this parameter.

Table 3.6: Indentation moduli (GPa).

Sample ID	M_1		M_3		Anisotropy ratio (M_1/M_3)
	Mean	SD	Mean	SD	
Wic-29	14.1	0.8	11.7	0.9	1.2
Har-46	28.6	1.2	—	—	—
Had-27	51.5	9.9	39.5	6.0	1.3

Table 3.7: Hardness.

Sample ID	H_1		H_3		Anisotropy ratio (H_1/H_3)
	Mean	SD	Mean	SD	
Wic-29	0.35	0.02	0.43	0.03	0.81
Har-46	0.71	0.05	—	—	—
Had-27	1.55	0.56	1.11	0.39	1.39

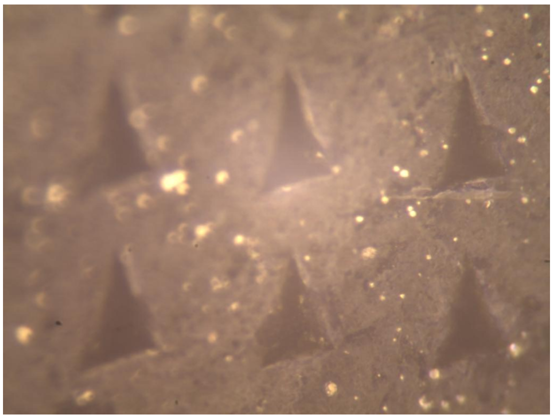

Figure 3.10: Microscopic image of sample Wic-29 on the section perpendicular to bedding.

As discussed before, indentation has the capability of holding a constant load and recording the displacement accurately which can be used to study the time-dependent response of materials. Here, the maximum load of 500 mN was kept constant for 120 s to record the creep response in these shale samples. Time-displacement data obtained from every single indent were analysed, and a logarithmic curve (Eq. 3.10) was fitted to the data. Figure 3.11 shows the averaged fitted curve over the indentation results. As it can be observed, the creep response of sample Had-27, for which both sections were tested, shows anisotropy. The ratio of this anisotropy is 1.36 which is quite comparable with the ratio of 1.3 obtained for indentation modulus (see Table 3.6). In this sample, the clay minerals and TOC contents are much lower in comparison to the other samples, which can justify the much lower recorded creep deformation. Comparing the results for samples Wic-29 and Har-46, it can be said that Wic-29 shows approximately two times more deformation then Har-46. These two samples have almost equal amounts of clay minerals, which are normally considered to be the source of creep behaviour in shales; however, Wic-29 and Har-46 contain significantly different volumes of kerogen (24.8 and 12.6 %, respectively), which explains the cause of the difference in their creep deformation and highlights the importance of kerogen on the time-dependent response of shale rocks. In general, it can be concluded that the creep response in shales is controlled by both clay minerals and kerogen.

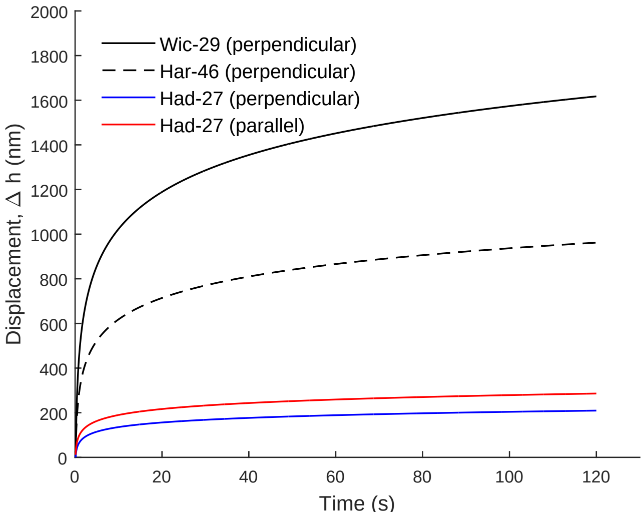

Figure 3.11: Displacement-time curves obtained on Posidonia shale samples for 120 s at a constant force of 500 mN.

Figure 3.12 shows the final creep deformation at 120 s versus the clay and kerogen content, and a strong correlation between them can be observed. A quadratic second-order equation can be fitted over the creep data obtained on the section perpendicular to the bedding direction with R^2=0.99 . Sone and Zoback (2013) also conducted creep test on shale core samples in a triaxial cell and observed a similar nonlinear correlation between creep results and clay+TOC content. In fact, it can be concluded that although the indentation is a small scale testing technique, it can correctly capture the trend of the mechanical responses of the samples.

3.4.2 Toarcian shales of the Paris Basin

The indentation test was conducted on these samples with a different machine, with a maximum load of 400 mN. This force generated indentation depths from 3.5 μm to 6.5 μm, depending on the sample stiffness. Here, on average, around 80 indentations were conducted on each surface to characterise its mechanical response. No time-dependent response was studied for these

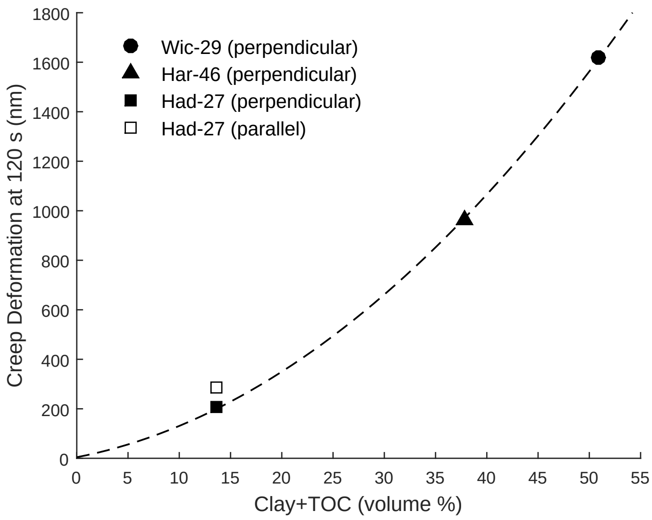

Figure 3.12: Creep deformation at 120 s versus clay and kerogen content along with a fitted curve over the data obtained perpendicular to bedding.

samples and only conventional indentation tests were performed.

An important issue is that the indentation data usually contains some out-of-range values which might be caused by the indenter touching a large silt grain or a large pore space, generating very high or very low penetration depths, respectively. A judgment is required to filter the out-of-range data and to eliminate their effects on the calculation of mean and standard deviation of shale material properties. Figure 3.13 shows the raw indentation results on samples No. 6 and 8 with some clear out-of-range data.

Table 3.8 provides indentation moduli taken in different directions for Toarcian shale samples. In addition, as all these samples were retrieved from the same shale layer, it is of interest to compare them in terms of anisotropy. In order to better understand the source of anisotropy in these samples, the anisotropy ratio (M_1/M_3) versus kerogen volume fraction is plotted (Figure 3.14). Considering the volume fractions of both kerogen and silt inclusions, it can be said that an increase in kerogen does not increase the anisotropy ratio, but reduces both indentation moduli significantly. Although similar results were observed for Posidonia Shale samples in the previous section, this might again seem in contradiction with the general idea that there is a direct correlation between anisotropy and kerogen volume fraction (Vernik and Nur, 1992). However, based on several experimental data reported in Vernik and Landis (1996), on the kerogen volume fraction versus the Thomsen anisotropic parameter, $\epsilon = C_{11} - C_{33}/(2C_{33})$, it can be said that this is only a tentative conclusion. In fact, the reported data are scattered particularly on immature samples (Vernik and Nur, 1992) which further highlights the difficulties involved

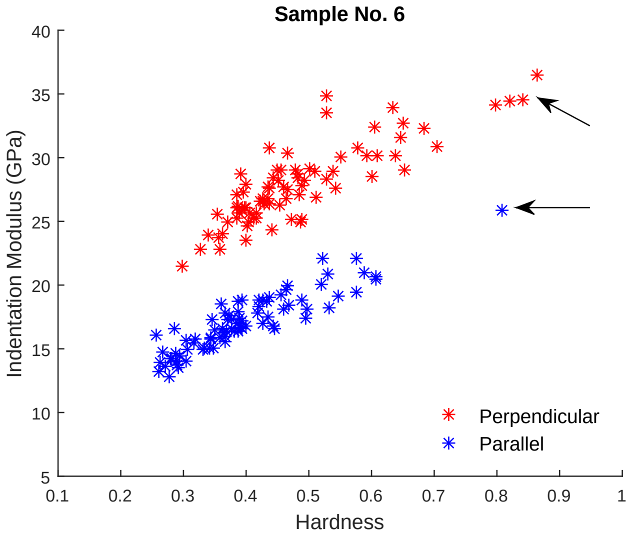

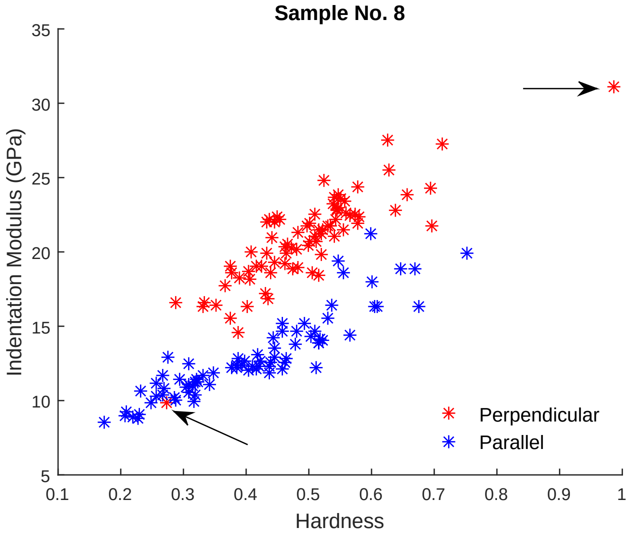

Figure 3.13: Indentation modulus versus hardness on section parallel and perpendicular to bedding direction for samples No. 6 and 8 (Arrows point towards possible out-of-range data).

in determination of the main parameters affecting shale anisotropy.

Table 3.8: Indentation moduli (GPa).

Sample ID	M_1		M_3		Anisotropy ratio (M_1/M_3)
	Mean	S.D.	Mean	S.D.	
2	30.3	7.7	17.2	7.3	1.76
6	27.4	2.7	17	2.1	1.61
8	20.6	2.8	12.6	2.5	1.63
10	28.5	7.6	—	—	—

Table 3.9 provides the so-called dimensionless material property of hardness. Unlike the elastic moduli, the anisotropy ratio is lower for hardness except for sample 2, for which hardness shows a very high standard deviation. It can be roughly concluded that the hardness is not as

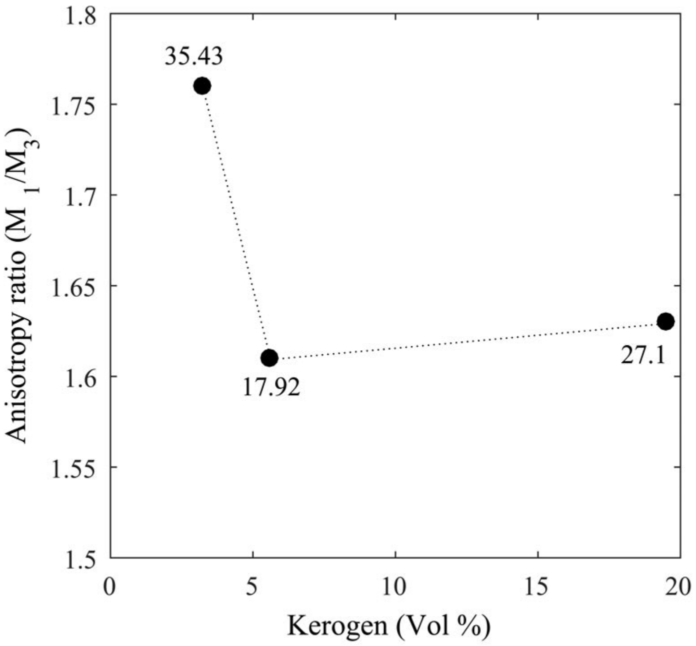

Figure 3.14: Anisotropy versus the kerogen volume fraction (Data label is the total silt inclusions volume fraction).

anisotropic as the indentation modulus. This could be justified by considering the properties that contribute to the hardness. This material property is a function of both elastic and plastic response. Therefore, it can be said that the plastic response of shales beneath the indenter in parallel and perpendicular to bedding is not highly anisotropic and only the elastic part of the hardness is contributing to its anisotropy. This is supported by many experimental studies, in which core samples drilled parallel and perpendicular to bedding showed almost identical uniaxial compression strength (Vales *et al.*, 2004; Ewy *et al.*, 2010; Cho *et al.*, 2012).

Table 3.9: Hardness.

Sample No.	H_1		H_3		Anisotropy ratio (H_1/H_3)
	Mean	S.D.	Mean	S.D.	
2	0.8	0.39	0.46	0.31	1.74
6	0.46	0.09	0.39	0.09	1.18
8	0.49	0.08	0.41	0.12	1.19
10	0.76	0.9	—	—	—

3.5 Conclusion

In this chapter, several shale samples were characterised in terms of both petrophysical and mechanical properties. Both XRPD and QEMSCAN analyses were implemented on these samples to determine the mineralogical compositions and the mechanical response, parallel and perpendicular to bedding, were evaluated using indentation testing.

Sensitivity analysis was carried out on different aspects of the indentation test including: loading rate, indenter shape and load holding time. It was observed that although shale samples show a significant time dependent response, the measured elastic moduli is not significantly sensitive to the loading rate or the load holding time at the maximum load. This could allow for simultaneous measurement of the elastic and time-dependent response. In addition, it proves the consistency and reliability of the indentation test for the case of shale rocks.

The obtained load-displacement curves, the plot of indentation modulus versus hardness and the microscopic image of the samples were carefully investigated. It was found out that, for shales with higher elastic moduli, roughly more than 30 GPa, the indentation measurements are more scattered. This problem can be partly attributed to the microstructure of these shales, formed by large grains (>20 μm), which cannot be fully captured by the small contact area of the indentation test. Additionally, reduction in porosity and TOC, or increase in silt inclusions can significantly increase the stiffness of shale. As the conventional indentation machines have limited capacities for the maximum load (normally less than < 500 mN), an increase in stiffness reduces the penetration depth and consequently the contact area. This further increases the influence of one constituent on the recorded load-displacement curve. This issue can be clearly seen in sample Had-27 of Posidonia shale, and samples 2 and 10 of Toarcian shales. In summary, it can be said that the current indentation machines in the market are not suitable for testing all types of shale samples and an increase in the capacity of the maximum applied force is essential.

The time-dependent response of shales, considered to originate from clay minerals, was studied by holding a constant load for a specific period of time in the indentation tests. The creep response was also found to be anisotropic, similar to the elastic moduli. Moreover, two samples containing an almost equal amount of clay minerals but different kerogen contents showed noticeably different creep responses. This can be translated to the significant time-dependent behaviour of kerogen and its non-negligible effect on overall creep in shale rocks. Comparing the creep deformation with the clay+TOC content of the samples, a strong nonlinear correlation was observed.

The indentation tests were conducted in high numbers to generate a robust statistical description on the measured properties. The plot of indentation modulus versus hardness was used to assess these measurements. It was observed that some indents show out-of-range values and their consideration can noticeably affect the mean value. These data can be detected by very high or very low penetration depth, and a judgment is required to ignore these values in the final calculation.

Finally, the Toarcian shales, which were retrieved from the same well with a similar level of maturity, were considered to evaluate the relationship of anisotropy and the shale characterisations. It was observed that an increase in the kerogen volume fraction does not necessarily translate into anisotropy. However, kerogen content significantly reduces both elastic moduli. This observation was supported by the results obtained on Posidonia Shale samples.

In addition to the limitations and capabilities of indentation testing, summarized above, the following points can be concluded. First, while indentation testing on shale samples is limited to two values of indentation moduli on sections parallel and perpendicular to bedding direction (unlike the UPV), it is a fast and relatively easy test to generate some reliable data on the magnitude of elastic stiffness and anisotropy of shales. Second, there is no need for good quality core samples, which is rarely available for shales. A small amount of shale cuttings is enough to prepare the suitable thin-sections for indentation testing.

References

Abousleiman Y., Tran M., Hoang S., Ortega J.A., Ulm F.J. 2009. Geomechanical field characterization of the two prolific U.S. mid-West gas plays with advanced wire-line logging tools. SPE Annual technical conference and exhibition, New Orleans, Louisiana, USA. SPE 124428.

Aplin A.C., Macquaker H.S. 2011. Mudstone diversity: Origin and implications for source, seal, and reservoir properties in petroleum systems. *Association of Petroleum Geologists Bulletin*, **95**, 2031-2059.

Bennett K.C., Berla L.A., Nix W.D., Borja R.I. 2015. Instrumented nanoindentation and 3D mechanistic modeling of a shale at multiple scales. *Acta Geotechnica*, **10**, 1-14.

Bobko C., Ulm F.J. 2008 The nano-mechanical morphology of shale. *Mechanics of Material*, **40**, 318-337.

Beake B. 2006. Modelling indentation creep of polymers: a phenomenological approach. *Journal of Physics D: Applied Physics*, **39**, 4478-4485.

Beake B., Bell G.A., Brostow W., Chonkaew W. 2007. Nanoindentation creep and glass transition temperatures in polymers. *Polymer International*, **56**, 773-778.

Bell G.A., Bielinski D.M., Beake B. 2008. Influence of Water on the Nanoindentation Creep Response of Nylon 6. *Journal of Applied Polymer Science*, **107**, 577-582.

Bruns B., Primio R., Berner U., Littke R. 2013. Petroleum system evolution in the inverted Lower Saxony Basin, northwest Germany: a 3D basin modeling study. *Geofluids*, **13**, 246-271.

Carcione J.M. 2000. A model for seismic velocity and attenuation in petroleum source rocks. *Geophysics*, **65**(4), 1080-1092.

Cheng L., Xia X., Scriven L.E., Gerberich W.W. 2005. Spherical-tip indentation of viscoelastic material. *Mechanics of Materials*, **37**, 213-226.

Cho J.W., Kima H., Jeon S., Min K.B. 2012. Deformation and strength anisotropy of Asan gneiss, Boryeong shale, and Yeoncheon schist. *International Journal of Rock Mechanics and Mining Sciences*, **50**, 158-169.

Chudoba T., Richter F. 2001. Investigation of creep behaviour under load during indentation experiments and its influence on hardness and modulus results. *Surface and Coatings Technology*, **148**, 191-198.

Constantinides G., Ulm F.J. 2003. On the use of nanoindentation for cementitious materials. *Materials and Structures*, **36**, 191-196.

Constantinides G., Ulm F.J. 2007. The nanogranular nature of C-S-H. *Journal of the Mechanics and Physics of Solids*, **55**, 64-90.

da Silva W.R.L., Nemecek J., Stemberk P. 2013. Application of multiscale elastic homogenization based on nanoindentation for high performance concrete. *Advances in Engineering Software*, **62–63**, 109-118.

Dean J., Bradbury A., Aldrich-Smith G., Clyne T.W. 2013. A procedure for extracting primary and secondary creep parameters from nanoindentation data. *Mechanics of Materials*, **65**, 124-134.

DeJong M., Ulm F.J. 2007. The nanogranular behavior of C-S-H at elevated temperatures (up to 700 C). *Cement and Concrete Research*, **37**, 1-12.

Delafargue A., Ulm F.J. 2004. Explicit approximations of the indentation modulus of elastically orthotropic solids for conical indenters. *International Journal of Solids and Structures*, **41**, 7351-7360.

Duan P., Bull S., Chen J. 2015. Modeling the nanomechanical responses of biopolymer composites during the nanoindentation. *Thin Solid Films*, **596**, 277-281.

Epshtein S.A., Borodich F.M., Bull S.J., 2015. Evaluation of elastic modulus and hardness of highly inhomogeneous materials by nanoindentation. *Applied Physics A*, **119**, 325-335.

Ewy R.T., Bovberg C.A., Stankovic R.J. 2010. Strength anisotropy of mudstones and shales. 44^{th} US Rock Mechanics Symposium and 5^{th} U.S.-Canada Rock Mechanics Symposium, held in Salt Lake City, UT June 27-30.

Jakobsen M., Hudson J.A., Johansen T.A. 2003. T-matrix approach to shale acoustics. *Geophysical Journal International*, **154**, 533-558.

Jarvie D.M. 2012. Shale resource systems for oil and gas: Part 2 – Shale-oil resource systems. In: Breyer, J.A. (ed.) Shale reservoirs – Giant resources for the 21st century. AAPG Memoir 97, pp. 89-119.

Hay J.L., Pharr G.M. 2000. Instrumented Indentation Testing. ASM Handbook, 232-243.

Hornby B.E., Schwartz L., Hudson J. 1994 Anisotropic effective medium modeling of the elastic properties of shales. *Geophysics*, **59**, 1570-83.

Hornby B.E. 1998. Experimental laboratory determination of the dynamic elastic properties of wet, drained shales. *Journal of Geophysical Research*, **103**(B12), 29945-29964.

Kruzic J.J., Kim D.K., Koester K.J., Ritchie R.O. 2009. Indentation techniques for evaluating the fracture toughness of biomaterials and hard tissues. *Journal of mechanical behaviour of biomedical materials*, **2**(4), 384-395.

Kumar V. 2012. Geomechanical Characterization of Shale Using Nano-indentation. MSc dissertation, University of Oklahoma.

Kumar V., Sondergeld C.H., Rai C.S., 2012. Nano to macro mechanical characterization of shale. SPE Annual technical conference and exhibition, San Antonio, Texas, USA. SPE 159804.

Mathia E.J. 2014. Geological evaluation of Posidonia and Wealden organic-rich shales: geochemical and diagenetic controls on pore system evolution. PhD thesis. Newcastle University.

Mavko G., Mukerji T., Dvorkin J. 2009. The Rock Physics Handbook. Cambridge University Press.

Mishra B., Verma P. 2015. Uniaxial and triaxial single and multistage creep tests on coal-measure shale rocks. *International Journal of Coal Geology*, **137**, 55-65.

Mondal P., Shah S.P., Marks L. 2007. A reliable technique to determine the local mechanical properties at the nanoscale for cementitious materials. *Cement and Concrete Research*, **37**, 1440-1444.

Okiongbo K.S., Aplin A.C., Latter S.R. 2005. Changes in Type II Kerogen Density as a Function of Maturity: Evidence from the Kimmeridge Clay Formation. *Energy & Fuels*, **19**(6), 2495-2499.

Oliver W.C., Pharr G.M. 1992. An improved technique for determining hardness and elastic modulus using load and displacement sensing indentation experiments. *Journal of Materials Research*, **7**, 1564-83.

Oliver W.C., Pharr G.M. 2004. Measurement of hardness and elastic modulus by instrumented indentation: advances in understanding and refinements to methodology. *Journal of Materials Research*, **19**(1), 3-20.

Pradier B., Gauthier B. 1987. Etude preliminaire de la matiere organique sedimentaire. In: Lorenz Cl. (ed.) Geologie profonde de la France, forage scientifique de Sancerre-Couy. Documents du BRGM n136, Bureau de recherches geologiques et minieres, 103-118.

Rybacki E., Reinicke A., Meier T., Makasi M., Dresen G. 2015. What controls the mechanical properties of shale rocks? – Part I: Strength and Young's modulus. *Journal of Petroleum Science and Engineering*, **135**, 702-722.

Sone H., Zoback M.D. 2013. Mechanical properties of shale-gas reservoir rocks - Part 1: Ductile creep, brittle strength, and their relation to the elastic modulus. *Geophysics*, **78**(5), D393-D402.

Ulm F.J., Abousleiman Y. 2006. The nanogranular nature of shale. *Acta Geotechnica*, **1**, 77-88.

Vales F., Nguyen Minh D., Gharbi H., Rejeb A. 2004. Experimental study of the influence of the degree of saturation on physical and mechanical properties in Tournemire shale (France).

Applied Clay Science, **26**, 197-207.

Vernik L., Nur A. 1992. Ultrasonic velocity and anisotropy of hyrdocarbon source rocks. *Geophysics*, **57**(5), 727-735.

Vernik L., Landis C. 1996. Elastic anisotropy of source rocks: Implication for HC generation and primary migration. *AAPG Bulletin*, **80**, 531-544.

Vernik L., Liu X. 1997. Velocity anisotropy in shales: A petrophysical study. *Geophysics*, **62**(2), 521-532.

Vernik L., Milovac J. 2011. Rock physics of organic shales. *The Leading Edge*, **30**, 318-323.

Zargari S., Prasad M., Mba K.C., Mattson E.D. 2013. Organic maturity, elastic properties, and textural characteristics of self resourcing reservoirs. *Geophysics*, **78**(4), D223-D235.

Zeszotarski J.C., Chromik R.R., Vinci R.P., Messmer M.C., Michels R., Larsen J.W. 2004. Imaging and mechanical property measurements of kerogen via nanoindentation. *Geochimica et Cosmochimica Acta*, **68**, 4113-4119.

Chapter 4

Predicting the elastic response of organic-rich shale using homogenisation

4.1 Introduction

Shale, or mudstone, is the most common sedimentary rock: a heterogeneous, multi-mineralic natural composite consisting of clay mineral aggregates, organic matter and variable quantities of minerals such as quartz, calcite and feldspar. High heterogeneity of these rocks has inspired many researches, in which correlations between macroscopic mechanical properties and the compositional variabilities of shales have been studied (Kumar *et al.*, 2015; Rybacki *et al.*, 2015). However, in order to systematically account for the microstructure, another approach is to adopt micro-mechanical models that have been widely used in the field of composite engineering (Klusemann and Svendsen, 2010; Mortazavi *et al.*, 2013). In these methods, the macroscale mechanical behaviour of a composite is determined from the mechanical response of each constituent, along with their interaction with each other. This modelling approach is in principle well suited to shale, the mechanical properties of which are likely to depend on the porosity, the volume fraction of different mineral and the amount of organic matter (Sayers, 2013a). In addition, the mechanical properties of the elementary building block of clay, as the most important constituent of shales, are not easy to quantify. This micron-size constituent, which is called clay particle or solid unit of clay, along with sub-micron-size voids form a natural composite called the porous clay. Homogenisation could also be used to back-calculate the mechanical properties of the solid unit of clay from porous clay, which is available in macro scale.

In order to derive closed-form solutions for the macroscale behaviour of composite materials, assumptions and simplifications are required about inclusion shapes, the interaction between the matrix and inclusions and the interaction between adjacent inclusions. The nature of these assumptions has resulted in a range of homogenisation schemes, of which some popular ones are the Dilute Scheme (DS), the Mori-Tanaka (MT), the Self-Consistent Scheme (SCS) and the Generalised Self-Consistent Scheme (GSCS) (Mori and Tanaka, 1973; Hill, 1965; Zaoui, 2002; Benveniste, 2008). Nevertheless, shale, a natural geo-composite, is inherently more complex than the assumed schematic composites or even synthetic ones. Therefore, it is of great importance to clarify the applicability of these formulations to accurately homogenise the mechanical response of complex microstructures of shale rocks.

Homogenisation methods have thus been used in conjunction with various assumptions to characterise the mechanical behaviour of both shales and the clay particles. For instance, in their pioneering work on the micro-mechanical modelling of the anisotropic elastic response of shales, Hornby *et al.* (1994) assumed an isotropic intrinsic response for the clay particles into which macroscopic anisotropy was introduced through platelet-shape for the particles, their orientation and interparticle nanopores. Silt inclusions were then added as spherical isolated grains. Subsequent work modified this approach to provide an improved description of the elastic response of shales, including the incorporation of organic matter into the shale microstructure model (Sayers, 1994; Jakodsen *et al.*, 2003; Ortega *et al.*, 2007; Zhu *et al.*, 2012; Vasin *et al.*, 2013; Sayers, 2013a; Qin *et al.*, 2014). The main difference between these studies relates to the homogenisation strategies used to upscale the shale matrix (containing solid clay, kerogen and fluid phases), as well as the properties of the solid clay and kerogen. For example, Zhu *et al.* (2012) and Qin *et al.* (2014) considered kerogen as elliptical inclusions embedded into the shale microstructure. Guo *et al.* (2014) followed the same approach as Hornby *et al.* (1994), combining clay particles with kerogen and adding pores as spherical, isolated inclusions. In contrast, Vernik and Landis (1996) considered kerogen as an isotropic background matrix for the shale, which causes a reduction of the elastic constants. However, Sayers (2013b) showed that a model in which the matrix is described as a transversely isotropic (TI) kerogen and the shale as inclusion provides a better prediction of the elastic stiffness.

Clearly, several quite different modelling approaches have been proposed to explain experimental observations, further highlighting the complexity of shales. In some studies (e.g. Wu *et al.*, 2012; Zhu *et al.*, 2013), multiple micro-structural features, such as the amount of pores and their aspect ratios in both clay and kerogen, kerogen particle aspect ratio, cracks, etc., were considered numerically. However, these features could not be directly measured and need to be calibrated. Although it is computationally possible to add any level of detail to a model, it should be noted that different combinations of these microstructural features can produce the same overall mechanical response. Consequently, it is still difficult to be sure of the microstructural factors which contribute most to the overall anisotropic mechanical response of shales (Bayuk, 2008). Moreover, the presence of too many unknowns in the model does not allow to assess the accuracy of the adopted homogenisation formulations.

Direct numerical simulations based on microstructural information have been used, not only to provide insights into the overall macroscopic behaviour of multiphase media, but also to quantify the applicability and limitations of the different homogenisation techniques (Zheng and Du, 2001; Segurado and Liorca, 2002; Schmauder *et al.*, 2003; Hbaieb *et al.*, 2007; Klusemann and Svendsen, 2010; Stransky *et al.*, 2011; Mortazavi *et al.*, 2013; Moussaddy *et al.*, 2013). Studies to date have considered synthetic composite materials with a matrix containing less than 20% of spherical or cylindrical inclusions; void spaces in the matrix have been assumed to be spherical, isolated pores. Results demonstrate that the accuracy of the homogenisation techniques is sensitive to the volume fraction and the shape of inclusions, along with the stiffness contrast between the inclusions and the matrix.

Two key issues need to be resolved in order to successfully implement multi-scale modelling approaches. Firstly, the mechanical properties of the elementary building blocks of shales must be known. Whilst the mechanical properties of phases, such as calcite and quartz, are reasonably well constrained, those of the solid unit of the porous clay and of organic matter are less well known. The second issue is the selection of an appropriate homogenisation strategy with which to account for the shale micro-structure and capture its behaviour at a macroscopic scale. With these two issues in mind, the objective of the present study is to assess the capabilities of multi-scale homogenisation methods to predict the elastic mechanical response of organic-rich shales using both numerical modelling and experimental measurements, from nano to macro scales. Here, shale is assumed to be a composite formed by a porous matrix in which silt mineral grains/inclusions are randomly distributed (Figure 4.1). We undertake numerical investigations designed to develop a better understanding of the capabilities and limitations of the homogenisation methods as a way of predicting the macroscopic behaviour of shales. Several numerically-generated microstructures based on SEM images and stochastic models were simulated. The macroscopic elastic response of these models were compared with the values predicted by the homogenisation methods, accounting for their microstructures. Published mechanical measurements using Ultra-sonic Pulse Velocity (UPV) test on core samples, are then used to evaluate the predictions of the homogenisation method. Finally, indentation moduli measured parallel and perpendicular to bedding in several characterised organic-rich shale samples, are used to further test the multi-scale homogenisation formulation for predicting the shale elastic response.

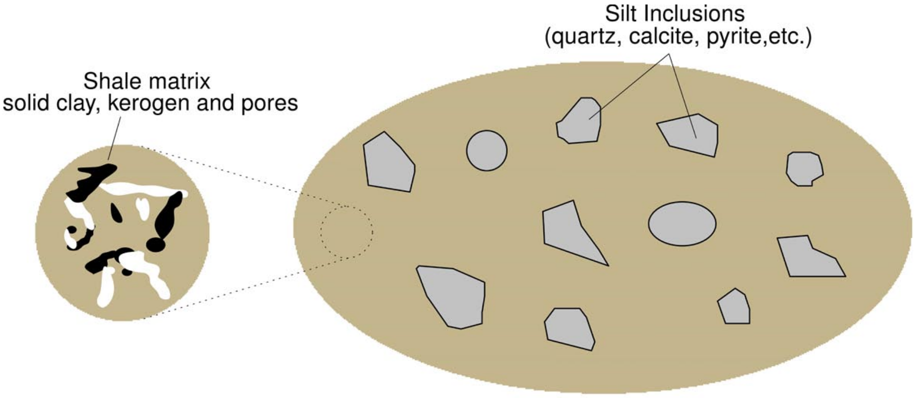

Figure 4.1: Schematic microstructure of shales.

4.2 Mean-field homogenisation methods

In order to characterise the macroscopic response of a multi-phase composite, a representative element volume (REV) is required. This volume (Ω) is defined in such a way that the macroscopic response for any sample larger than the REV, will be independent of the sample size. Assuming a linear elastic response for all the composite constituents, the elastic relationship at both micro and macro scales can be described as:

$$\boldsymbol{\sigma}(\boldsymbol{x}) = \mathbb{C}(\boldsymbol{x}) : \boldsymbol{\varepsilon}(\boldsymbol{x}) \tag{4.1}$$

$$\boldsymbol{\Sigma} = \mathbb{C}_{\text{hom}} : \boldsymbol{E} \tag{4.2}$$

where $\boldsymbol{x}$ is the position vector inside the REV, $\boldsymbol{\sigma}(\boldsymbol{x})$ is the local stress field, $\boldsymbol{\varepsilon}(\boldsymbol{x})$ is the local strain field, $\boldsymbol{\Sigma}$ is the macroscopic stress tensor and $\boldsymbol{E}$ is the macroscopic strain tensor. $\mathbb{C}(\boldsymbol{x})$ and $\mathbb{C}_{\text{hom}}$ represent the local and global fourth-order stiffness tensors, respectively.

If the average of a field, α, over the representative element volume is defined as:

$$\langle \alpha \rangle = \frac{1}{\Omega} \int_{\Omega} \alpha(\boldsymbol{x}) d\boldsymbol{x} \tag{4.3}$$

the macroscopic stress and strain can then be written in the following form:

$$\boldsymbol{\Sigma} = \langle \boldsymbol{\sigma} \rangle \quad ; \quad \boldsymbol{E} = \langle \boldsymbol{\varepsilon} \rangle \tag{4.4}$$

In order to relate the macroscopic strain to the local strain field, a linear relationship can be established as:

$$\boldsymbol{\varepsilon}(\boldsymbol{x}) = \mathbb{A}(\boldsymbol{x}) : \boldsymbol{E} \tag{4.5}$$

where $\mathbb{A}$ is the localisation tensor, which depends on both the homogenisation scheme and the assumptions made on the mechanical response. Considering a composite with N different phases and combining Eq. 4.5 into Eq. 4.4, it can be shown that:

$$\langle \mathbb{A} \rangle = \sum_{r=0}^{N} f_r \langle \mathbb{A}_r \rangle = \mathbb{I} \tag{4.6}$$

where f_r and $\mathbb{A}_r$ represent the volume fraction and localisation tensor for phase r, respectively. Consequently, the relationship between the macroscopic stress and strain can be determined.

$$\boldsymbol{\sigma}(\boldsymbol{x}) = \mathbb{C}(\boldsymbol{x}) : \mathbb{A}(\boldsymbol{x}) : \boldsymbol{E} \tag{4.7}$$

$$\Sigma = \langle \boldsymbol{\sigma} \rangle = \langle \mathbb{C} : \mathbb{A} \rangle : \boldsymbol{E} \tag{4.8}$$

$$\mathbb{C}_{\text{hom}} = \langle \mathbb{C} : \mathbb{A} \rangle = \sum_{r=0}^{N} f_r \mathbb{C}_r : \mathbb{A}_r \tag{4.9}$$

where $\mathbb{C}_r$ is the stiffness tensor for phase r. If the continuous phase representing the composite matrix, which surrounds the remaining constituents (see Figure 4.1), is assigned as phase 0, Eq. 4.9 can be re-written as:

$$\mathbb{C}_{\text{hom}} = \mathbb{C}_0 + \sum_{r=1}^{N} f_r (\mathbb{C}_r - \mathbb{C}_0) : \mathbb{A}_r \tag{4.10}$$

The analytical expression for both the localisation tensor and the effective homogenised stiffness tensor will be summarised for each of the four homogenisation schemes adopted in this study; namely the Dilute Scheme, the Mori-Tanaka model (MT), the Self-Consistent Scheme (SCS), and the Generalized Self-Consistent Scheme (GSCS). For more information on the derivations and assumptions of these schemes, readers are referred to Zaoui (2002), Chateau and Dormieux (2002), Benveniste (2008) and Abou-Chakra Guery *et al.* (2010).

4.2.1 Dilute Scheme

In the Dilute Scheme, the primary assumption is that the concentration of inclusions in the matrix is small, so that there is no interaction between them and their separation is well-defined.

This leads to a solution for composites with low concentrations of inclusions based on a single inclusion embedded in an infinite matrix. In this case, the localisation tensor for phase r can be defined as follows:

$$\mathbb{A}_r = \left[\mathbb{I} + \mathbb{P}^0_{\mathrm{I_r}} : (\mathbb{C}_r - \mathbb{C}_0)\right]^{-1} \tag{4.11}$$

where $\mathbb{P}^0_{\mathrm{I_r}}$ is the Hill's tensor, which is related to the Eshelby tensor and is in general a function of the shape and orientation of the rth inclusion as well as the stiffness tensor of the matrix phase (see Appendix A.1). The corresponding homogenised stiffness tensor can be derived as:

$$\mathbb{C}_{\mathrm{hom}} = \mathbb{C}_0 + \sum_{r=1}^{N} f_r \left[(\mathbb{C}_r - \mathbb{C}_0)^{-1} + \mathbb{P}^0_{\mathrm{I_r}}\right]^{-1} \tag{4.12}$$

4.2.2 Mori-Tanaka Scheme

The Mori-Tanaka model was developed in a similar way as the Dilute Scheme, by including an extra term in order to account for the interaction between inclusions. In this case, the localisation tensor, $\mathbb{A}_r$, was given as:

$$\mathbb{A}_r = [\mathbb{I} + \mathbb{P}^0_{\mathrm{I_r}} : (\mathbb{C}_r - \mathbb{C}_0)]^{-1} : \left[\sum_{s=0}^{N} f_s [\mathbb{I} + \mathbb{P}^0_{\mathrm{I_r}} : (\mathbb{C}_s - \mathbb{C}_0)]^{-1}\right]^{-1} \tag{4.13}$$

and the corresponding homogenised effective stiffness tensor can be obtained as:

$$\mathbb{C}_{\mathrm{hom}} = \mathbb{C}_0 + \sum_{r=1}^{N} f_r [(\mathbb{C}_r - \mathbb{C}_0)^{-1} + \mathbb{P}^0_{\mathrm{I_r}}]^{-1} \left[\sum_{s=0}^{N} f_s [\mathbb{I} + \mathbb{P}^0_{\mathrm{l_r}} : (\mathbb{C}_s - \mathbb{C}_0)]^{-1}\right]^{-1} \tag{4.14}$$

4.2.3 Self-Consistent Scheme

In the Self-Consistent Scheme each inclusion is assumed to be embedded in an unknown homogenised medium, so that the localisation tensor $\mathbb{A}_r$ will contain the homogenised effective stiffness tensor, $\mathbb{C}_{\mathrm{hom}}$. Within this formulation, no single phase is considered to act as the matrix and all the phases are given equal importance. Due to the implicit form of this scheme, an iterative algorithm is required allowing the homogenised stiffness tensor to be obtained in a straightforward way. The homogenised localisation tensor, $\mathbb{A}^{\mathrm{hom}}_r$, for the Self-Consistent Scheme is thus given as:

$$\mathbb{A}^{\mathrm{hom}}_r = [\mathbb{I} + \mathbb{P}^{\mathrm{hom}}_{\mathrm{l_r}} : (\mathbb{C}_r - \mathbb{C}_{\mathrm{hom}})]^{-1} : \left[\sum_{s=0}^{N} f_s [\mathbb{I} + \mathbb{P}^{\mathrm{hom}}_{\mathrm{l_r}} : (\mathbb{C}_s - \mathbb{C}_{\mathrm{hom}})]^{-1}\right]^{-1} \tag{4.15}$$

and the homogenised effective elasticity tensor, for composites with inclusions having identical orientation and shape, is derived as:

$$\mathbb{C}_{\mathrm{hom}} = \sum_{r=0}^{N} f_r \mathbb{C}_r : [\mathbb{I} + \mathbb{P}^{\mathrm{hom}}_{\mathrm{I_r}} : (\mathbb{C}_r - \mathbb{C}_{\mathrm{hom}})]^{-1} \tag{4.16}$$

4.2.4 Generalized Self-Consistent Scheme

This scheme was developed on a similar basis as the SCS, with the difference that the inclusion is assumed to be surrounded by some of the matrix material and subsequently embedded in the homogenised medium. The determination of the closed-form solution for this scheme is not as straightforward as in the other models, but several solutions have been proposed based on different assumptions (Christensen and Lo, 1979; Benveniste, 2008). In the case of an isotropic composite material including one type of spherical inclusion, the bulk and shear moduli were obtained as:

$$\kappa_c = \frac{f_0 \kappa_0 (4\mu_0 + 3\kappa_i) + f_i \kappa_i (4\mu_0 + 3\kappa_0)}{f_0 (4\mu_0 + 3\kappa_i) + f_i (4\mu_0 + 3\kappa_0)} \tag{4.17}$$

where the subscripts 0, i, and c represent the matrix, inclusion and the homogenised composite, respectively. It should be noted that both GSCS and MT provide the same value for the homogenised bulk modulus. The effective shear modulus, μ_c, of the composite material can be obtained by solving the following equation:

$$A\left(\frac{\mu_c}{\mu_0}\right)^2 + B\left(\frac{\mu_c}{\mu_0}\right)^2 + C = 0 \tag{4.18}$$

where A, B and C are material constants which are provided in Appendix A.2.

4.3 Material Point Method

The effect of interactions between different phases on the mechanical behaviour of a composite can be assessed by numerical modelling, with the benefit of simulating the detailed geometry of the REV. In this study, material point method (MPM) was selected for this purpose. This method was originated in fluid dynamics and further developed by Sulsky *et al.* (1994) and extended by Sulsky and Schreyer (1996) and Bardenhagen and Kober (2004) among others to model solid mechanics problems. Technically, the MPM is a meshless method in which the material points that also possess the state variables (position, mass, velocity, acceleration, stress state, etc), are Lagrangian and represent the discretised continuum. They are independent of the Eulerian fixed computational mesh. Since the method uses an arbitrary mesh, distortion inherent from the usual Lagrangian formulations is avoided. Conservation of mass is automatically satisfied as the mass of each point is kept constant during the calculation. At each time step, the information is initially extrapolated from the material points to the mesh, where the governing equations are solved and the solutions are transferred back to the mesh and updated (Wieckowski, 2004; Jassim, 2012). This numerical method will be further discussed in the next chapter and the basic formulation can also be found in Appendix B.

4.4 Matrix-inclusion morphology

Scanning Electron Microscope (SEM) images of shale samples can provide important insights into their microstructure. Figure 4.2 shows an SEM image on a shale cut perpendicular to the bedding plane. It can be seen that, at the scale of a few micrometres, shales can be described as composite materials in which the inclusions are surrounded by the matrix phase. These inclusions are characterised by various shapes ranging from spherical to angular and including highly irregular shapes for which the orientation is not clearly defined.

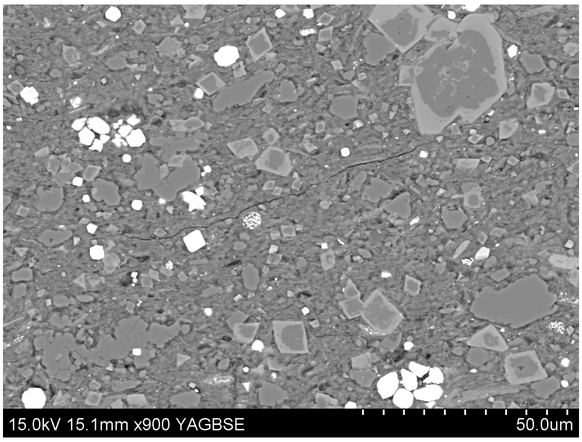

Figure 4.2: Typical SEM image of a shale sample from a cutting section perpendicular to bedding plane.

Here, the MPM is used to simulate the mechanical behaviour of shale with different microstructures. The numerical results are then compared with the homogenisation schemes described in the previous section, in order to evaluate the modelling capabilities of the mean-field methods in predicting the homogenised behaviour of highly complex natural composites such as shales. We extend previous studies by considering angular inclusion shapes, highly-contrasting matrix and inclusion properties, high concentrations of inclusions, three phase composites with complex random micro-structures. A summary of typical values of elastic properties of common mineral inclusions in shale rocks are given in Table 4.1. Additionally, the following material properties are assigned to the isotropic porous clay matrix: Young's modulus E=3 GPa; Poisson's ratio v=0.3 (Abou-Chakra Guery *et al.*, 2010).

Table 4.1: Properties of common silt inclusions in shales (Bass, 1995; Mavko *et al.*, 2009; Whitaker *et al.*, 2010).

Minerals	Elastic properties	
	E (GPa)	Poisson's ratio
Quartz	101	0.06
Calcite	95	0.28
Pyrite	265.4	0.18
Feldspar	73.7	0.26
Dolomite	118	0.29

4.4.1 Composite with single inclusion

The analytical solutions for the mean-field homogenisation methods were developed on the basis of a single inclusion with a spherical or elliptical shape, embedded in the matrix phase (Zheng and Du, 2001). Such assumptions do not recognize the natural shape of inclusions in clayey rocks that are mostly small and angular pieces of hard minerals, such as calcite and quartz. In order to evaluate such analytical solutions and account for the angularity of real inclusions, it is proposed to explore the simulations of a single inclusion with a spherical or cubic shape. Due to the symmetry of the problem under consideration, only one quarter of the REV model with appropriate boundary conditions is simulated (Figure 4.3). Two different loading conditions are performed by controlling the displacements. In the first loading, a uniform normal displacement has been applied at the top and two perpendicular lateral boundaries of the REV model, with normal movements not permitted at the remaining boundaries. This loading condition is expected to generate hydro-static compression and can be used to estimate the bulk modulus of the REV. In the second loading, a uniaxial compression is simulated by imposing the vertical displacement at the top boundary of the REV and fixing the vertical movement at the opposite boundary. This test was undertaken to estimate the Young's modulus of the REV.

In addition, an arrangement of eight material points per element, with 8000 points in total number, was determined through a mesh sensitivity analysis, which was carried out to minimise the discretisation error and improve the accuracy of the results. This mesh, together with the described loading and boundary conditions, has been adopted in all simulations unless otherwise mentioned.

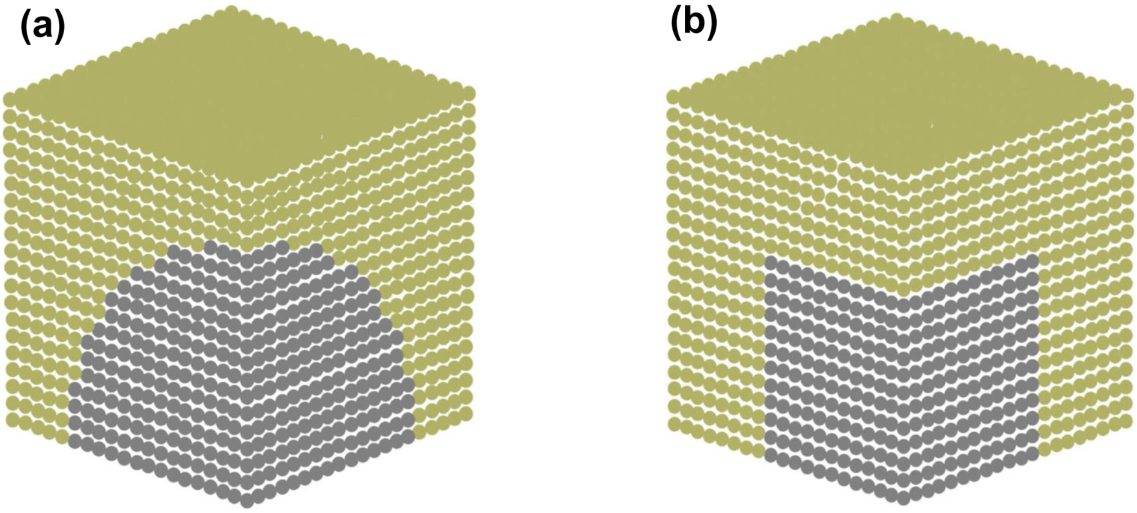

Figure 4.3: MPM models: (a) spherical and (b) cubic inclusions embedded in a matrix.

Figure 4.4 shows a comparison of the normalised bulk modulus for single spherical and cubic inclusions and the values predicted by the different homogenisation methods, for different volume fractions of the inclusion. The comparison between the simulated and calculated bulk modulus using the MT and GSCS models, are in good agreement. However, for the SCS, it can be seen that a stiffer behaviour is predicted for a volume fraction of the inclusion greater than approximately 20%, which results in an overestimation of the bulk modulus. The analyses also indicate that there is no influence of the cubic-shaped inclusion on the homogenised bulk modulus of the REV.

Comparison of the simulated and calculated normalised Young's modulus is also shown in Figure 4.4. Overall, the numerical results are in good agreement with the SCS, up to volume fractions of inclusion around 40%. For inclusion concentrations above this threshold, the SCS overestimates the Young's modulus. Both MT and GSCS predictions slightly underestimate the Young's modulus and the prediction error increases with increasing inclusion volume fraction. It should be noted that the MT and GSCS models predict virtually identical moduli. However, due to the simplicity of the implementation of MT compared to the GSCS scheme, this scheme allows a variety of shale rocks to be investigated, for example with a transversely isotropic matrix, a multi-phase composite and with different inclusion shapes. In addition, as the inclusion volume fraction increases above 20%, there is an underestimation of the effective properties using the DS model, leading to a softer response. This is due to the concentration of inclusions and their interaction, which are not accounted for in the formulation of DS.

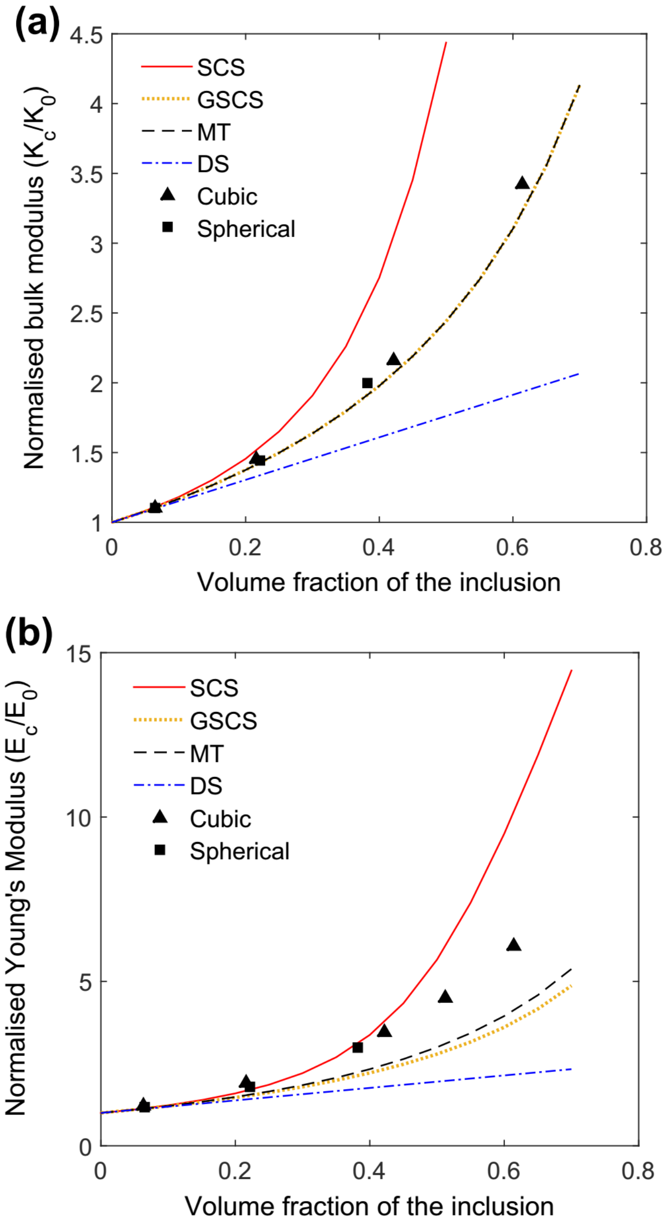

Figure 4.4: Comparison between the results of numerical and mean-field homogenisation methods for models with various volume fractions of spherical and cubic inclusions: (a) normalised bulk modulus and (b) normalised Young's modulus.

4.4.2 Composite with Randomly Distributed Inclusions

Shales are very complex multi-phase composite materials, which usually contain various types of inclusions such as calcite, quartz, pyrite, feldspar, kerogen, etc. Calcite and quartz constitute the highest volume fractions of inclusions, with other minerals usually less than 15% (Meier *et al.*, 2013; Ortega *et al.*, 2007; Sierra *et al.*, 2010). In addition, there is a significant strength difference between the major inclusions (calcite/quartz) and the low volume fraction inclusions. For example, pyrite is almost three times stiffer than calcite (see Table 4.1).

For the final investigation of the predicted results by homogenisation techniques, they are evaluated for the case of a composite with randomly distributed grains, which is more close to the real microstructure of shales. To increase the level of complexity, two types of cubic inclusions with different sizes including calcite and pyrite are considered. The ratio of inclusions' volumes to the total volume of REV are 0.33 and 0.1 for calcite and pyrite grains, respectively. The model consists of 27000 material points with eight points per element (Figure 4.5). The inclusions are randomly placed in the matrix in such a way that they are not in contact with each other, and all of them are surrounded by at least one layer of material points having the clay matrix properties.

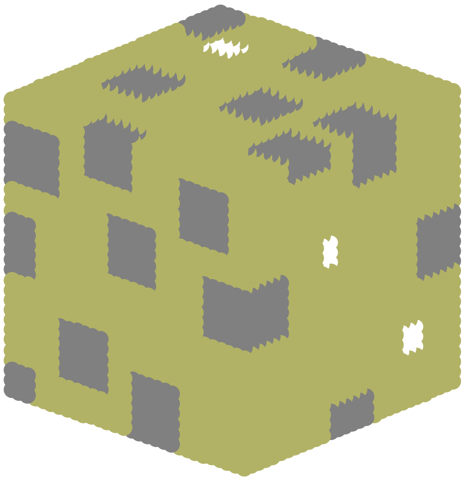

Figure 4.5: A REV with randomly distributed calcite (black) and pyrite (white) grains; volume fractions are 33% and 1%, respectively.

Three random models were generated and both hydrostatic and uniaxial compression tests were carried out. The bulk modulus, Young's modulus and two components of the stiffness tensor obtained from numerical simulation and two homogenisation schemes are presented in Table 4.2. MT provides a very good prediction for bulk modulus and a fair prediction for Young's modulus. In addition, although the error of prediction for Young's modulus using SCS is a little less than MT at this volume fraction of inclusions, the bulk modulus is overestimated. In fact, the results are in agreement with the trend being observed for the case of a single inclusion. Considering the results obtained for stiffness tensor components, no clear advantage can be observed by using MT or SCS to predict the overall, homogenised stiffness tensor. This is because for an isotropic material, each component of its stiffness tensor is a function of two elastic constants which combine the errors obtained for bulk and Young's moduli.

Table 4.2: Numerical and mean-field methods results for the random three-phase composite.

Normalized Modulus		K_c/K_0	E_c/E_0	C^c_{11}/C^0_{11}	C^c_{12}/C^0_{12}
Method	Simulation	1.86	2.34	2.83	2.16
	MT	1.77	1.97	2.142	1.91
	SCS	2.38	2.66	2.91	2.57

Theoretically, the mean-field methods were formulated for N different phases, which make it possible to study composites with various inclusions. On the other hand, from a practical point of view, it can be difficult to accurately determine the volume fraction of each inclusion, especially when its concentration is very low or has a similar density as the other inclusions. Mineralogical information may be supplied simply as the volume fraction of clay and non-clay minerals. It is therefore of interest to quantify the effect of ignoring minerals present in low concentration and simplifying the shale to a two-phase composite, based on its homogenised response.

Here, a simple example which consists of a small pyrite inclusion placed within calcite grains has been adopted, to study the difference in the homogenised response between a real composite and a simplified one. The volume fraction of pyrite is selected based on common values found in shale samples for minor inclusions. For example, the Kimmeridge shale consists of 30.5% quartz, 2.1% pyrite, 7.2% feldspar, with the rest comprising different clay minerals (Horby, 1998). A model with 26.8% calcite and 11.3% pyrite is generated. The results of the normalized elastic moduli for the three-phase composite and the simplified one, in which all the clay minerals, are assumed to be quartz are presented in Table 4.3, indicating that the lack of information about these low concentrated minerals may not affect the results significantly. It can also be observed that the SCS is more sensitive to this simplification than MT method. Generally, it can be summarized that this practical simplification appears to be acceptable.

Table 4.3: The results of numerical and mean-field methods for both three-phase and simplified composite.

Model		Three-Phase Comp.		Simplified Comp.	
Normalized Modulus		K_c/K_0	E_c/E_0	K_c/K_0	E_c/E_0
Method	Simulation	1.99	2.33	1.98	2.32
	MT	1.94	2.17	1.92	2.15
	SCS	2.68	3.31	2.60	3.16

4.5 Porous clay matrix

One of the complexities of shale rocks is that the matrix itself is a porous material, for which the mechanical properties of its solid unit (clay minerals) are poorly constrained. Nevertheless, the mechanical properties of the solid clay, in conjunction with the total porosity of the clay matrix, play a major role in the overall macroscopic mechanical response of clayey rocks. Due to the difference in length-scale between voids and the porous clay matrix , the homogenisation schemes can be adapted to account for the effects of porosity on the mechanical response of the matrix and to back-analyse the solid clay properties. In this section, the accuracy and capabilities of the homogenisation methods for predicting the mechanical response of porous composites are investigated. According to the experimental data available in the literature, the porosity of clay matrix in shales varies between 2 to 40% (Ortega *et al.*, 2007; Sierra *et al.*, 2010; Meier *et al.*, 2013). Moreover, determination of the elastic properties of a solid unit of clay is still an open topic, which is out of the scope of this research, with different values obtained by different researchers. Here, values of 5 GPa for Young's modulus (E) and 0.33 for Poisson's ratio (v) were adopted for the solid unit of clay (Shen *et al.*, 2012).

4.5.1 Simplified porous matrix micro-structure

As the real microstructure of the porous clay matrix is difficult to characterise accurately, two different idealized models are considered for the arrangement of voids and clay particles. In the first model, it is assumed that the voids are embedded in solid clay, similar to the matrix-inclusion placement; in the second model, the solid unit of clay is considered to be spherical particles in contact with each other and forming a network of connected pores (Figure 4.6). Both models are subject to hydrostatic loading with different porosities.

The results of the normalized bulk moduli are plotted in Figure 4.7 along with the predicted moduli by the mean-field homogenisation schemes. The MT method is able to predict the effective bulk modulus for a porosity ranging between 0 and 1. In contrast, the SCS prediction of the same effective modulus is only valid up to porosity values around 0.5, after which the stiffness reaches non-physical values. The same observation can be made for the DS model, for which non-physical values are predicted for porosities above 0.33. In addition, from Figure 4.7 it can be concluded that the stiffness response of the first model with isolated voids is in good agreement with the MT results. In contrast, the second model, with a pore network, shows a good agreement with the SCS predictions.

Published results of indentation tests and imaging techniques along with theoretical con-

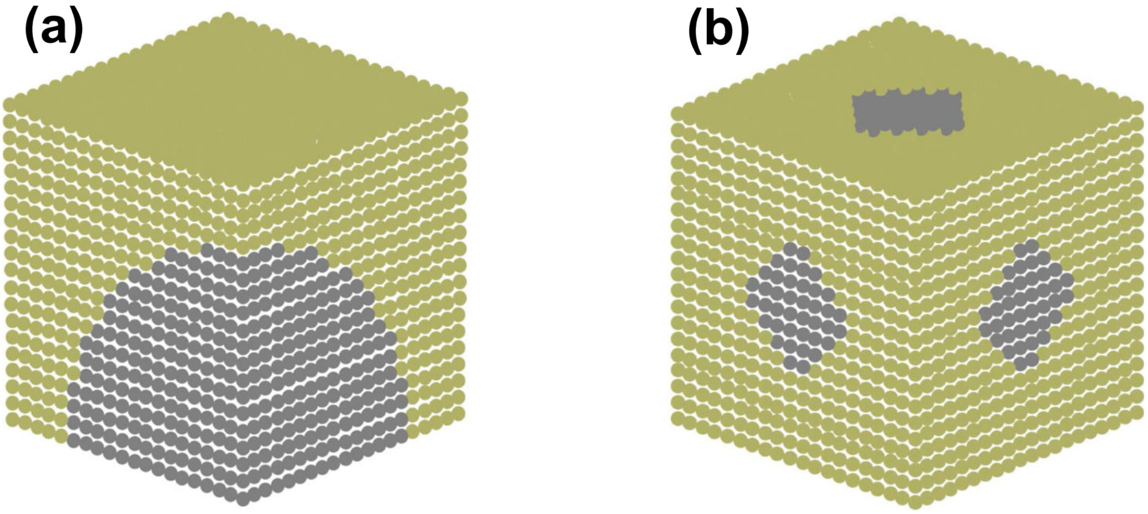

Figure 4.6: MPM models: (a) isolated void and (b) connected pore network. The grey particles are deleted to generate voids.

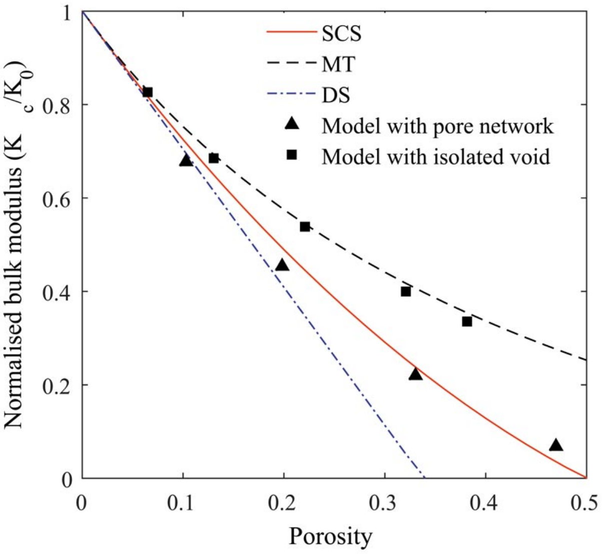

Figure 4.7: Comparison between the results of numerical and homogenisation methods for normalised bulk modulus of a clay matrix with isolated and connected pores.

cepts in granular media are next used to elucidate which of the two modelled arrangements might be more realistic to represent the clay matrix microstructure. In work undertaken by Ulm and Abousleiman (2006) on different shale samples, nanoindentation tests highlighted the linear relationship between the indentation modulus of clay matrix and porosity, with the indentation moduli reaching the value of zero when the porosity approached a value of approximately 0.5 (Figure 4.8). Additionally, in the model with spherical clay particles and a pore network (see Figure 4.6), if the radius of particles is decreased until the porosity reaches a value of approximately 0.52, then the contact between the particles is completely lost. This value is almost equal to the one observed by Onoda and Liniger (1990) for the highest possible porosity in the case of granular packing of uniform spheroids.

The relationship between SCS-predicted, normalized bulk modulus and porosity is almost linear and predicts that the stiffness becomes zero when the porosity is 0.5 (Figure 4.7). It therefore appears that the SCS is an appropriate model with which to homogenise a porous clay matrix, as its results are well matched with both theoretical results and experimental observations.

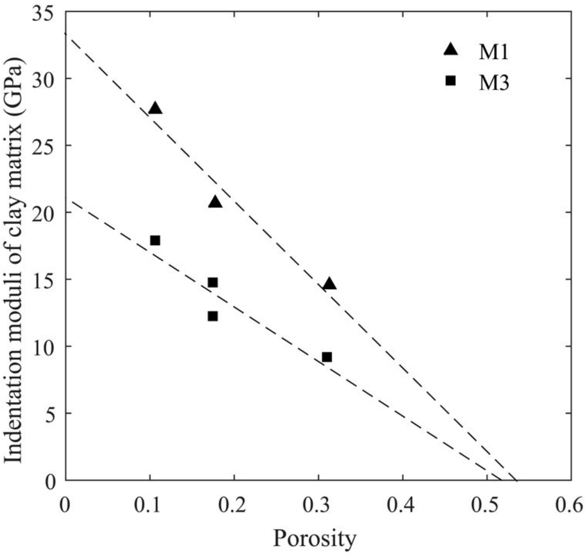

Figure 4.8: Indentation moduli parallel (M_3) and perpendicular (M_1) to bedding plane of shale samples versus the porosity (Modified from Ulm and Abousleiman, 2006).

4.5.2 Porous Matrix with Random Pores

Having evaluated the performance of the homogenisation methods with simplified pore systems, a realistic 3D stochastic pore network model, obtained from high resolution SEM images of a shale rock (Ma *et al.*, 2014), has also been simulated. The stochastic model consists of a cube with 200 voxels in each dimension, with a property of either a pore or solid assigned to each voxel. Three smaller cubes with 25 voxels in each dimension, with different porosities were selected from inside the stochastic model (Figure 4.9). The three stochastic samples used in the simulations, are generated by mapping each voxel into one element.

Figure 4.10 shows the averaged normalized Young's moduli in three directions obtained from numerical simulations. A good agreement can be observed between numerical results and values predicted by the SCS model.

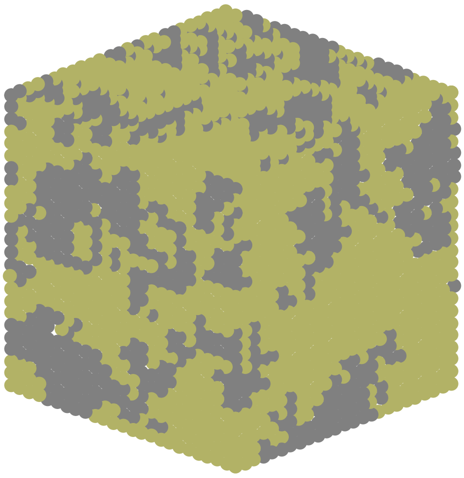

Figure 4.9: Stochastic model of porous clay matrix with porosity of 0.32 (pores are represented by grey particles).

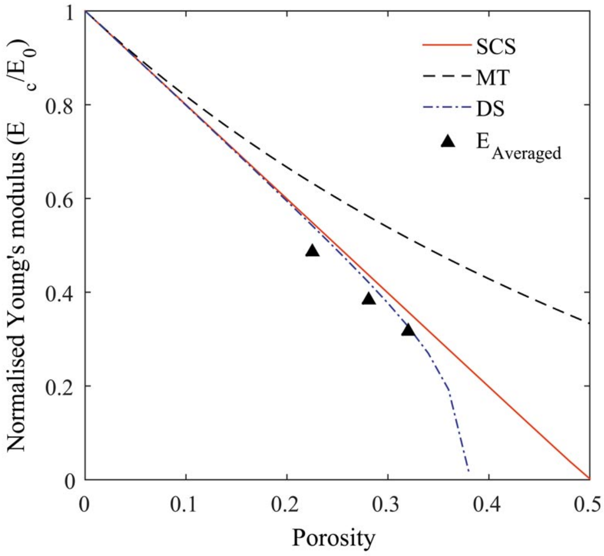

Figure 4.10: Comparison between the results of numerical and mean-field homogenisation methods of normalized averaged Young's modulus in three directions for the stochastic models.

It is also well-known that the shale pore system is complex, consisting of both connected and isolated pores ranging in size from a nanometre to a few micrometres (Chalmers *et al.*, 2012; Chen *et al.*, 2015; Naraghia *et al.*, 2015). Consequently, the stochastic models seem to represent the experimental observations on both the microstructure and mechanical response of porous clay. To further study the mechanical response of these random pore systems, a REV was considered in which the porosity was randomly distributed through the model. As there was no restriction on the placement of the pores, a matrix with both isolated and connected pores was formed (Figure 4.11). Three different target porosities below and above the threshold of 50% porosity were considered and six random models were generated for each target porosity.

Figure 4.12 shows the numerical predictions of the effective bulk and Young's moduli along with the results obtained from the adopted homogenisation schemes. It can be seen that for the case of a composite with random porosity below 50%, the SCS provides good predictions compared to the other schemes. It is also observed that when the porosity exceeds the threshold of 50%, the stiffness converges towards a value of zero. Additionally, the three different random models for each target porosity produce approximately the same mechanical behaviour which makes these results reproducible with no noticeable anisotropy induced by the pore network.

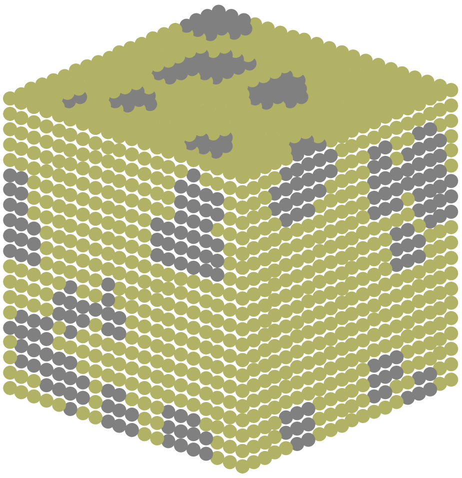

Figure 4.11: REV for a matrix with porosity of 0.3 and a random distribution of pores (pores are represented by grey particles).

Since the microstructure of a porous clay matrix is difficult to characterise, conceptual models of porous clay matrix offer an efficient quantification of its mechanical response. This allows the overall elastic-plastic behaviour of the clayey rocks to be investigated. When pore spaces embedded in solid clay are assumed to be spherical and isolated, closed-form solutions for the homogenised elastic-plastic response can be derived (Maghous *et al.*, 2009; Shen *et al.*, 2012, 2013). However, the choice of simplified, isolated voids in this study, resulted in a poor prediction of the mechanical response of porous clay.

Using models which assume random pores in a porous clay matrix, the mechanical response is more consistent with the theoretical and experimental results. In addition, the generation of different random pores system to capture a given target porosity would not alter the overall mechanical response. The approach followed here may produce more accurate results when a

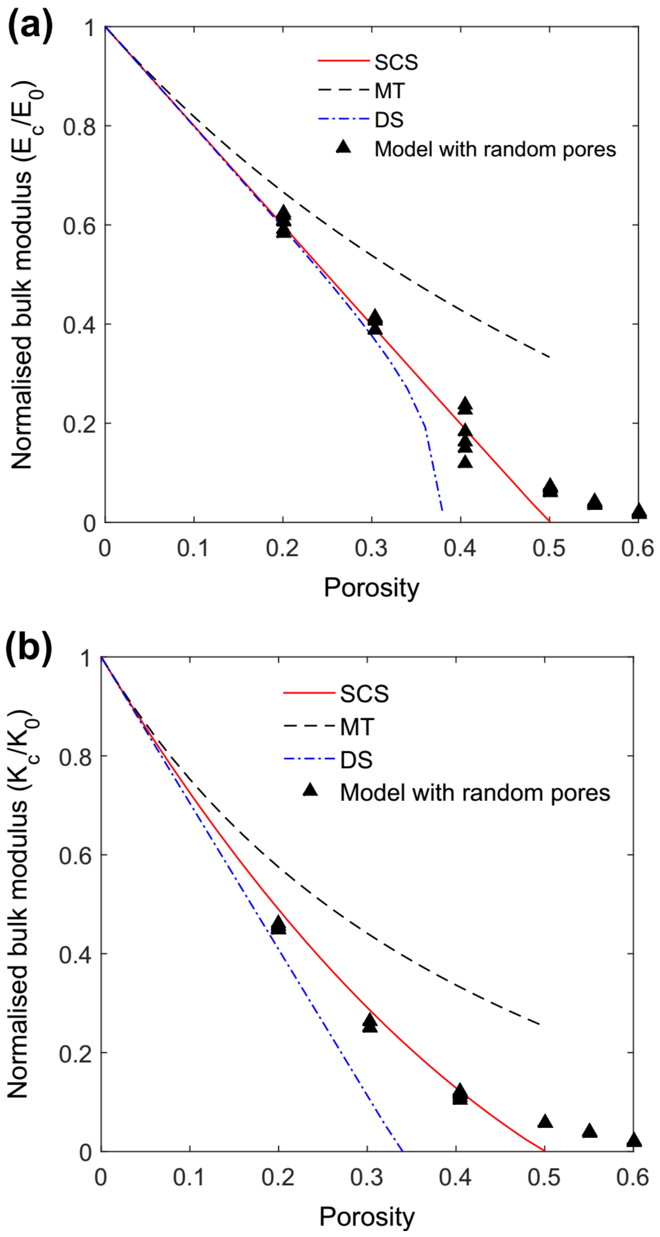

Figure 4.12: Comparison between numerical and mean-field methods for the model with random porosity: (a) normalised Young's modulus and (b) normalised bulk modulus.

transversely isotropic elastic response, along with a suitable failure surface such as Drucker-Prager are considered for the solid unit of clay.

4.6 Homogenisation of shale rock elastic response

In the previous section, the capabilities of using homogenisation techniques in the case of shale rocks was investigated using numerical simulations in which several simplified virtual shale microstructures were generated and studied. Good agreement was obtained between macroscopic elastic responses of the numerical rocks and the predicted values from the homogenisation methods.

However, it is clear that real composites, especially shales, are far more complex than the assumed numerical models and consequently, it is important to validate the homogenisation techniques against several experimental data sets. Shale rocks, in general, are transversely isotropic (TI) in elastic response and it is well known that this property originates from aligned, plate-like clay minerals within the shale (Sayers, 1994). However, different models have been proposed to explain this TI response. For example, Hornby *et al.* (1994) assumed that the shale matrix consists of elliptical pores and elliptical isotropic elastic clay particles, and these elementary building blocks are the source of anisotropy. This idea has been adopted in some of the subsequent studies (Jakobsen *et al.*, 2003; Zhu *et al.*, 2012; Vasin *et al.*, 2013). Ortega *et al.* (2007), on the other hand, implicitly considered the effect of the plate-like elements by a TI set of elastic constants for the solid unit of the matrix based on the nanoindentation results, obtained on clay matrix (see Figure 4.8).

In this section, homogenisation formulations are used to explain experimental measurements of the elastic properties of shale samples. Shales with different inclusion volume fractions were selected to show how understanding of the performance of each mean-field homogenisation formulation could help to better interpret the predictive results. Whilst UPV tests have been used to fully characterise the elastic response of shale samples, the experiment requires good quality core samples and is both technically difficult and time-consuming. Recently, indentation tests have been used to estimate the mechanical properties of shales. This test can be easily and efficiently performed on shale cuttings and a good estimation on the anisotropic macroscopic elastic response of shale can be obtained (Ulm and Abousleiman, 2006; Kumar *et al.*, 2015). Here, published UPV on well-characterised shales are used to evaluate the predictive capability of the homogenisation techniques. In addition, several organic-rich shale samples were prepared, characterised and used to generate indentation data in order to extend the validation data sets.

4.6.1 Assumptions and material properties

From Eq. (4.10), it can be seen that the volume fractions and the stiffness tensors of all constituents are required to allow the calculation of the homogenised elastic response of the composite. The volume fraction and mineralogy of clay and silt inclusions can be estimated using X-ray diffraction, and the amount of organic matter can be measured by chemical analysis as it was discussed in Chapter 3. A good estimation of the porosity, which can be measured in various ways, is also essential to the calculation of the shale matrix properties. The entire porosity of the sample is assumed to exist in the shale matrix, so that the porosity of the matrix, ϕ_{matrix}, which is used in the first level of homogenisation, is calculated as:

$$\phi_{matrix} = \frac{\phi_{shale}}{1 - f_{inc}} \tag{4.19}$$

where ϕ_{shale} represents the shale porosity and f_{inc} is the total volume of non-clay minerals. For dry conditions, porosity is taken to be a constituent with zero stiffness. However, in fully saturated shale, the stiffness properties of water within pores (i.e. bulk stiffness K=2.2 GPa and shear stiffness G=0 GPa), needs to be considered (Hornby *et al.*, 1994; Vasin *et al.*, 2013).

Model implementation requires certain assumptions to be made about the properties of the different phases in shale. The shape and orientation of both inclusions and pores are generally considered to be important sources of the macroscopic anisotropic response of shales (Vasin *et al.*, 2013). Nanoindentation tests on shale sections (see Figure 4.8) suggest that the solid part of the porous clay exhibits a significant, intrinsic, anisotropic elastic response (Ulm and Abousleiman, 2006; Bobko and Ulm, 2008). Ortega *et al.* (2010) used a micro-mechanical approach to study the simultaneous effects of (a) the intrinsic anisotropy of the solid unit of porous clay, and (b) the shape and orientation of inclusions, on the transversely isotropic elastic behaviour of bulk shale. They concluded that the shape and orientation of inclusions were insignificant controls on the macroscopic anisotropy of shale, compared to the anisotropic response of the solid part of the porous clay. In addition, incorporating the effect of inclusion shape into multi-scale homogenisation requires additional experimental data which makes this approach inefficient from a practical point of view.

Here, inclusions such as quartz, calcite, pyrite, etc, are considered to be spherical and to have isotropic elastic moduli, which can be found in the literature (Table 4.1). The solid unit of porous clay, on the other hand, is assumed to be anisotropic; furthermore, its properties cannot be directly measured using conventional rock mechanics tests. Ortega *et al.* (2007) assumed that the overall anisotropy of shale originates from a solid unit of clay with universal mechanical properties. The elastic constants of the solid unit of clay, as a transversely isotropic material, were estimated by back-analysing from UPV measurements on shale core samples. In fact, this solid phase could be an agglomerate of clay particles rather than a single plate shaped clay particle. Table 4.4 provides the values obtained by Ortega *et al.* (2007). It should be noted that the assumption of isotropic elastic response for silt inclusions and high level of anisotropy for the porous clay at nanoscale, were previously confirmed using PeakForce QNM® technique in Chapter 2.

Table 4.4: Solid clay properties (data from Ortega *et al.*, 2007).

Elastic Constant	Value (GPa)
C_{11}	44.9
C_{33}	24.2
C_{13}	18.1
C_{66}	11.6
C_{44}	3.7
C_{12}=$(C_{11} - 2C_{66})$	21.7

The assumption that only one set of elastic constants can be used for the solid unit of clay (e.g. Ortega *et al.*, 2007; Table 4.4), regardless of mineralogy, is debatable and so it is of interest to compare Ortega *et al.*'s values with those used in previous studies. Hornby *et al.* (1994) back-calculated the solid clays' elastic constants from an experimental data set on clay-fluid composite as K = 22.9 GPa and G= 10.6 GPa, assuming isotropic conditions. Similar values of K = 25 GPa and G = 9 GPa are provided in Mavko *et al.* (2009). These values have been adopted in several micromechanical models of shales with satisfactory results, regardless of the clay mineralogy (Jakobsen *et al.*, 2003; Draege *et al.*, 2006; Wu *et al.*, 2012; Sayers 2013a; Qin *et al.*, 2014; Guo *et al.*, 2014). Converting the anisotropic properties in Table 4.4 using the Voigt average (Antonangeli *et al.*, 2005) to its equivalent isotropic form results in comparable values of K = 23.9 GPa and G = 6.7 GPa. Considering these micromechanical models and also nanoindentation test data (Ulm and Abousleiman, 2006), the assumption of constant properties for the elementary building block of porous clay can be adopted confidently. Additionally, it should be noted that the presented values are still much lower than the ones obtained for a single clay particle (Wang *et al.*, 2001). This difference can be justified using the conclusion being made by Bobko and Ulm (2008) in which the porous clay is considered to have a nano-granular microstructure. Based on this observation, it can be said that the mechanical response of porous clay might be mainly determined by chemical and mechanical interactions in contacts between individual clay particles or clay agglomerates, rather than the intrinsic mechanical response of a single clay particle.

Shale gas and oil reservoirs contain significant amounts of organic matter, which has a wide range of measured elastic properties. In chapter 2, a comprehensive discussion on the mechanical properties of kerogen obtained through different studies was presented. In addition, PeakForce QNM® was used to conduct direct measurements on kerogen embedded in shale matrix. Here, the values obtained by nanomechanical mapping will be adopted which were 5.9 GPa and 10.35 GPa for the Young's modulus of immature and mature kerogen, respectively if the Poisson's ration is assumed to be 0.3.

4.6.2 Elastic response of shale's porous clay

The mechanical response of silt-grade mineral inclusions in shales are well known and even possible shape effects can be quantified, using SEM or 3-D X-ray microtomographic imaging (Kanitpanyacharoen *et al.*, 2011; Vasin *et al.*, 2013; Peng *et al.*, 2015). However, neither the exact microstructure of the porous clay, nor the properties of the solid unit of this composite, have been fully evaluated. A complex network of pores including connected channels and isolated pores at different scales have been experimentally observed in shale matrix (e.g. Chalmers *et al.*, 2012). Similarly, the organic matter occurs as a semi-continuous phase, rather than as isolated inclusions in the porous clay. Consequently, the main challenge in modelling the elastic behaviour of shales is the response of the matrix.

The main assumption in our modelling strategy is that the anisotropy originates from the solid clay, having a transversely elastic response. The Self-Consistent Scheme is used to combine, without any specific orientation distribution, the solid clay with the presence of pores and organic matter. Aligned, platy clay minerals are not considered explicitly and the TI response compensates for this effect. On the other hand, Hornby *et al.* (1994) assumed an isotropic response for the solid clay and the anisotropy was subsequently generated by considering an oblate spheroid-shaped clay particles and nanopores. The SCS was combined with a differential effective medium model in order to satisfy the continuity of all the phases at any porosity level.

In order to clarify similarities and differences between the approach adopted in this paper and the pioneering work of Hornby *et al.* (1994), all five elastic constants of a fully-saturated porous clay are plotted as a function of porosity in Figure 4.13. Both approaches provide a similar trend for the elastic constants as functions of fluid-filled porosity except for C_{44}, which shows a drastic decrease with a small increase in porosity in the Hornby *et al.* (1994) formulation. Additional differences can be partly attributed to the initial assumptions with regard to the isotropy and anisotropy of the elastic properties of the solid unit of clay. It should be noted that an increase or decrease in anisotropy can, of course, be introduced by considering elliptical shapes with specific orientations for pores or organic matter in the SCS formulation. These two modelling approaches give quite consistent results in reproducing the response of porous clay.

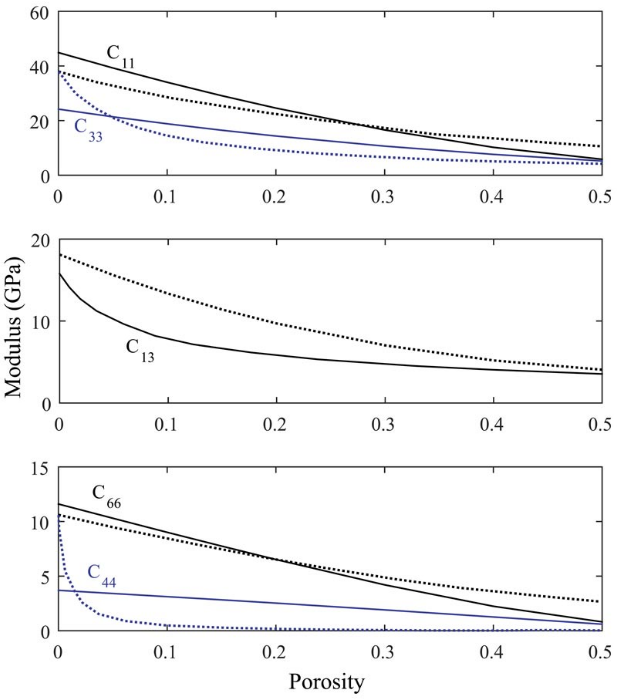

Figure 4.13: Saturated porous clay response versus porosity (solid lines are the results of this paper and dashed lines were extracted from Hornby *et al.* (1994)).

4.6.3 UPV test data sets

There are very few measurements of the mechanical behaviour of shales which are well characterised in terms of both mineralogy and microstrcture. Among these available data, those which were not used by Ortega *et al.* (2007) to back-calculate the stiffness of the solid unit of porous clay, were chosen for this study. Table 4.5 provides the mineralogical descriptions of these samples. The transversely isotropic elastic stiffness tensors were obtained for these four shales using UPV tests conducted on core samples. For three data sets of Kimmeridge shale, Jurassic shales, and Domnesteanu *et al.* (2002)'s sample, the elastic constants were measured in saturated conditions under different confining pressures. With increasing confining pressure, properties almost converged to constant values, which we infer are due to the closure of micro-cracks. As cracks are not considered in our modelling, the values corresponding to the highest confining pressure were selected for comparison. For Woodford shales the natural water content of the samples was preserved but no information was provided on the confining pressure.

The mineralogical data, provided in Table 4.5, were used along with homogenisation methods to estimate the five elastic constants for each sample. Based on the results obtained in the previous sections using numerical modelling, the SCS was adopted for the first stage of homogenisation. Both MT and SCS formulations were implemented for the second stage, in

Table 4.5: Mineralogical data for the shale samples of the UPV data sets (extracted from Hornby *et al.* (1994), Sierra *et al.* (2010) and Domnesteanu *et al.* (2002))

Sample	Kimmeridge Shale	Jurassic Shale	Woodford-1 Shale	Woodford-2 Shale	Domnesteanu *et al.* (2002)
Mineralogical Data	Volume Fraction (%)				
Quartz	30.5	31	-	-	44.4
Calcite	-	1	-	-	-
Pyrite	2.1	5	-	-	1.5
Feldspar	7.2	4	-	-	6.5
Porous clay	60.2	58	57.1	65.2	47.6
Sum of Non-Clay	39.8	42	42.9	34.8	52.4
Shale Porosity	2.5	10.5	16	15	14
Clay Porosity	4.15	18.1	28	23	29.4

which matrix-inclusion morphology is homogenised, in order to evaluate which strategy results in better predictions of macroscale mechanical behaviour. Considering the range of applicability of the presented formulation to homogenise matrix-inclusion morphology, being less than 40 % of total volumetric inclusions, initially, the first four samples which satisfy this limit are investigated. In addition, the elastic properties of quartz were used to homogenise samples for which only the volume fraction of non-clay minerals are available, as this mineral is usually the most common non-clay mineral in shales. Figure 4.14 illustrates the predicted and the experimental results of the elastic constants of transversely isotropic shales using both SCS-SCS and SCS-MT strategies with bars showing the experimental standard deviation for each constant. The values of these constants, Thomsen's anisotropy parameters of $\varepsilon = (C_{11} - C_{33})/2C_{33}$ and $\gamma = (C_{66} - C_{44})/2C_{44}$ and their relative errors (%) are also given in Tables 4.7 and 4.6.

Comparing the relative errors between two up-scaling strategies revealed that there is no clear superiority for one strategy over the other one. This result can be justified due to the fact that each component of the stiffness tensor is a combination of two elastic constants, for example for an isotropic material $C_{11} = E(1 - \nu)/((1 + \nu)(1 - 2\nu))$. As it was highlighted in Section 4, numerical studies using SCS and MT schemes for predicting homogenised elastic response of matrix-inclusion morphology showed that each of these elastic constants can be better predicted with one of these schemes. In fact, the error observed in homogenised stiffness tensor components can be seen as the combined error of homogenised elastic constants. It can be observed that both SCS-SCS and SCS-MT methods produce some theoretical errors. However, in general, it can be concluded that SCS-SCS performs slightly better, particularly in terms of capturing anisotropy.

The prediction errors are relatively lower for the elastic constants C_{11} and C_{33} compared to

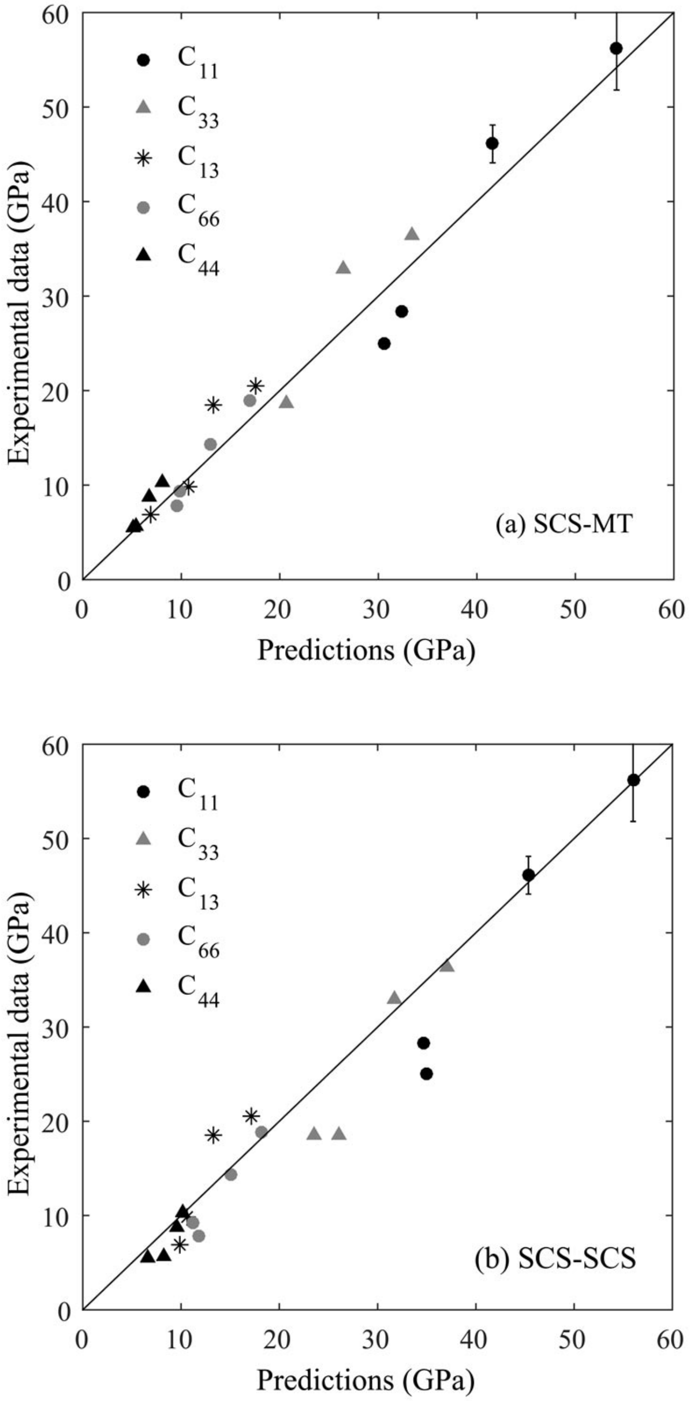

Figure 4.14: Summary of the experimental and predicted results for the UPV data sets shale samples using (a) SCS-MT and (b) SCS-SCS (vertical bars represent the standard deviations for the experimental data).

those for C_{13}. This can be explained by the high degree of measurement uncertainties in C_{13}, where the standard deviations are usually expected to be between 30% and 50% (Jones and Wang, 1981; Domnesteanu *et al.*, 2002; Jakobsen *et al.*, 2000). Additionally, Sayers (2013a) studied the anisotropic response of shales and concluded that the value of C_{13} can be affected

Table 4.6: Experimental (Exp) and predicted (Pred) elastic constants for the UPV data sets samples using using SCS-MT.

Elastic constant	Kimmeridge Shale			Jurassic Shale			Woodford-2 Shale			Woodford-2 Shale		
	Exp.	Pred.	Error	Exp.	Pred.	Error	Exp.	Pred.	Error	Exp.	Pred.	Error
C_{11}	56.2	54.2	3.55	46.1	41.6	9.76	25	30.6	22.4	28.3	32.5	14.8
C_{33}	36.4	33.5	8	32.9	26.4	19.7	18.6	20.6	10.7	18.6	20.7	11.2
C_{13}	20.5	17.6	14.1	18.5	13.3	28.1	6.9	10.1	46.3	9.8	10.8	10.2
C_{66}	18.9	17	10	14.3	13	9.1	7.8	9.5	21.7	9.3	9.9	6.45
C_{44}	10.3	8.1	21.3	8.8	6.7	23.8	5.7	5.4	5.26	5.5	5.1	7.3
ε	0.27	0.31	0.13	0.2	0.28	43.5	0.17	0.24	41	0.26	0.28	9.3
γ	0.41	0.54	31.5	0.31	0.47	50.4	0.18	0.37	106	0.34	0.47	36.2

Table 4.7: Experimental (Exp) and predicted (Pred) elastic constants for the UPV data sets samples using SCS-SCS.

Elastic constant	Kimmeridge Shale			Jurassic Shale			Woodford-2 Shale			Woodford-2 Shale		
	Exp.	Pred.	Error	Exp.	Pred.	Error	Exp.	Pred.	Error	Exp.	Pred.	Error
C_{11}	56.2	56	0.35	46.1	45.3	1.73	25	35	40	28.3	34.6	22.2
C_{33}	36.4	37	1.64	32.9	31.7	3.64	18.6	26	39.7	18.6	23.5	26.
C_{13}	20.5	17.2	16.1	18.5	13.3	28.1	6.9	9.96	44.3	9.8	10.6	8.16
C_{66}	18.9	18.2	3.70	14.3	15	4.9	7.8	11.8	51.2	9.3	11.1	19.3
C_{44}	10.3	10.2	0.97	8.8	9.5	7.95	5.7	8.2	43.8	5.5	6.6	20
ε	0.27	0.26	5.5	0.2	0.21	6.9	0.17	0.17	0.0	0.26	0.23	9.4
γ	0.41	0.39	6.0	0.31	0.29	7.3	0.18	0.21	19	0.34	0.34	0.0

by features such as the presence of microcracks in the sample, which is ignored in our model. Considering the complexity of shale microstructure in addition to the high standard deviations which are usually observed when measuring shale properties, we conclude that the homogenisation methods can provide valuable mechanical results simply and inexpensively, using just quantitative mineralogical descriptions of shales.

The data in Table 4.6 show that the anisotropy was captured very well for all the data sets. However, it is obvious that the absolute predicted elastic constants are not satisfactory for the case of Woodford shales in comparison with the results obtained for Kimmeridge and Jurassic shales. As the homogenisation overestimates the elastic modulus, this could be due to the lack of information on the confining pressures used in the Woodford data sets. This is a critical parameter in the UPV test results, as it can reduce the effect of microcracks, which are not considered in the modelling. For example, elevation in confining pressure from 5 MPa to 80 MPa increases C_{11} by 40% in Jurassic shale (Hornby, 1998). The TOC contents of these samples were not provided in the reference, which could also have significantly reduced the elastic response. Moreover, it is also of interest to compare these results with previous micro-mechanical modelling of the same data sets. Jakobsen *et al.* (2003) attempted to predict the Jurassic shale elastic response. Several strategies were tried and the best results they could achieve were close to the measured properties at a confining pressure of 20 MPa. Vasin *et al.* (2013) started with a single clay particle to build up a shale model for Kimmeridge shale. They could not manage to reproduce the elastic response using the shale characterization obtained experimentally. By increasing the porosity to more than 10% with a specific aspect ratio, a good agreement was achieved with the predicted results and the measured elastic constant at a confining pressure of 80 MPa. It should be emphasised that the predicted data here, are obtained solely using the shale characterisation presented in the literature (Hornby, 1998; Sierra *et al.*, 2010), without any further calibration.

In Section 4, it was shown that neither SCS nor MT can provide accurate prediction on the elastic properties of a composite with high concentrations of inclusion (e.g. more than 50 %). However, this conclusion was derived based on numerical simulation of simplified models; therefore, it has to be validated against the complex case of shale rocks. The last shale sample provided in Table 4.5 contains 52.4 % of total silt inclusion which could be a suitable data set to further assess the presented homogenisation strategy. Figure 4.15 shows the predicted values for the two elastic constants C_{11} and C_{33}, for this shale sample along with Kimmeridge and Jurassic shales, using both SCS-SCS and SCS-MT strategies. It is now better clear that the predicted values of SCS-SCS are comparable with the experimental results for Kimmeridge and Jurassic shales; however, none of the modelling strategies do perform well for the sample from Domnesteanu *et al.* (2002). In order to understand this prediction error, we need to refer back to Figures 4.4, where the basic problem of a single inclusion embedded in a matrix was considered. It can be seen that for high concentrations of inclusion, the elastic modulus lays somewhere between the predicted values by SCS and MT. Figure 4.15 clearly shows the elastic properties are underestimated and overestimated by the MT and SCS, respectively; which is completely consistent with the results obtained by numerical modelling. On the whole, the key to successful and reliable implementation of homogenisation formulations is to fully understand their limitations, range of applicability and representative microstructure.

4.6.4 Indentation data set on organic-rich shales

The significance of the effect of organic matter on the mechanical properties of shale rocks was illustrated in Chapter 3. Therefore, a proper modelling strategy in conjunction with suitable

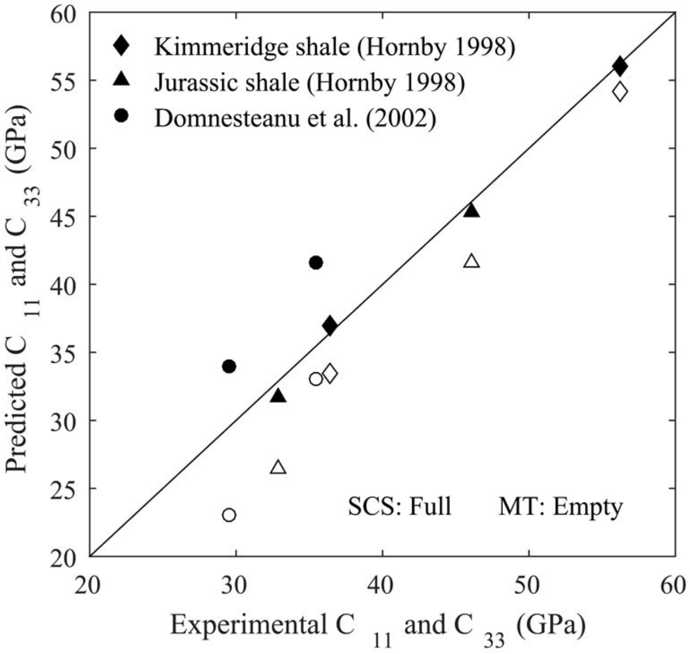

Figure 4.15: Experimental results versus predicted values for C_{11} and C_{33} of three shale samples with SCS at the fist level and both SCS and MT at the second level of homogenisation.

values for the elastic properties of this phase are essential in order to successfully conduct micromechanical modelling of organic-rich shales. There is a discrepancy between the reported elastic properties of kerogen in the literature. In this study, in chapter 2, a nanomechanical technique was implemented to conduct direct in-situ mechanical measurement on kerogen having different thermal maturity. These nanoscale measured data will be used in this section. Here, the rock physics modelling of organic-rich shale will be discussed in details.

Initially, the Toarcian shales of the Paris Basin are considered. These samples were characterised in terms of both petrophysical and mechanical properties, in Chapter 3. Table 4.8 provides all the characterisations required for the micromechanical modelling. However, as the porosity was not measured, an estimation of this parameter is required. Due to the fact that all the samples have been retrieved from similar depths, it is assumed that the clay packing density, η , is the same, in all samples. The clay packing density relates to the compaction state of clay particles and can be defined as: $\eta = 1 - \phi_{clay}$. This value can be back-calculated from one data set by equalising the experimental value to the predicted one. The obtained value is then used as the reference parameter for the rest of the experimental data. In addition, as these samples had been exposed to room-temperature for a long time before the test, the shale will be considered as dry, with no fluid within the pore spaces.

An assumption in the homogenisation formulation is that the matrix is considered as a con-

Table 4.8: Characterisations of Toarcian shale samples.

Sample ID	2	6	8	10
Quartz	29.33	6.5	9.28	25.63
Calcite	0.8	7.4	9.6	5.84
Pyrite	0.3	1.11	6.05	2.69
Feldspar	3.55	0.21	0.58	2.6
Dolomite	1.45	2.7	1.59	1.14
Kerogen, V_K	3.2	5.6	19.5	3.2
Porous Clay	61.32	87.68	53.4	58.9
Depth (m)	224.9	340	347.5	202.5

tinuous phase and the inclusions are isolated and fully surrounded by the matrix phase. SEM observations suggest that the organic matter is a semi-continuous phase, mixed with the porous clay. We therefore assume that the organic matter can be considered to be part of the shale matrix so that its contribution is taken into account, along with that of the porosity, in the first level of homogenisation. Previous approaches include considering organic matter as the background phase in shale (Vernik and Landis, 1996; Bayuk *et al.*, 2008; Sayers, 2013b), combining kerogen and solid clay as the elementary building block of the shale matrix (Ortega *et al.*, 2010), or adding kerogen as isloated inclusions (Guo *et al.*, 2014).

Based on the observation that kerogen in the tested samples does not increase the anisotropy ratio, here it is assumed that kerogen is mixed with a porous clay, having the same packing density in all the samples. The combination of these phases through the use of SCS enables us to reproduce a system of semi-continuous random pore and kerogen networks with no preferential orientation. This approach is consistent with the experimental observation (see Chapter 3, Figure 14), in which anisotropy is slightly reduced by an increase in kerogen. The mechanical properties of kerogen are important and controversial factors in the prediction of the overall mechanical response for organic-rich shale. As the current samples are immature, the value of 5.9 GPa for kerogen Young's modulus, obtained in Chapter 2, is adopted. The Poisson's ratio is also assumed to be 0.3.

Again the two strategies of SCS-MT and SCS-SCS are adopted for shale modelling. The clay packing density was calibrated to be approximately 0.88 and 0.84 for the first and the second strategies, respectively, based on the indentation modulus parallel to the bedding direction (M_1) for sample No. 2. The same packing densities were adopted for the remaining samples. Figure 4.16 summarizes the experimental data versus the predicted values for indentation moduli. Table 4.9 and 4.10 also provides these values along with their relative errors.

Considering the standard deviations in the indentation data, which create a range for the indentation moduli, it can be seen that almost all the predicted moduli are within these ranges. The model shows very good predictions of the effect of changing the kerogen and inclusion volume fractions, purely based on mineralogical composition. The results obtained using both strategies are quite acceptable. However, in two cases of samples No. 2 and No. 8, the experimental data show a higher anisotropy ratio (M_1/M_3) than the predictions. This could be attributed to the simplifications which assume spherical silt inclusions and pores/kerogen distributions with no preferential orientation. Although these effects can be easily introduced in the calculation by considering an elliptical shape for inclusions, it is simply not possible to quantify them by direct experimental measurements. Bayuk *et al.* (2008) mentioned that considering different combinations of these micro-structural features in the modelling, can produce similar anisotropy. This is one of the drawbacks of micro-mechanical modelling and also one of the reasons why a range of modelling strategies have been adopted for shale. A possible solution could be to combine micro-mechanical modelling, with fast and efficient indentation testing on shale cuttings, which cannot solely characterise full TI elastic constants of shales, in order to identify some of the potential sources of anisotropy and also calibrate the micro-structural features.

Table 4.9: Predicted results (Pred.) versus experimental measurements (Exp.) for SCS-MT strategy on Toarcian shales.

Sample No.	Clay packing density	Exp. M_1	Exp. M_3	Exp. M_1/M_3	Pred. M_1	Pred. M_3	Pred. (M_1/M_3)	Error M_1 (%)	Error M_3 (%)
2	0.88	30.3	17.2	1.76	30.3	20.3	1.5	0.0	18
6	0.88	27.4	17	1.61	26	16.45	1.58	5	3.2
8	0.88	20.6	12.6	1.63	22	15.8	1.4	6.8	25.4
10	0.88	28.5	-	-	30.8	-	-	8	-

Table 4.10: Predicted results (Pred.) versus experimental measurements (Exp.) for SCS-SCS strategy on Toarcian shales.

Sample No.	Clay packing density	Exp. M_1	Exp. M_3	Exp. M_1/M_3	Pred. M_1	Pred. M_3	Pred. (M_1/M_3)	Error M_1 (%)	Error M_3 (%)
2	0.84	30.3	17.2	1.76	30.3	21.8	1.39	0.0	26
6	0.84	27.4	17	1.61	25.5	16.3	1.57	6.9	4.1
8	0.84	20.6	12.6	1.63	21	15.5	1.36	1.9	23
10	0.84	28.5	-	-	31	-	-	8.7	-

Finally, a highly organic-rich Posidonia Shale sample (Wic-29) is also considered for the micro-mechanical modelling. The characterisation of this sample was discussed in Chapter 3.

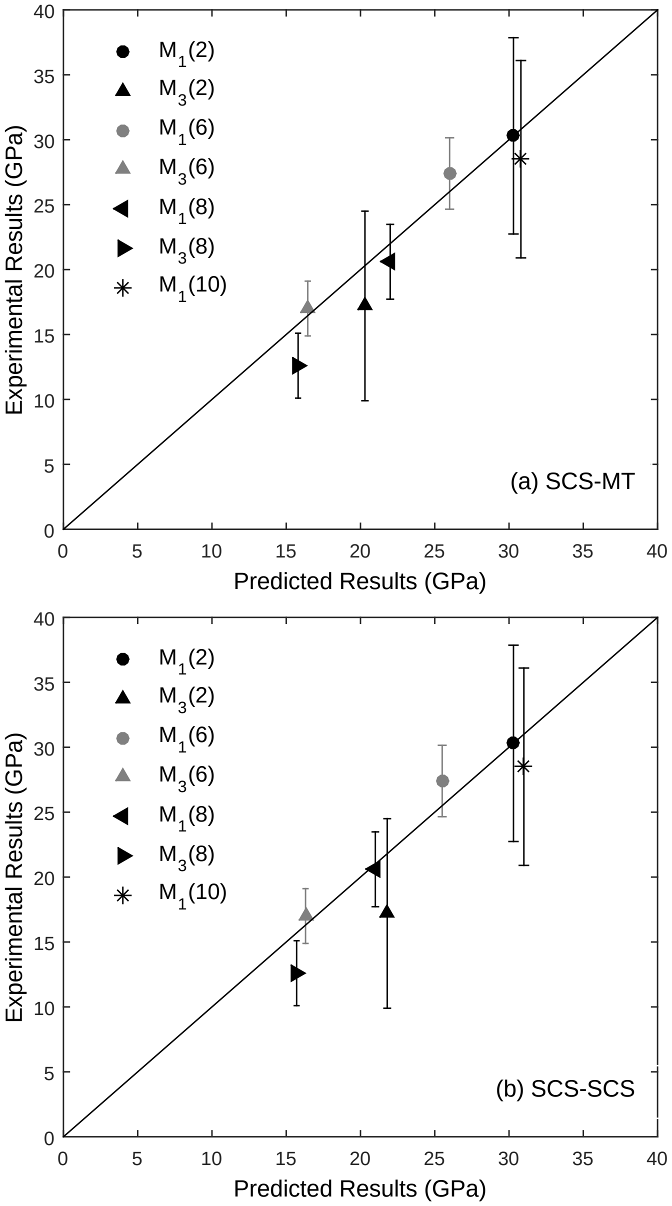

Figure 4.16: Summary of the experimental and predicted results for the Toarcian shale samples using (a) SCS-MT and (b) SCS-SCS (vertical bars represent the standard deviations for the experimental data).

Table 4.11 summaries the input data required for the modelling process. Table 4.12 provides the predicted results versus the experimental measurements for this sample. It can be observed that the SCS-SCS strategy slightly overestimates the indentation moduli; however, SCS-MT provides a very good prediction for the elastic response of the Posidonia Shale sample. Again, it should be noted that these results are obtained only based on the experimentally characterised shale properties, with no further calibration.

The kerogen elastic modulus of 5.9 GPa was obtained by direct nanoscale measurement on sample Wic-29, therefore, it is of interest to re-calculate the results using the kerogen properties reported in literature. The values of 8 GPa and 0.28 for Young's modulus and Poisson's ratio, which were back-calculated by Vernik and Nur (1992) have been used in several studies (Bayuk *et al.*, 2008; Ortega *et al.*, 2009; Sayers, 2013b). The homogenisation procedure will be repeated for sample Wic-29, with these kerogen properties, to assess the sensitivity of the predicted moduli to these parameters. Table 4.13 provides the newly predicted values for indentation moduli. It can be observed that the change in the kerogen Young's modulus, increased the error of predicted moduli around 20 %. In fact, none of the homogenisation strategies can provide reasonable values using this set of properties for kerogen. This can further highlight the importance of the data obtained by the PeakForce QNM®.

In general, shale microstructure is very complex and micromechanical modelling requires major simplifications in order to formulate it. Nevertheless, in this study, it was shown that the homogenisation can be adopted as an effective approach to better explain the experimental measurements or extrapolate them for depths for which the mechanical measurement may not be available. However, in order to confidently achieve this purpose, appropriate homogenisation strategies, a good understanding of their range of applicability and accurate and reliable input data are essential.

Table 4.11: Characterisations of the sample Wic-29.

Sample	Wic-29
Quartz	9.05
Feldspar	1.97
Calcite	25.3
Dolomite	0.62
Pyrite	1.85
Clay	26.04
Kerogen	24.87
Porosity	10.3

Table 4.12: Experimental measurements (Exp.) versus predicted results (Pred.) using kerogen properties obtained by nanomechanical mapping.

Modelling strategy	Exp. M_1	Exp. M_3	Exp. M_1/M_3	Pred. M_1	Pred. M_3	Pred. M_1/M_3	Error M_1 (%)	Error M_3 (%)
SCS-MT	14.1	11.7	1.2	14.6	12.3	1.19	4	5.6
SCS-SCS				16.2	14.2	1.4	14.9	21.8

Table 4.13: Experimental measurements (Exp.) versus predicted results (Pred.) using kerogen properties reported by Vernik and Nur (1992).

Modelling strategy	Exp. M_1	Exp. M_3	Exp. M_1/M_3	Pred. M_1	Pred. M_3	Pred. M_1/M_3	Error M_1 (%)	Error M_3 (%)
SCS-MT	14.1	11.7	1.2	17.02	14.24	1.19	20.7	21.7
SCS-SCS				19.6	17.01	1.15	39	45.4

4.7 Summary and conclusion

In this study, the possibility of adopting homogenisation techniques in order to explain the macroscopic response of shale rocks was investigated. First, a comparative evaluation study using different homogenisation schemes and numerical simulations that account for microstructures has been carried out. Shales were considered to be two-level composites consisting of clay particles, kerogen and pores at the first level and a matrix with silt mineral inclusions at the second level. Different simplified microstructures related to these levels were simulated to determine suitable homogenisation strategies for shale rocks. Finally, several experimental data obtained on core samples and shale cuttings, were considered to evaluate the performance and accuracy of these micromechanical formulations as a predictive tool for elastic response of shale rocks.

The results of numerical simulation of matrix-inclusion morphology reveal that MT and GSCS homogenisation schemes, provide the most accurate predictions of the homogenised bulk modulus; the SCS model overestimated the bulk modulus, particularly when the volume fraction of inclusions is high. In contrast, the Young's modulus is better predicted by the SCS model, for materials with up to 40% volume fraction of inclusions. Consequently, no clear advantage was offered by either scheme in predicting the homogenised stiffness matrix, for which all the components are functions of the two elastic constants, i.e. the bulk and shear moduli.

Two different microstructures for the porous clay matrix were considered, one consisting of isolated pores and a second with a connected pore network. For a system with isolated pores, the MT model reproduces the macroscopic response more accurately, whilst the SCS model is more effective for a matrix with a pore network. In addition, pore networks for shales with (a) randomly distributed pores and (b) stochastically-developed pore networks using SEM images, have been simulated and the results were compared with those obtained using homogenisation techniques. In both cases, the SCS gives the best prediction of the macroscopic rock stiffness response, with an almost linear porosity-stiffness relationship up to 50% porosity, similar to experimental studies on the mechanical response of the clay matrix in shales.

These results, along with the experimental data which suggest that most pores in shales are connected, show that the SCS is the most appropriate model with which to homogenise the elastic properties of a porous clay matrix. Importantly, the conceptual, randomly distributed pore system could be adopted as a model for clay matrix with which to study the macroscopic elastic-plastic response of fine-grained sedimentary rocks dominated by a porous clay matrix.

Results from the homogenisation method were then evaluated against the limited geomechanical data sets available in the literature. Considering the multiscale complexity of shales and also the high standard deviations usually obtained in mechanical experiments on shale samples, the values estimated by the homogenisation method, which are based solely on mineralogical descriptions, provide valuable predictions of the mechanical response. Additionally, comparing SCS and MT for the second level of homogenisation, it was concluded that SCS produced just slightly better prediction of elastic response with a very good estimate of anisotropy. A shale sample with high level of concentration of silt inclusion, more than 50 %, was also investigated. It was observed that the mechanical response of this sample lies between the predictions by SCS-MT and SCS-SCS. This observation is in agreement with the results obtained by numerical simulation, which further highlights the sufficiency of numerical study on determination of the range of applicability of homogenisation methods.

Finally, in order to study the homogenisation methods for the case of organic-rich shales, the results obtained in Chapter 3 using advanced indentation tests, were used as validation data sets. Based on the observations in the nanoscale mechanical maps and SEM images, the organic matters content of shale samples was taken into account in the first level of homogenisation, in a similar fashion to porosity, with the elastic modulus being measured by nano-mechanical mapping in Chapter 2. A comparison between the predicted indentation moduli and the experimental values confirms the capability of the multi-scale homogenisation method to predict the effect of kerogen on the elastic response of shales, provided that this phase is suitably accounted for. However, micro-structural features such as grain shape or pore aspect ratio, which cannot be measured directly, need to be calibrated in order to further adjust the predicted anisotropy. This calibration can be performed using the indentation data set, which can be obtained from shale cuttings. Generally, it can be concluded that the homogenisation technique can be effectively used as an auxiliary approach to conventional rock mechanics tests to estimate the elastic response of shale rocks, using petrological and mechanical properties of shale cuttings.

References

Abou-Chakra Guery A., Cormery F., Shao F., Kondo D. 2010. A comparative micromechanical analysis of the effective properties of a geomaterial: effect of mineralogical compositions. *Computers and Geotechniques*, **37**, 585-593.

Antonangeli D., Krish M., Fiquet G., Badro J., Farber D.L., Bossak A., Merkel S. 2005. Aggregate and single-crystalline elasticity of hcp cobalt at high pressure. *Physical Review B* **72**(13).

Andersen, S., Andersen L. 2010. Modelling of landslides with the material-point method. Computational Geoscience, **14**, 137-147.

Andersen S., Andersen L. 2010. Analysis of spatial interpolation in the material-point method. *Computers and Structures*, **88**, 506-518.

Bardenhagen, SG., Kober, E.M. 2004. The generalized interpolation material point method. *Computer Modeling in Engineering and Sciences*, **5**(6), 477–495.

Bass J.D. 1995. Elasticity of minerals, glasses, and melts. In: [Minerals Physics & Crystallography: A handbook of physical constants] (ed. T.J. Ahrens), pp. 45-63. *AGU Reference Shelf.*

Bayuk I.O., Ammerman M., Chesnokov E.M. 2008. Upscaling of elastic properties of anisotropic sedimentary rocks. *Geophysical Journal International*, **172**, 842–860.

Benveniste, Y. 2008. Revisiting the generalized Self-Consistent Scheme in composites: clarification of some aspects and a new formulation. *Journal of the Mechanics and Physics of Solids*, **56**, 2984-3002.

Beuth L., Wieckowski Z., Vermeer P.A. 2011. Solution of quasi-static large-strain problems by the material point method. *International Journal for Numerical and Analytical Methods in Geomechanics*, **35**, 1451-1465.

Bobko C., Ulm F.J. 2008 The nano-mechanical morphology of shale. *Mechanics of Material*, **40**, 318-337.

Chalmers G.R., Bustin R.M., Power I.M. 2012. Characterization of gas shale pore systems by porosimetry, pycnometry, surface area, and field emission scanning electron microscopy/transmission electron microscopy image analyses: examples from the Barnett, Woodford, Haynesville, Marcellus and Doig units. *The American Association of Petroleum Geologists Bulletin*, **96**(6), 1099-1119.

Chateau X., Dormieux L. 2002. Micromechanics of saturated and unsaturated porous media. *International Journal for Numerical and Analytical Methods in Geomechanics*, **26**, 831-844.

Chen L., Zhang L., Kang Q., Viswanathan H.S., Yao J., Tao W. 2015. Nanoscale simulation of shale transport properties using the lattice Boltzmann method: permeability and diffusivity. *Scientific Reports*, **5**(8089).

Christensen R.M., Lo K.H. 1979. Solutions for effective and shear properties in three phase and cylinder models. *Journal of the Mechanics and Physics of Solids*, **27**, 315-330.

Domnesteanu P., McCann C., Sothcott J. 2002. Velocity anisotropy and attenuation of shale in under- and overpressured conditions. Geophysical Prospecting, **50**, 487-503.

Draege A., Jakobsen M., Johansen T.A. 2006. Rock physics modelling of shale diagenesis. *Petroleum Geoscience* **12**, 49-57.

Fritsch, A. Hellmich, C. 2007. Universal microstructural patterns in cortical and trabecular, extracellular and extravascular bone materials: Micromechanics-based prediction of anisotropic elasticity. *Journal of Theoretical Biology*, **224**, 597–620.

Guo Z.Q., Li X.Y., Liu C. 2014. Anisotropy parameters estimate and rock physics analysis for the Barnett Shale. *Journal of Geophysics and Engineering*, **11**, 065006.

Hbaieb K., Wang Q.X., Chia Y.H.J. Cotterell, B. 2007. Modelling stiffness of polymer/clay nanocomposites. *Polymer*, **48**, 901-909.

Hill R. 1965. A self-consistent mechanics of composite materials. *Journal of Mechanics and Physics of Solids*, **13**, 213-222.

Hornby B.E., Schwartz L., Hudson J. 1994 Anisotropic effective medium modeling of the elastic properties of shales. *Geophysics*, **59**, 1570-83.

Hornby B.E. 1998. Experimental laboratory determination of the dynamic elastic properties of wet, drained shales. *Journal of Geophysical Research*, **103**(B12), 29945-29964.

Jakobsen M. and Johansen T.A. 2000. Anisotropic approximations for mudrocks: A seismic laboratory study. *Geophysics* **45**(6), 1711-1725.

Jakobsen M., Hudson J.A., Johansen T.A. 2003. T-matrix approach to shale acoustics. *Geophysical Journal International*, **154**, 533–558.

Jassim I., Stolle D., Vermeer P. 2012. Two-phase dynamic analysis by material point method. *International Journal for Numerical and Analytical Methods in Geomechanics*.

Jones L.E.A., Wang H.F. 1981. Ultrasonic velocities in Cretaceous shales from the Williston basin. *Geophysics*, **46**(3), 288-297.

Kanitpanyacharoen W., Wenk H.R., Kets F., Lehr C., Wirth R. 2011. Texture and anisotropy analysis of Qusaiba shales. *Geophysical Prospecting*, **59**, 536–556.

Klusemann B., Svendsen B. 2010. Homogenisation methods for multi-phase elastic composites: Comparisons and benchmarks. *Technische Mechanik*, **3**0(4), 374-386.

Kumar V., Sondergeld C., Rai C.S. 2015. Effect of mineralogy and organic matter on mechanical properties of shale. *Interpretation*, **3**(3), SV9-SV15.

Ma J., Sanchez J.P., Wu K., Couples G.D., Jiang Z. 2014. A pore network model for simulating non-ideal gas flow in micro- and nano-porous materials. *Fuel*, **116**, 498-508.

Maghous S., Dormieux, L., Barthelemy, J.F. 2009. Micromechanical approach to the strength properties of frictional geomaterials. *European Journal of Mechanics*, **28**, 179-188.

Mast C.M., Mackenzie-Helnwein P., Arduino P., Miller G.R., Shin W. 2012. Mitigating kinematic locking in the material point method. *Journal of Computational Physics*, **231**, 5351-5373.

Mast C.M., Arduino P., Miller G.R., Shin W., Mackenzie-Helnwein P. 2015. Avalanche and landslide simulation using the material point method: flow dynamics and force interaction with structures. *Computational Geoscience*, **231**, 5351-5373.

Mavko G., Mukerji T., Dvorkin J. 2009. The rock physics handbook. Cambridge University Press. ISBN 9780521861366.

Meier T., Ryback E., Reinicke A., Dresen G. 2013. Influence of borehole diameter on the formation of borehole breakouts in black shale. *International Journal of Rock Mechanics and Mining Sciences*, **62**, 74-85.

Mori T., Tanaka K. 1973. Average stress in matrix and average elastic energy of materials with misfitting inclusions. *Acta Metallurgica*, **21**.

Mortazavi B., Baniassadi M., Bardon J., Ahzi S. 2013. Modeling of two-phase random composite materials by finite element, Mori–Tanaka and strong contrast methods. *Composites: Part B*, **45**, 1117-1125.

Moussaddy H., Therriault D., Lévesque M. 2013. A numerical approximation to the elastic properties of shpare reinforced composite. In: The 19th International Conference Composite Materials.

Naraghia M.E., Javadpour F. 2015. A stochastic permeability model for the shale-gas systems. *International Journal of Coal Geology*, **140**, 111-124.

Onoda G.Y., Liniger E.G. 1990. Random loose packings of uniform spheres and the dilatancy onset. *Physical Review Letters*, **64**(22), 2727-2730.

Qin X., Han D., Zhao L. 2014. Rock physics modeling of organic-rich shales with different maturity levels. *SEG Technical Program Expanded Abstracts*, 2952-2957.

Ortega J.A., Ulm F.J., Abousleiman Y.N. 2007. The effect of the nanogranular nature of shale on their poroelastic behavior. *Acta Geotechnica*, **2**, 155-182.

Ortega J.A., Ulm F.J., Abousleiman Y. 2009. The nanogranular acoustic signature of shale.

Geophysics, **74**(3), D65-D84.

Ortega J.A., Ulm F.J., Abousleiman Y. 2010. The effect of particle shape and grain-scale properties of shale: A micromechanics approach. *International Journal of Numerical and Analytical Method in Geomechanics* **34**, 1124-1156.

Peng S., Yang J., Xiao X., Loucks B., Ruppel S. and Zhang T. 2015. An integrated method for upscaling pore-network characterization and permeability estimation: example from the Mississippian Barnett shale. *Transport in Porous Media*, **109**, 359–376.

Rybacki E., Reinicke A., Meier T., Makasi M., Dresen G. 2015. What controls the mechanical properties of shale rocks? – Part I: Strength and Young's modulus. *Journal of Petroleum Science and Engineering*, **135**, 702-722.

Sayers C.M. 1994. The elastic anisotropy of shales. *Journal of Geophysical Research*, **99**(B1), 767-774.

Sayers C.M. 2013a. The effect of anisotropy on the Young's moduli and Poisson's ratios of shales. *Geophysical Prospecting*, **61**, 416-426.

Sayers C.M. 2013. The effect of kerogen on the elastic anisotropy of organic-rich shales. *Geophysics*, **78**(2), D65-D74.

Segurado J., Llorca J. 2002. A numerical approximation to the elastic properties of shpere reinforced composite. *Journal of the Mechanics and Physics of Solids*, **50**, 2107-2121.

Schmauder S., Weber U., Soppa E. 2003. Computational micromechanics of heterogeneous materials. *Key Engineering Materials*, **251-252**, 415-422.

Shen W.Q., Shao J.F., Kondo D., Gatmiri B. 2012. A micro–macro model for clayey rocks with a plastic compressible porous matrix. *International Journal of Plasticity*, **36**, 64-85.

Shen W.Q., Kondo D., Dormieux L., Shao J.F. 2013. A closed-form three scale model for ductile rocks with a plastically compressible porous matrix. *Mechanics of Materials*, **59**, 73-86.

Sierra R., Tran M.H., Abousleiman Y.N., Slatt R.M. 2010. Woodford Shale Mechanical Properties and the Impacts of Lithofacies. In: the 44th US Rock Mech. Symp. (ARMA) 10-461.

Stransky J., Vorel J., Zeman J., Sejnoha M. 2011. Mori-Tanaka based estimates of effective thermal conductivity of various engineering materials. *Micromachines*, **2**, 129-149.

Sulsky D., Schreyer H.L., 1996. Axisymmetric form of the material point method with applications to upsetting and Taylor impact problems. *Computer Methods in Applied Mechanics and Engineering*, **139**, 409-429.

Sulsky D., Schreyer H.L., 1996. Axisymmetric form of the material point method with applications to upsetting and Taylor impact problems. *Computer Methods in Applied Mechanics*

and Engineering, **139**, 409-429.

Ulm F.J., Abousleiman Y. 2006. The nanogranular nature of shale. *Acta Geotechnica*, **1**, 77-88.

Vasin R.N., Wenk H.R., Kanitpanyacharoen W., Matthies S., Wirth R. 2013. Elastic anisotropy modeling of Kimmeridge shale. *Journal of Geophysical Research: Solid Earth*, **118**, 3931-3956.

Vernik L., Nur A. 1992. Ultrasonic velocity and anisotropy of hyrdocarbon source rocks. *Geophysics*, **57**(5), 727-735.

Vernik L., Landis C. 1996. Elastic anisotropy of source rocks: Implication for HC generation and primary migration. *AAPG Bulletin*, **80**, 531-544.

Vernik L., Liu X. 1997. Velocity anisotropy in shales: A petrophysical study. *Geophysics*, **62**(2), 521-532.

Vernik L., Milovac J. 2011. Rock physics of organic shales. *The Leading Edge*, **30**, 318-323.

Wang Z., Wang H., Cates M.E. 2001. Effective elastic properties of solid clays. *Geophysics*, **66**(2), 428-440.

Whitaker M.L., Liu W., Wang L. Li B. 2010. Acoustic Velocities and Elastic Properties of Pyrite (FeS2) to 9.6 GPa. *Journal of Earth Science*, **21**, 792-80.

Wieckowski Z. 2004. The material point method in large strain engineering problems. *Computer Methods in Applied Mechanics and Engineering*, **193**, 4417–4438.

Wu X., Chapman M., Li X.Y., Dai H. 2012. Anisotropic elastic modelling for organic shales. 74th EAGE Conference and Exhibition SPE EUROPEC.

Zaoui A. 2012. Continuum micromechanics: survey. *Journal of Engineering Mechanics*, **128**(8), 808-816.

Zeszotarski J.C., Chromik R.R., Vinci R.P., Messmer M.C., Michels R., Larsen J.W. 2004. Imaging and mechanical property measurements of kerogen via nanoindentation. *Geochimica et Cosmochimica Acta*, **68**, 4113-4119.

Zhang Q., Zhu H., Zhang L., Ding X. 2011. Study of scale effect on intact rock strength using particle flow modeling. *International Journal of Rock Mechanics and Mining Sciences*, **48**, 1320-1328.

Zhu Y., Xu S., Payne M., Martinez A., Liu E., Harris C., Bandyopadhyay, K. 2012. Improved rock-physics model for shale gas reservoirs. 82nd SEG Meeting Expanded Abstracts 0927.

Zu Y., Xu S., Liu E., Payne M.A., Terrell M.J. 2013. Predicting anisotropic source rock properties from well data: U.S. Patent 2013/0013209 A1.

Chapter 5

Inverse analysis of indentation test on organic-rich shale using Material Point Method

5.1 Introduction

Drilling wells has always been a challenging task in the oil and gas industry due to the high probability of well bore instability (Meier *et al.*, 2013, 2015). A safe and economic design of the drilling procedure, including the design of drilling mud weight and well casing, requires reliable data on the non-linear mechanical response of the host rock. The most traditional approach to constrain the elastoplastic properties of rocks, is to undertake uniaxial or triaxial tests on core samples retrieved from well bores. Many attempts have been devoted to measure or to predict the elastic response of shale rocks using different approaches, ranging from micromechanical models to indentation testing on shale cuttings and in-situ Ultra-sonic Pulse Velocity (UPV) in well bores. On the other hand, the estimation of plastic material parameters are still in the realm of laboratory tests on rock cores.

Some researchers attempted to develop micromechanical models that are able to relate the macroscopic plastic response of shale to its microstructure (Barthelemy *et al.*, 2004; Abou-Chakra Guery *et al.*, 2008a, 2008b; Lin *et al.*, 2012; Shen *et al.*, 2012, 2013). However, due to the high complexity of the plastic response, they imposed several simplifications in order to make it possible to formulate the micromechanical models. For instance, the porous clay matrix was considered to be composed of solid and spherical isolated pores or the whole elastoplastic response at different scales was assumed to be isotropic. Neither experimental observations

(Bobko and Ulm, 2008; Goodarzi *et al.*, 2017) nor theoretical studies (Ulm and Abousleiman 2006; Goodarzi *et al.*, 2016) are consistent with these assumptions. The applicability of these micromechanical models to shale rocks is still questionable.

The indentation test has found its way into the shale industry, due to its feasibility to be conducted on simple cuttings. Additionally, the good correlation between the elastic modulus obtained from this test and the modulus determined by UPV testing on core samples showed the capability of indentation as a useful tool in shales characterisation (Kumar *et al.*, 2012). Unlike the elastic modulus, which can be directly derived from indentation load-displacement curves, plasticity parameters cannot be easily obtained from the same curves. In fact, only the so-called hardness index, which can indirectly be related to the elastoplastic response of the material, can be determined. This index can provide a means of comparing different materials, but the conventional material plasticity parameters, such as cohesion or angle of internal friction, cannot be simply inferred from this value.

The indentation test involves penetration, which induces both material and geometrical nonlinearities. Therefore, an analytical formulation cannot be developed to fully capture the evolving state of material in this test. Advances in the finite element method made it possible, to some extent, to simulate such a process, which is associated with excessive deformations of a solid mass. Since then, several studies have been focused on the simulation of indentation test to better understand the factors that affect the load-displacement curve obtained through the test. Min *et al.* (2003) studied the load-displacement response and plastic zone of indenters having different geometries. They concluded that the Berkovich indenter response can be considered equivalent to a conical indenter having a semi apex angle equal to 70.3^o. This finding is of great importance as it can help to simplify the three dimensional problem of the indentation test with a Berkovich indenter to a simple axisymmetric model. The effect of the frictional contact on indentation results was investigated by different researchers (Cheng and Cheng, 2004; Sarris and Constantinides, 2013) and was found to be influential when very high values are selected, which does not reflect the realistic contact between the indenter and well polished metals, glasses or ceramics. Consequently, most of the studies have been carried out with the assumption of a frictionless contact (Antunes *et al.*, 2006; Magnenet *et al.*, 2009; Rauchs and Bardon, 2011). Magnenet *et al.* (2009), considered a material obeying the Drucker-Prager failure criterion and investigated the sensitivity of the load-displacement curve to changes in the elastoplastic material parameters, using five different indenters. It was concluded that the final results are highly influenced by the angle of internal friction, whereas Poisson's ratio has a minor effect. Additionally, their results proved that sharp indenters (conical or Berkovich) perform better than flat tip indenters, such as cylindrical or cubical. Some attempts have been devoted to extracting the stress-strain relationship of metals and polymers by inverse analysis of indentation load-displacement curves (Dao *et al.*, 2001; Magnenet *et al.*, 2009; Lee *et al.*, 2010; Bennett *et al.*, 2015). Tho *et al.* (2004) showed that every load-displacement curve has three quantities, namely the curvature loading path, the initial slope of the unloading curve, and the ratio of residual depth to maximum indentation depth. They derived an analytical solution linking these three quantities and proved that only two quantities can be independent. It should be noted that in the simplest form of a constitutive model, at least three parameters, two elastic constants and one plasticity index, are required to describe the material response. This implies that inverse analysis of a single load-displacement curve cannot lead to a unique set of properties. In fact, an infinite combination of these parameters may produce identical load-displacement curves. In order to mitigate this problem by equating the number of unknowns and knowns, it has been suggested to perform inverse analysis on several load-displacement curves obtained from indenters of different geometries (Bucaille *et al.*, 2003; Seltzer *et al.*, 2011).

In this chapter, the feasibility of using the indentation test for estimating strength parameters of shale rocks is investigated. In order to pursue this aim, numerical simulations are undertaken to back-calculate plastic parameters by calibrating the numerical results against experimental load-displacement curves. Several well-characterised shale samples were subjected to indentation tests using different indenters in order to generate various stress-strain paths in the samples. The Berkovich and spherical indenters were used for this purpose under load controlled conditions set at 500 mN. In order to undertake the numerical simulations, a recently developed technique known as the material point method (MPM), which is considered to be an extension of the conventional finite element method (FEM) for large deformation problems, is adopted (Sulsky *et al.*, 1994, 1996; Coetzee *et al.*, 2005). The MPM can be considered as an unconditionally stable method when geometrical nonlinearities are involved, with no need for any extra treatment to handle excessive deformations. An explicit MPM formulation is implemented along with displacement boundary conditions and a contact algorithm. The shale samples are assumed to obey the Drucker-Prager failure criterion with no hardening. The cohesion and the internal angle of friction are back-calculated by simultaneous calibrations of load-displacement curves obtained by the Berkovich and spherical indenters on each samples. The effects of the frictional contact between the indenter and the sample will also be discussed in this study.

5.2 Computational tool

The indentation test involves excessive deformation of the material underneath the indenter through a contact surface, which increases the complexity of this problem. Such phenomenon has always been a challenging task in computational mechanics and several approaches have been proposed to deal with the issues related to contact. Numerous papers have been published tackling this issue by keeping the original mesh-based FEM formulation and using re-meshing methods, to avoid the extensive mesh distortion (Hu and Randolph, 1998; Nazem *et al.*, 2006, 2008). One of the main problems associated with these techniques is that mapping of state variables from the old mesh to the new one may result in numerical errors. Additionally, in history-dependent constitutive models, which are widely used in geomaterials, the history of each point of the body mass cannot be fully tracked throughout the simulation. Effort has been directed at the formulation of the so-called mesh free techniques, which are based on particles. All the state variables are carried on these particles and the integration is also performed on the same particles. Therefore, the history of each material point can be preserved without any mesh distortion that might terminate the simulation (Sulsky *et al.*, 1994; Li *et al.*, 2000; Qiu *et al.*, 2011; Bui *et al.*, 2008, 2013). The complete presentation of the advantages and disadvantages of these algorithmic treatments for large deformation problems is out of the scope of this study. However, among all of them, MPM has recently gained popularity due to its capability to simulate very large deformation without any extra effort along with its simple formulation. Additionally, it was shown that MPM is computationally more efficient and accurate than the mesh free methods such as Smoothed-Particle Hydrodynamics (SPH) (Ma *et al.*, 2009).

The original MPM proposed by (Sulsky *et al.*, 1994, 1996) was mainly suitable for impact problems, in which the inertia is high and the contact with no-penetration is sufficient. For problems closer to a quasi-static condition, the internal forces should be in equilibrium with the external forces. However, the first derivative of the shape functions for linear elements are discontinuous, which can lead to numerical noise in the simulation, known as the particle crossing phenomenon. This problem has been discussed in many studies and several improvements including the use of the Generalized Interpolation (Bardenhagen and Kober, 2004), Spline shape function (Steffen *et al.*, 2008; Andersen *et al.*, 2010) and mixed integration (Beuth *et al.*, 2011) were proposed to solve such a problem. Moreover, a computationally simple and efficient algorithm for frictional contact was proposed by Bardenhagen *et al.* (2000, 2001).

The basic equations of MPM and the adopted contact algorithms are provided in the Appendix B. The integration schemes and boundary conditions will be discussed in the following sections.

5.2.1 Integration in MPM

The majority of published MPM works were either based on the original MPM integration or the Generalized Interpolation Material Point (GIMP). The continuous shape functions of the GIMP, significantly reduce the particle crossing noise and the potentially associated instability. The GIMP formulation has been provided and discussed in literature (Bardenhagen and Kober, 2004; Buzzi *et al.*, 2008; Narin and Guilkey, 2015; Solowski and Sloan, 2015). Beuth *et al.* (2011) developed the so-called mixed integration method for quasi-static MPM formulation. In this technique, the conventional finite element Gaussian integration is adopted for fully filled elements inside the body and the conventional MPM integration is adopted for the partially filled elements around the boundary.

In order to perform the mixed integration in every calculation steps, the partially filled elements need to be detected around the boundary. For the internal fully filled elements, a mapping procedure is required to transfer the MPs data inside each element to the Gauss points (GPs) and vice versa. Eq. 5.1 shows the criterion for detecting partially filled elements:

$$\sum_{i=1}^{n_p} V_p < \beta V_{Elm} \tag{5.1}$$

where n$_p$ is the total number of material points (MPs) inside an element, V$_p$ is the MP volume, V$_{Elm}$ is the volume of the element, and β is a constant. Through a sensitivity analysis, it was found out that values between 0.8 to 0.9 are suitable for β.

In explicit MPM formulations, only linear elements can be adopted, being either triangular or rectangular elements. For the case of these two elements, one GP is sufficient, which allows the mapping procedure to be straightforward. A weighted average of all the MPs inside an element can be assigned to the GP and the updated values obtained on the GP can be considered for all the MPs inside that element. Eq. 5.2 shows the weighted averaging of MPs' stress.

$$\sigma_{GP} = \frac{\sum\limits_{i=1}^{n} \sigma_p V_p}{\sum\limits_{i=1}^{n_p} V_p} \tag{5.2}$$

where σ_p is the MP stress state, and σ_{GP} is the mapped stress state over to the Gauss point. The same procedure can be considered for all other types of state variables such as strains, stresses and hardening parameters.

5.2.2 Prescribed kinematic condition

The prescribed displacement boundary condition is trivial in conventional mesh-based techniques such as FEM. In explicit formulations, it can be easily achieved by applying a constant velocity to nodes over a given period of time. However, in MPM, as the material points are located inside the body, any prescribed state variable on them have to be mapped to the nodes. This may result, after several element crossings, in an inaccurate implementation of the prescribed boundary condition. Hamad (2014) proposed using a set of additional boundary particles which can carry the prescribed kinematic condition. All the nodes involved with these boundary particles are considered as boundary nodes and are only subjected to mapped velocities from boundary particles. Hamad (2014) also highlighted that inaccuracy may be obtained with this scheme, particularly when one boundary element is not fully filled with boundary particles. Beuth (2012) used a scheme known as a moving mesh boundary, in which the prescribed kinematic condition is initially applied on the nodes as they move during the simulation. However, this approach is limited to an irregular mesh, which has to obey the contact surface.

Here, a very stiff indenter is pushed into the shale sample with a constant velocity and the indenter is normally assumed to be a rigid body (Dao *et al.*, 2001; Bucaille *et al.*, 2003; Seltzer *et al.*, 2011). The increase in elastic modulus of the material points that represent the indenter significantly reduces the critical time step for explicit analysis. In order to solve this problem in a simple and inexpensive way, it is attempted to dominate the momentum being mapped from indenter on contact nodes. A very high virtual density is attributed to the indenter. On the contact nodes, where momentum is received from both sample and indenter, the high mass of the indenter's material points imposes the indenter momentum. Therefore, the final calculated velocities at the contact nodes are significantly influenced by the velocity of the indenter and the accuracy of the solution depends on the mass of the indenter. The author's experience showed that a multiplier of 1×10^4 is quite sufficient to be applied on the density of the indenter. It should be noted that as the mass of the indenter is increased, there is no negative effect on the critical time step.

5.2.3 Verification examples

An important step of the development of a computational tool is the validation stage. Results can be compared with existing analytical solutions or other validated computational codes. There are only few very simple examples, such as bending of a cantilever beam, for which an analytical solution has been derived under large deformation conditions. Therefore, in this study, the developed MPM code is validated against a few more sophisticated examples, using the finite element code ABAQUS. Three validation examples are simulated to illustrate the performance of the presented axisymmetric formulation along with the constitutive models and the mixed integration involving large deformations and contact mechanics.

Uniaxial compression test

A simple yet robust example, which allows evaluation of the implementation of constitutive models, is the triaxial test. Here, an axisymmetric model under small strain conditions is simulated, using both von Mises and Drucker-Prager constitutive models. No confining pressure is applied, so the Uniaxial Compression Strength (UCS) test is imposed. Figure 5.1 shows the geometry and boundary conditions of the model with a displacement boundary condition applied at the top of the model. The material parameters are provided in Table 5.2. It should be noted that for von Mises model, only the cohesion is taken into account.

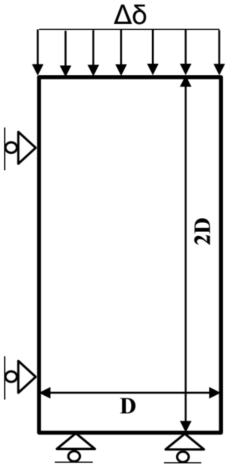

Figure 5.1: Geometry and boundary conditions for the UCS test.

Table 5.1: Soil properties for the UCS test.

Parameter	Unit	Value
Young's modulus, E	(kPa)	1×10^4
Poisson's ratio, ν	-	0.3
Angle of internal friction, ϕ	^{o}	30
Cohesion, C	(kPa)	1×10^2

Figure 5.2 shows the stress-strain curves for both models for the uniaxial compression strength (see Eq. 5.3). It can be seen that the simulation results are in good agreement with the analytical solution, which demonstrates the correct implementation of the formulation and

constitutive models.

$$UCS = \begin{cases} 2C & \text{von Mises;} \\ \dfrac{2C\cos\phi}{1-\sin\phi} & \text{Drucker-Prager.} \end{cases} \tag{5.3}$$

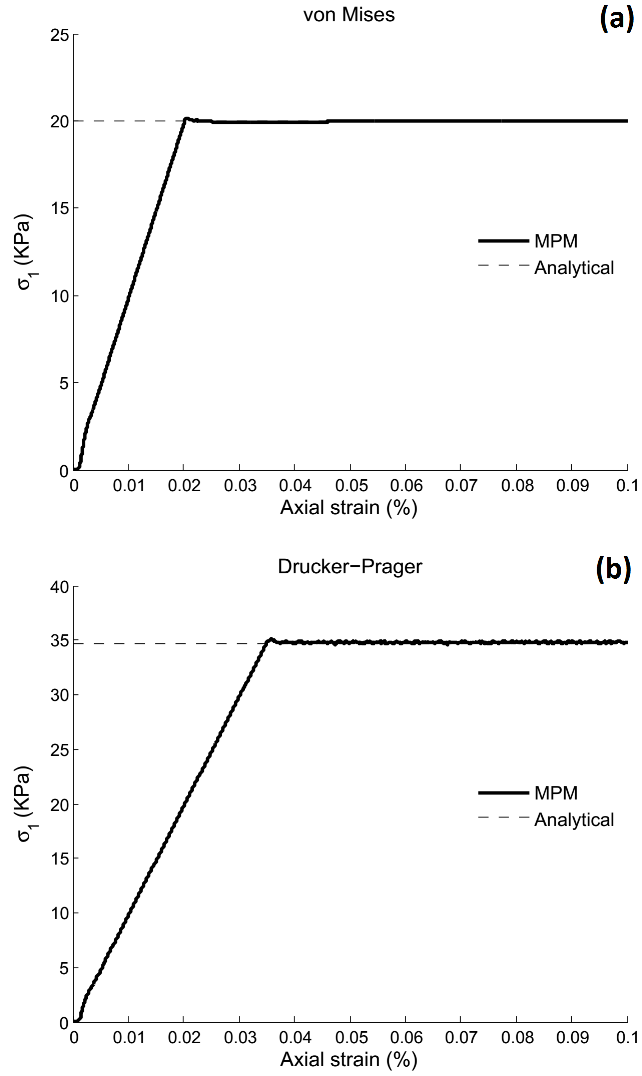

Figure 5.2: Stress-strain response for the UCS test for both von Mises (a) and Drucker-Prager (b) models.

Large deformation of an elastic cylinder

In order to demonstrate the capability of the presented large deformation formulation and the mixed integration technique involving the crossing of particles over several elements, an example with excessive deformation is considered, in which an elastic cylinder is allowed to deform subjected to its body force. The problem can be simulated using an axisymmetric configuration.

Figure 5.4 shows the geometry and boundary conditions. The same model is also simulated using the ABAQUS FEM code.

Figure 5.4 shows the contours of total displacements with both MPM and ABAQUS. The displacements of two target points, A and B, are also depicted in Figure 5.5. Considering the excessive deformation of the solid body and the crossing of several particles over various elements, the MPM formulation can still provide accurate numerical results comparable with the FEM solution.

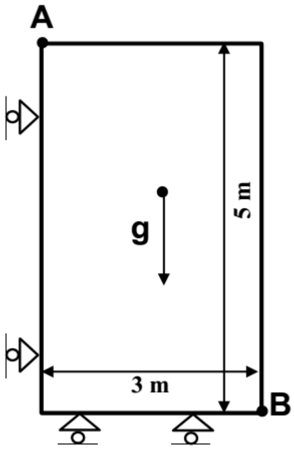

Figure 5.3: Geometry and boundary conditions of an elastic cylinder undergoing large deformations.

Table 5.2: Material properties for the elastic cylinder

Parameter	Unit	Value
Young's modulus, E	(kPa)	1×10^2
Poisson's ratio, ν	-	0.3
Density	(kg/m^3)	1500
Gravity	(m/s^2)	10

Footing penetration

The final validation example consists of a classical footing problem. This example involves large strain by allowing the footing to penetrate into the soil mass. The footing is considered as a rigid and axisymmetric resting on a von Mises soil and a no friction condition is applied at the interface between the soil and the footing. The mechanical properties of the soil are the same as those used in the previous uniaxial compression test (see Table 5.2). A prescribed displacement is applied on the footing in order to impose a rigid behaviour. The geometry and boundary conditions for this example are shown in Figure 5.6.

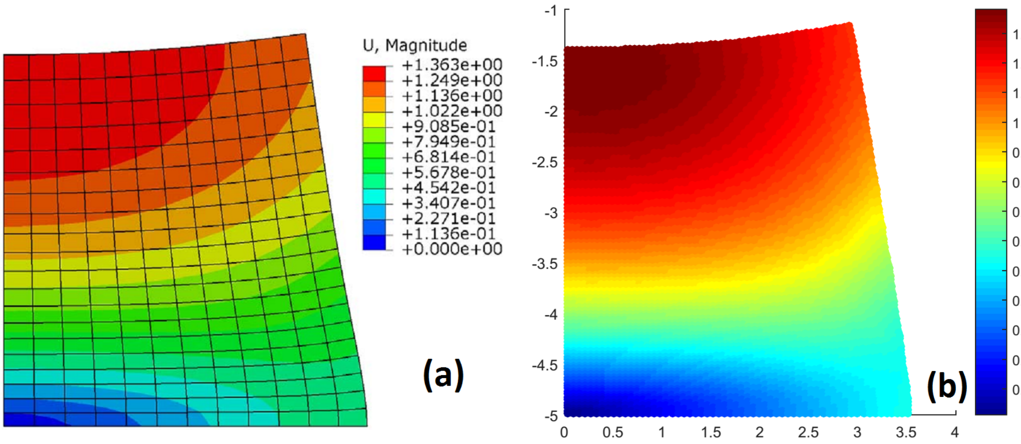

Figure 5.4: Contours of total displacements obtained with both ABAQUS (a) and MPM (b) on deformed configurations.

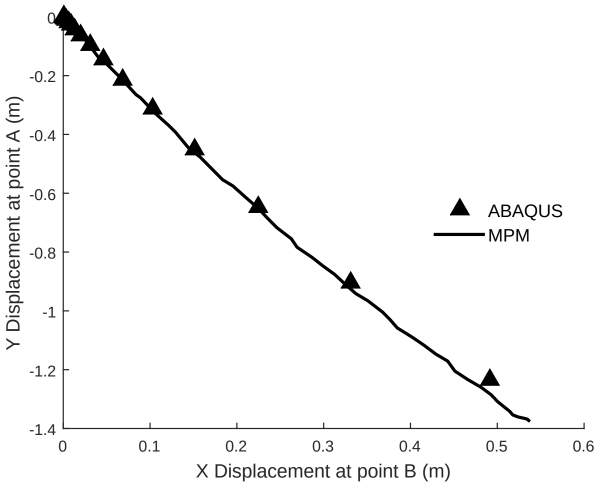

Figure 5.5: Vertical displacement versus horizontal displacement at two points A and B obtained with both MPM and ABAQUS.

The radius of the footing is 3 m; therefore, in order to be able to accurately capture the failure mechanism, the elements beneath the footing are considered to have a mesh size of 0.5 m. The excessive deformation in the soil tends to take place in the vicinity of the footing in the form of vertical compaction and horizontal extension. A higher particle density (16 particles per element) around the footing avoids a non-physical gap in the continuum body. Far from the footing, as the deformations are infinitesimal, only one particle per element is required to describe the strain field. This gradual refinement can significantly reduce the total number of material points and consequently reduce the overall computational cost. Figure 5.7 shows the mesh size and particle density used in the model.

A known difficulty arising in explicit solvers for quasi-static problems is noise or vibration

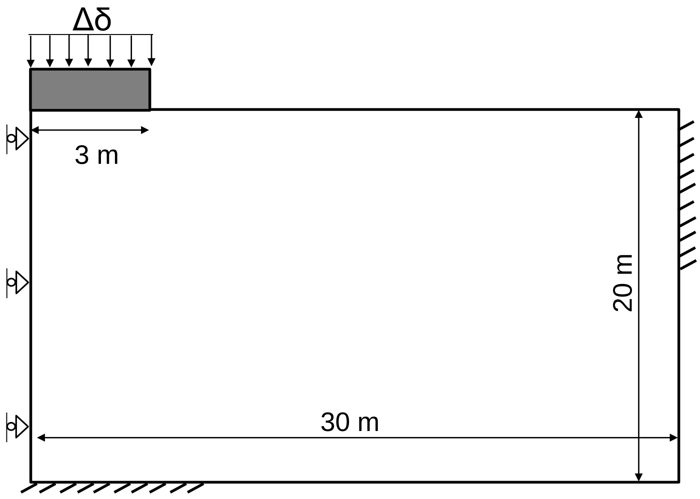

Figure 5.6: Geometry and boundary conditions of the circular footing problem.

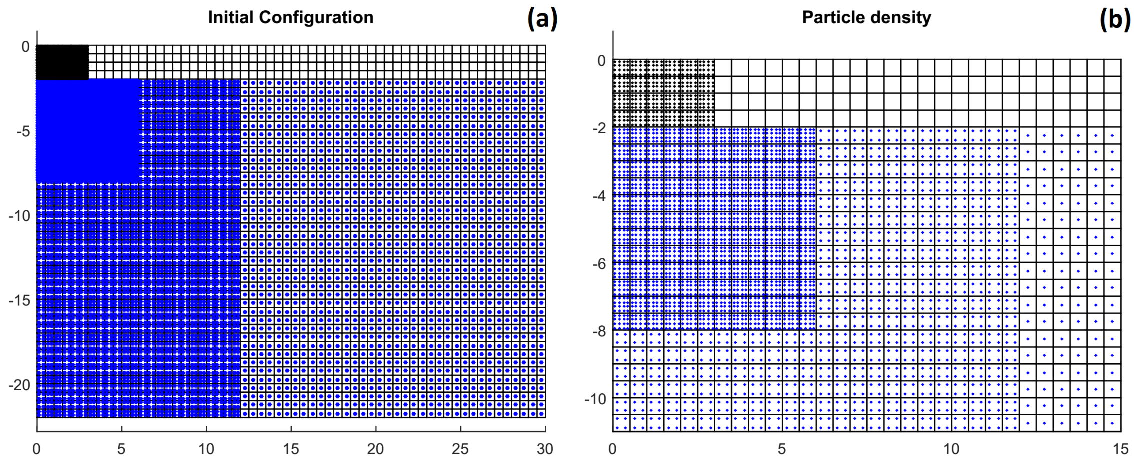

Figure 5.7: Initial mesh (a) and particle densities (b) around the footing for the circular footing problem. (three densities of 16, 4 and 1 material points per elements are used).

(Ma and Randolph, 2014). The source of the noise is the high inertia of the system, which cannot be adequately damped. In order to tackle this problem, some efficient numerical treatments are considered in this study. First, the use of a prescribed displacement (i.e. prescribed velocity in an explicit scheme), produces much lower noise than a prescribed loading. Second, through sensitivity analysis, it was observed that higher values of damping coefficient (see Appendix B), around 0.8 - 0.9, can significantly reduce the oscillation in the numerical system. However, using a high value of damping increases the time that is required for the applied load or displacement to propagate in the medium. This means a higher number of iterations is essential. Third, the contact force is normally calculated directly from the contact elements. In the MPM formulation, this can be achieved by extracting the internal forces of the contact nodes. However, if the soil weight is ignored, the contact force can be obtained from the vertical reaction force at the boundaries. Since the noise at the contact surface dissipates by damping when it reaches the boundary, the results will be smoother when the vertical reaction force at boundaries is used, instead of the normal contact force.

This example is also simulated using ABAQUS with the exact geometry and mesh density used in MPM. Loading is performed by imposing a prescribed displacement on the footing. The bearing capacity versus displacement of the footing is shown in Figure 5.8. As it can be seen, the MPM results are in good agreement with the FEM analysis. However, the simulation with the FEM is terminated after 0.75 m of penetration due to the excessive mesh distortion around the edge of the footing. Figure 5.9 shows the contours of horizontal and vertical displacements around the footing. In addition, the displacements at different nodes situated at the soil/footing interface are compared with each other to demonstrate the performance and accuracy of the prescribed displacement boundary condition. It was noted that the maximum difference in both vertical and horizontal movements of the material points at the footing interface is less than 0.02 %, which can be considered as infinitesimal and confirms the semi-rigid movement of the footing obtained using the implemented kinematic boundary condition.

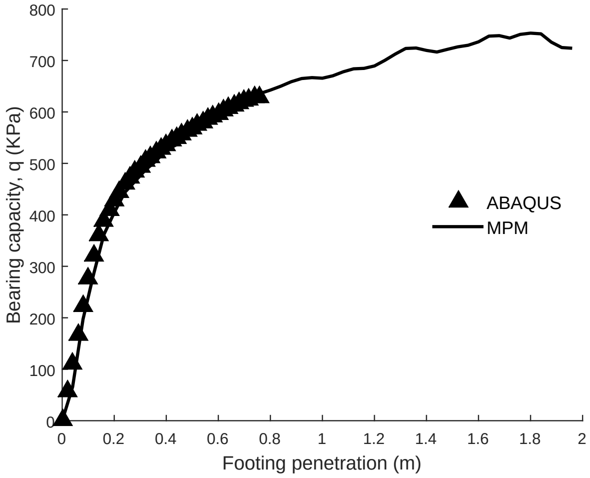

Figure 5.8: Bearing capacity versus footing penetration with both MPM and ABAQUS.

5.3 Sample description and indentation tests

Three Posidonia shale samples with quite different mineralogical compositions and consequently mechanical responses, were selected for this study. The samples, namely Wic-29, Har-46 and Had-27, were comprehensively characterised in Chapter 3 in terms of porosity,

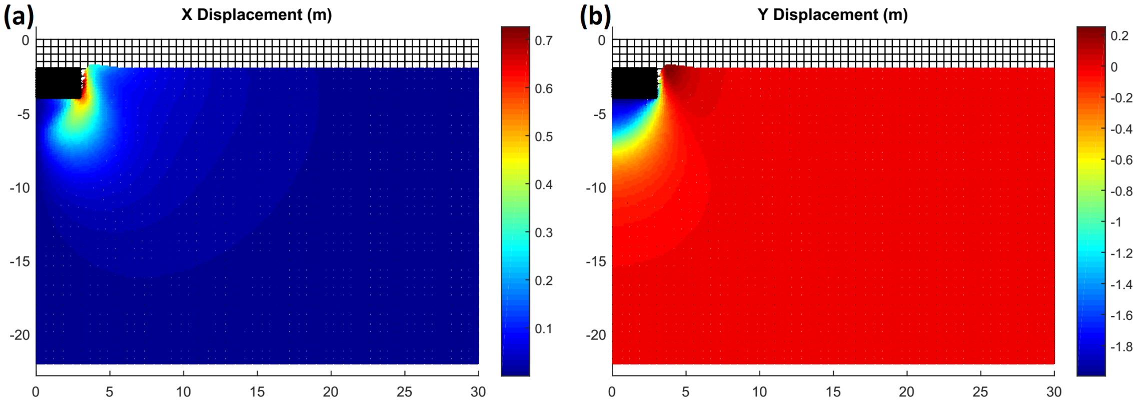

Figure 5.9: The contours of horizontal (a) and vertical (b) displacements after 2 m of penetration.

organic carbon content and silt mineral inclusions. Indentation testing was then conducted on well-polished sections prepared perpendicular to bedding direction. Two different indenters, Berkovich and spherical, were considered to generate different stress-strain paths in the samples, in order to provide the opportunity to determine as accurately as possible the two unknown plasticity material parameters (cohesion and internal friction angle). All the tests were conducted with a maximum force of 500 mN, 120 s holding time at the maximum load and 49 indents per section. The radius of the spherical indenter was 25 μm.

In order to conduct the inverse analysis, it is required to generate an average load-displacement curve to represent each set of indentation tests. As the maximum load is constant in all the indentation tests, two average maximum displacements are determined at the end of loading curves and at the beginning of unloading curves. Then, the average loading and unloading curves are derived using the Least-Squares Polynomial Approximation. The scope of this study is limited to the back-calculation of strength parameters, therefore, the mean load-displacement curves are corrected with respect to the time-dependent response. The loading-unloading stage was 50 s, which is relatively low compared to the holding time of 120 s at the maximum load. The effect of creep in these two stages is ignored and the unloading curve was shifted by the average creep displacement at the maximum load.

Figure 5.10 shows the mean load-displacement curves and Table 5.3 provides the mean values of the indentation moduli (reduced Young's moduli, E*), maximum penetration depths (h$_{max}$), and estimated maximum contact areas (A$_c$) for these samples. The contact areas provided in this table were estimated by calculating the contact surface on the indenter's geometry from the penetration depth, without considering any pile-up or sink-in effect around the indenter.

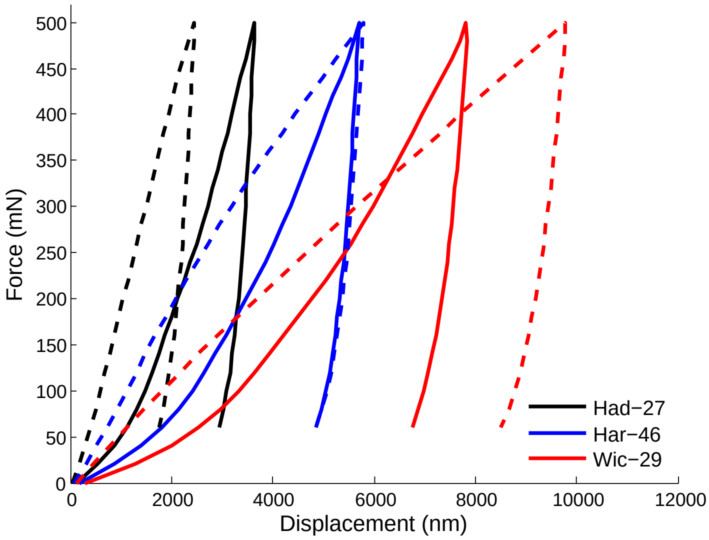

Figure 5.10: Mean load-displacement curves for both Berkovich (solid lines) and spherical (dashed lines) indenters.

Table 5.3: Different characteristics obtained from the mean load-displacement curves.

Parameter	Wic-29		Har-46		Had-27	
Indenter	Spherical	Berkovic	Spherical	Berkovic	Spherical	Berkovic
E^* (GPa)	14.0	14.0	26.9	25.1	47.3	51.3
h_{max} (μm)	9.77	7.81	5.80	5.70	2.45	3.64
A_c (μm^2)	1234.8	1496.8	805.38	769.72	365.98	324.61

It is worth noting that the author's experience showed that there is local variability in the mechanical properties of shale due its high level of inhomogeneity. Therefore, the exact value of the reduced elastic moduli obtained from each set of tests are used, which may be slightly different for each indenter and also from the values provided in Chapter 3. In addition, the relative difference in the load-displacement curves obtained using the Berkovich and spherical indenters depends on the penetration depth. It can be observed that for sample Had-27, the spherical indenter penetrates less into the surface of the sample than the Berkovich indenter; however, for sample Wic-29, which is considered to be much softer than the Had-27 sample, the spherical indenter penetrates into the sample surface more than the Berkovich indenter. This observation can be explained by the shape of the spherical indenter, for which the contact surface inclination is continuously increasing with the consequence of allowing the sample surface to slip easily along the contact area. The Berkovich indenter, on the other hand, has a constant contact inclination, which makes its response more consistent at different penetration depths.

5.4 Inverse analysis of indentation test

5.4.1 Nonuniqueness of a single indentation load-displacement curve

Material response beneath the indenter, which is sensed as the reaction force, is a function of the elastoplastic behaviour of the material and the shape of the contact surface (Magnenet *et al.*, 2008; Guo *et al.*, 2010). Tho *et al.* (2004) studied conical indenters and showed that a load-displacement curve can only be representative of two unique independent material parameters. As a result, when the elastoplastic response of a material is described by more than two parameters, a single load-displacement curve, for a given indenter shape, can be predicted by several combinations of material properties. In the case of shale rocks, the simplest way to describe the elastoplastic response could be an isotropic elastic behaviour in conjunction with a pressure sensitive constitutive model. Such a model can be described by a Young's modulus, a Poisson's ratio, a cohesion and an angle of internal friction. Assuming a suitable value for Poisson's ratio, the three remaining material parameters have to be determined to define the mechanical response of a shale sample. This results in non-unique indentation responses of shale rocks.

In order to better demonstrate this problem, indentation tests with both Berkovich and spherical indenters on two different materials, with pressure sensitive ($\phi > 0$) and von Mises ($\phi = 0$) plastic responses are simulated. Table 5.4 provides the material properties used for these simulations. The spherical (Spher.) indenter has an axisymmetric shape, however, the Berkovich indenter is a uniform three-sided pyramid. It was shown that the three dimensional geometry of a Berkovich indenter can be resembled by a conical indenter with apex angle of 70.3 degree (Dao *et al.*, 2001; Bucaille *et al.*, 2003). These two geometries produce identical projected areas for any given penetration depth. A similar approach is considered in this study in order to be able to use the axisymmetric formulation for the Berkovich indenter.

Table 5.4: A von Mises (Material 1) and a pressure-sensitive (Material 2) material properties with identical indentation results using the Berkovich indenter.

Parameter	Unit	Material 1	Material 2
Young's modulus, E	(kPa)	1×10^4	1×10^4
Poisson's ratio, ν	-	0.3	0.3
Friction angle, ϕ	(^{o})	0	20
Cohesion, C	(kPa)	100	40

Two key parameters involved in the modelling of the indentation test having potentially noticeable effects on numerical results, are the size of the model and the mesh refinement around the contact area. The size of the model should be large enough in such way that the results are insensitive to the boundary conditions. In addition, as the contact area is continuously changing, the finer the mesh is, the more accurately the contact surface can be captured. There is no clear rule of thumb for the plastic material parameters, and it is recommended that a sensitivity analysis is undertaken in order to determine suitable values for each particular problem. Figure 5.11 illustrates the axisymmetric geometry and boundary conditions for the simulation of indentation tests. The MPM models and particle densities per elements are provided in Figure 5.12 and 5.13. Higher particle densities of 16 and 4 particles per element are used around the contact surface in order to account for the excessive distortion around this area and to accurately calculate the contact normal vectors.

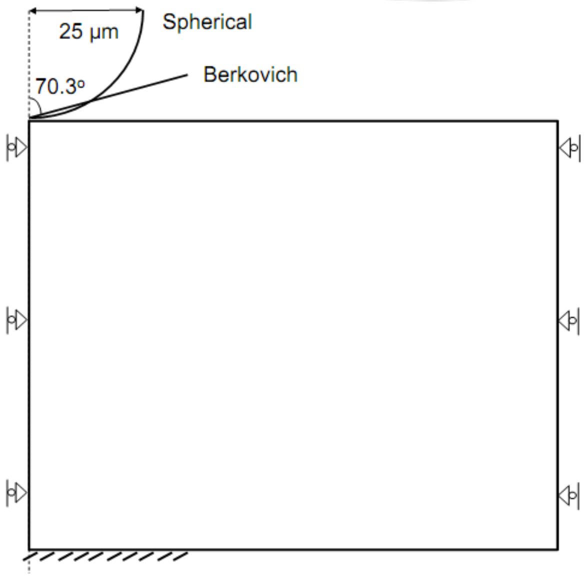

Figure 5.11: Geometry and boundary conditions used in the simulation of indentation tests.

Figure 5.14 shows two load-displacement curves obtained with the same elastic moduli and different plasticity parameters using the Berkovich indenter. It can be observed that both the von Mises and the pressure-sensitive models produced identical indentation load-displacement curves. In fact, there are infinite combinations of cohesion and angle of internal friction, that are able to produce the same curve. The extent of the plastic zone beneath the indenter revealed that the stress-strain paths for the tested samples are not identical in the two simulations (Figure 5.15). It should be noted that the observed slight oscillations in the load-displacement curves is expected due to the explicit nature of the MPM formulation.

Bucaille *et al.* (2003) attempted to back-calculate the hardening parameters of a von Mises

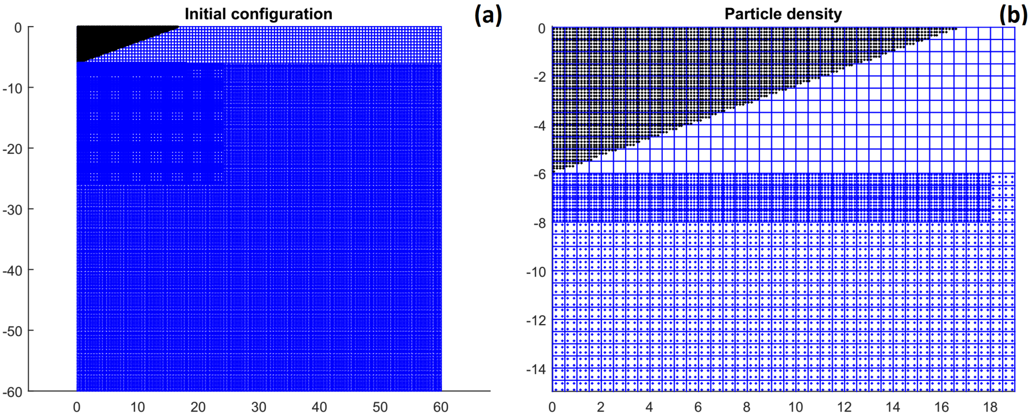

Figure 5.12: (a) initial configuration and (b) particle densities for the indentation test with the Berkovich indenter.

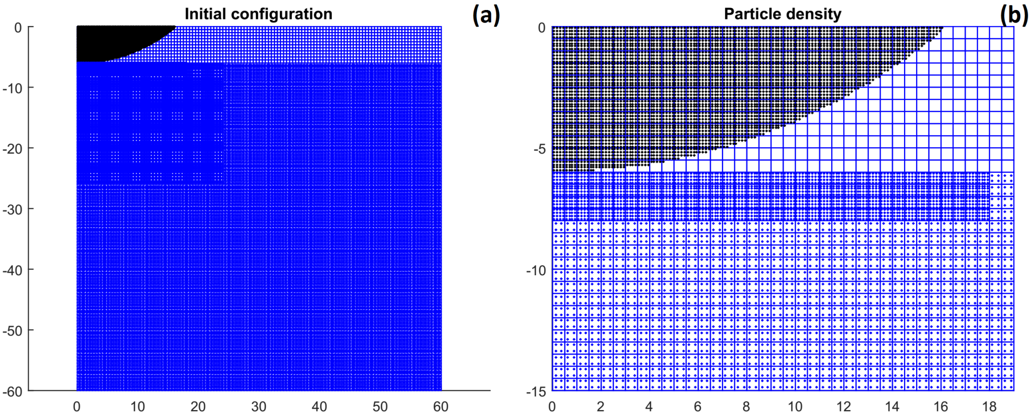

Figure 5.13: (a) initial configuration and (b) particle densities for indentation test with the spherical indenter. 16 particles per element and 4 particles per element.

model for metal plasticity. They have concluded that using two load-displacement curves, obtained by two different indenters, allows for the exact calibration of the plastic parameters. A similar approach was adopted and successfully applied to pressure-sensitive polymers by Seltzer *et al.* (2011). Figure 5.16 shows the load-displacement curves for the same materials (presented at Table 5.4) with the spherical indenter. As it can be observed, two sets of material properties for which the indentation results are matched with the Berkovich indenter, do not produce identical indentation curves with the spherical indenter.

Alternatively, two sets of properties, presented in Table 5.5), produce identical results of indentation test using a spherical indenter. However, different responses are observed when the test is carried out using a Berkovich indenter (see Figure 5.17). Again, the plastic zones beneath the spherical indenter are completely different while the load-displacement responses from the

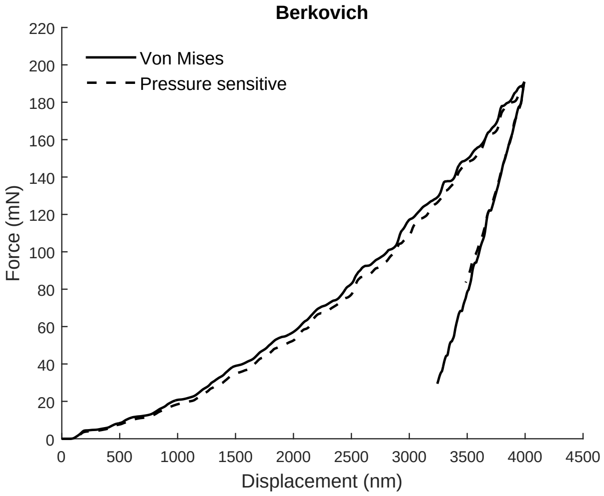

Figure 5.14: The load-displacement curves for both von Mises and pressure sensitive materials with Berkovich indenter.

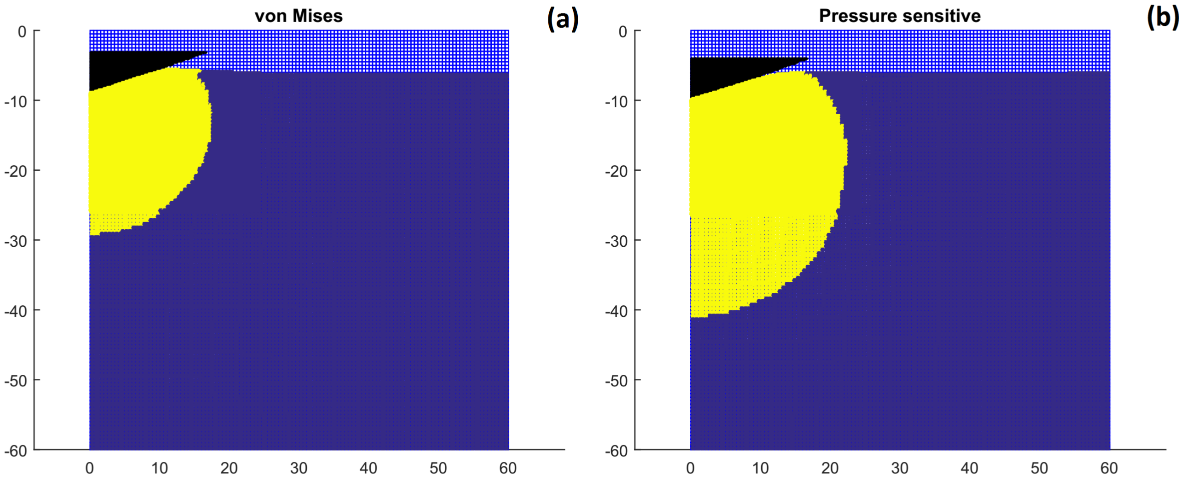

Figure 5.15: Plastic zone developed around the Berkovich indenter for both a von Mises (a) and pressure- sensitive (b) materials with identical indentation load-displacement curves.

test are identical (Figure 5.18). This fact will be used in the next section to determine the unique set of cohesion and angle of internal friction for the shale samples, using indentation tests.

Table 5.5: A von Mises (Material 1) and a pressure-sensitive (Material 2) material properties with identical indentation results using the spherical indenter.

Parameter	Unit	Material 1	Material 2
Young's modulus, E	(kPa)	1E4	1E4
Poisson's ratio, ν		0.3	0.3
Friction angle, ϕ	(^{o})	0	20
Cohesion, C	(kPa)	100	36

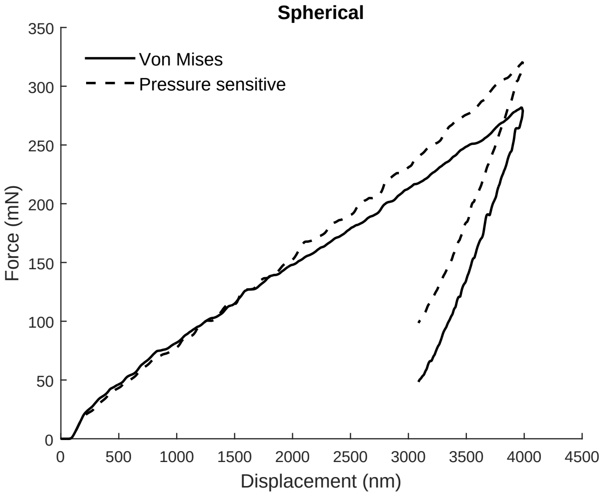

Figure 5.16: Load-displacement curves for a von Mises material and a pressure-sensitive material models obtained with a spherical indenter.

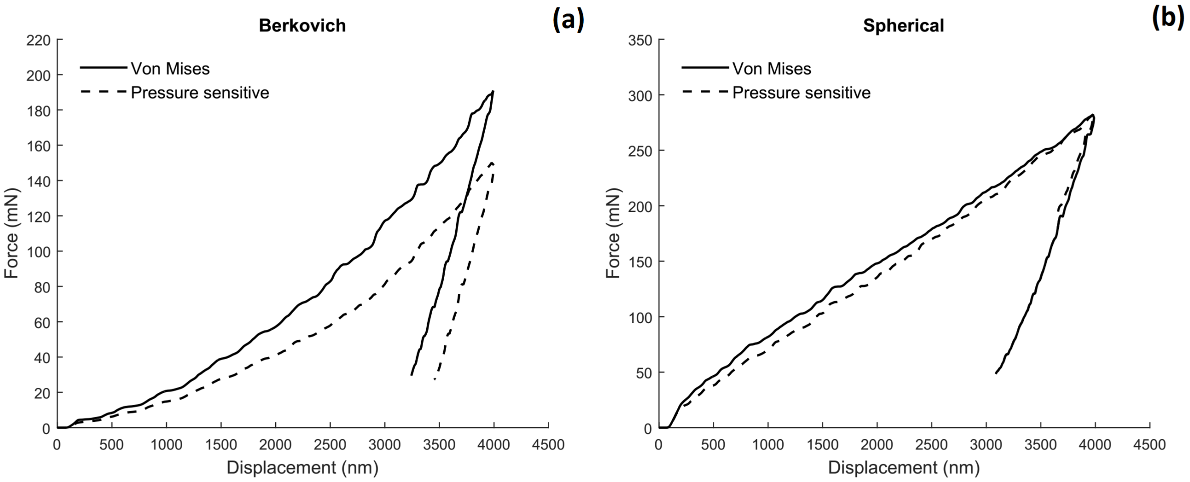

Figure 5.17: Load-displacement curves obtained with the Berkovich (a) and the spherical (b) indenters for a von Mises material and a pressure-sensitive material.

5.4.2 Inverse analysis of indentation test on organic-rich shale

Three shale samples, described in Section 5.3, are now considered for inverse analysis, in order to determine their respective plastic parameters. As only two different indenters were used, only two unknowns should be considered. A Poisson's ratio of 0.3 is assumed, in order to calculate Young's modulus from the reduced modulus obtained directly from the unloading curve. In addition, no frictional contact (μ) was initially considered between the indenters and the shale samples. Having made these assumptions, the only remaining unknowns in the inverse analysis are cohesion and angle of internal friction.

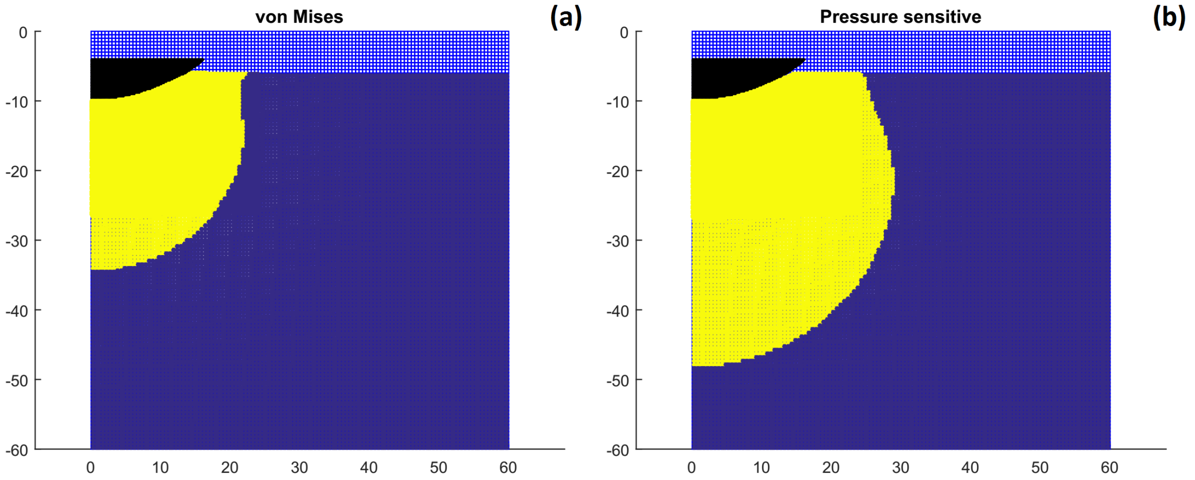

Figure 5.18: Plastic zone around spherical indenter for both a von Mises (a) and a pressure sensitive (b) materials with identical indentation load-displacement curves.

The mesh density and boundary conditions for the models are similar to those presented in Figures 5.11, 5.12 and 5.13. The author's experience showed that the size of the model should be at least 10 times larger than the penetration depth, in order to avoid any noticeable boundary effects on the final results. The experimental elastic moduli presented in Table 5.3 are used in the simulations. For each sample, a set of cohesion and angle of internal friction has been calibrated by matching the experimental load-displacement curves, using both the Berkovich and the spherical indenters. The numerical predictions of load-displacement curves are smoothed and compared with averaged experimental indentation measurements.

Figure 5.19 shows a comparison of the observed load-displacement curves and the calculated responses from the MPM analysis, for the sample Had-27. Table 5.6 also provides the back-calculated properties corresponding to these curves. It should be noted that the Uniaxial Compression Strength is calculated according to Eq. 5.3. As it can be seen, the set of plastic parameters which could best fit both sets of indentation tests, shows that the sample response is not sensitive to pressure. This may seem to be in contradiction with the experimental data which shows rocks possess pressure-sensitive properties (Ewy *et al.*, 2010; Rybacki *et al.*, 2015).

Table 5.6: The input and the final calibrated parameters of the indentation tests on sample Had-27.

Known parameters			Calibrated parameters		
E (GPa)	ν	μ	ϕ (^{o})	C (MPa)	UCS (MPa)
Berkovich 46.8 Spherical 43.1	0.3	0	0	285	570

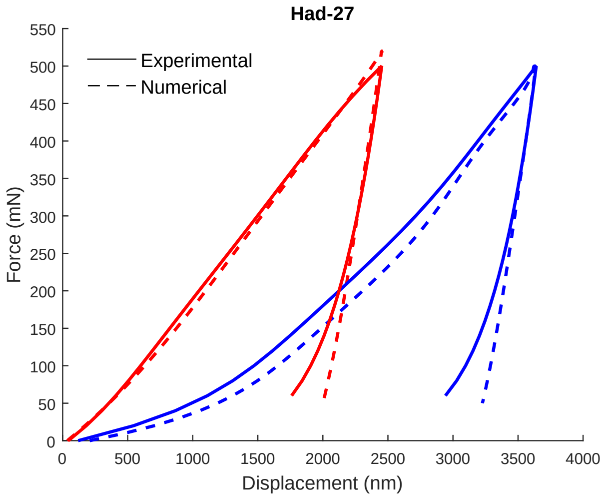

Figure 5.19: The experimental and the calibrated numerical load-displacement curves for both Berkovich (blue) and spherical (red) indenters.

In order to shed some light on this behaviour, it is worthwhile considering more advanced rock constitutive models. Conventional pressure-sensitive models such as the Drucker-Prager or the Mohr-Coulomb model assume that both angle of internal friction and cohesion are mobilised simultaneously and contribute to rock strength at the same time. This assumption may be correct when the confining pressure is high enough that rock behaviour can be assumed as ductile (Rojat *et al.*, 2009; Esterhuizen *et al.*, 2011). Diederichs *et al.* (2000) concluded that initially the cohesion is the main contributor to rock strength and as the induced damage increases, the cohesion reduces and the contribution of frictional component in the rock strength increases. Following these studies, Hajiabdolmajid *et al.* (2002, 2003) proposed an advanced Mohr-Coulomb based model called Cohesion Weakening Friction Strengthening (CWFS). In this model, both cohesion and angle of internal friction of rocks are functions of the plastic shear strain and the cohesion reduces gradually while the angle of internal friction increases as plastic shear straining occurs. Diederichs (2007) also developed a so-called composite constitutive model in which the cohesion is the major contributor at peak strength and, after a sufficient level of induced damage, the angle of internal friction will be the dominant parameter at the residual strength. Considering the studies mentioned above along with the results obtained in this work using the inverse analysis of the indentation tests, it can be concluded that when the indentation test is conducted under the described details, the two mechanisms (cohesion and friction) contributing in rock strength cannot be activated at the same time. In other words, the frictional component was not mobilised beneath the indenter at the same time as the cohesion.

Comparing UCS for the Had-27 sample with the available data from literature (see Table

5.7), it can be seen that the back-calculated value for this sample is relatively high. This result might be due to the well-known problem of scale effect in rocks. In the field of rock mechanics, it is well-established that the mechanical strength of rock is reduced when the size of the tested specimen is increased. This phenomenon can be observed at both core scale and large scale rock mass until the sample size reaches its representative volume element (RVE), where the UCS is converges to a specific value (Bieniawski, 1968; Hustruild, 1976; Hoek and Brown, 1980; Jackson and Lau, 1990; Thuro *et al.*, 2001; Liang *et al.*, 2011). For instance, Zhang *et al.* (2011) provided an extensive UCS data for various sample sizes and showed that for intact rock samples, the reduction in strength as the sample size is increased can be up to 400%. This phenomenon can be explained by the presence of micro fractures and defects in the microstructure of rocks, which control the failure mechanism. The size of the sample must be large enough to account for all these features in order to produce a failure mode independent of the sample volume. Based on these studies, and the high value of UCS observed in the indentation test, it can be concluded that although the shale sample has a very fine microstructure, compared to other rocks, the area affected by the indentation test is not large enough to be a RVE for the elastoplastic behaviour of the shale sample.

Table 5.7: The UCS data obtained from core scale samples for different shales.

Sample Sample	E (GPa)	ν –	UCS (MPa)	Source
Asan gneiss	68.3	0.3	223.2	Cho *et al.* (2012)
Boryeong shale	39.3	0.18	126.2	
Yeoncheon schist	72.1	0.25	124.7	
Alum shale	29	—	83.8	Rybacki *et al.* (2015)
Alum shale	11	—	41.4	
Barnett shale	25	—	105.5	
Barnett shale	18.9	—	73	
Barnett shale	12	—	35.7	
Wickensen shale	10.3	—	114.8	
Wickensen shale	4.1	—	87.4	
Dotternhausen shale	9.4	—	70.9	
Posidonia Shale	17.3	—	75	Meier *et al.* (2013)
Posidonia Shale	9.4	—	67	

Similarly, the load-displacement curves are fitted for the Har-46 sample. This sample is much softer than the previous one (Har-27), therefore the maximum penetration depth is higher under the same maximum load. Figure 5.20 shows a comparison of the observed and the simulated load-displacement curves for this sample. The values of the input and calibrated parameters used in the indentation simulations are listed in Table 5.8. It can be observed that this shale sample shows very low pressure-sensitivity and its response is still strongly dominated by the cohesive component. This is in agreement with the results obtain for the Had-27 sample. More penetration in this sample, which is because of its lower stiffness, allows for a slight mobilisation of the frictional component. Again, the UCS value is high compared to the available experimental data (Table 5.7). This means that the contact area is still not large enough to affect the RVE of this sample.

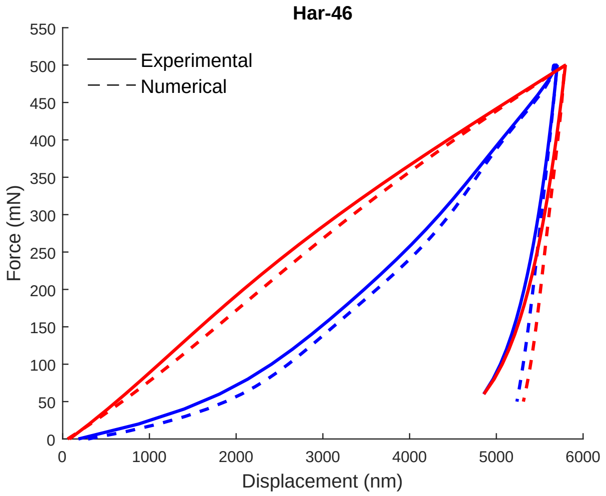

Figure 5.20: The experimental and the calibrated numerical load-displacement curves for both Berkovich (blue) and spherical (red) indenters.

Table 5.8: The input and the final calibrated parameters of the indentation tests on sample Har-46.

Known parameters			Calibrated parameters		
E (GPa)	ν –	μ –	ϕ (^{o})	C (MPa)	UCS (MPa)
Berkovich: 24.480 Spherical: 22.841	0.3	0	6.4	78.25	175

The last sample, Wic-29, is much softer than the previous ones, due to both its higher porosity and organic matter content. As mentioned in Section 5.3, due to the curvature of spherical indenters, the obtained load-displacement curve is more sensitive to the penetration depth in comparison with the curve of Berkovich indenter. The calibration process was started with load-displacement curve of Berkovich indenter since the contact inclination is not sensitive to the penetration depth. For this sample, a response described by a von Mises model (only cohesive) with a cohesion of 104.75 MPa matches well the results of the Berkovich indenter. However, the peak force produced using the same material properties for the spherical indenter is around 361 mN , which is much lower than the maximum load of 500 mN, applied in the experiment. By adopting a pressure-sensitive model, better results are obtained for both indenters. It was observed that when the internal angle of friction for the pressure-sensitive set of properties is increased, the obtained peak load for the spherical indenter increases; however, even when a cohesionless property was calibrated for the Berkovich test, it cannot still reproduce the experimental curve of the spherical indenter. Figure 5.21 provides several trial load-displacement curves for sample Wic-29.

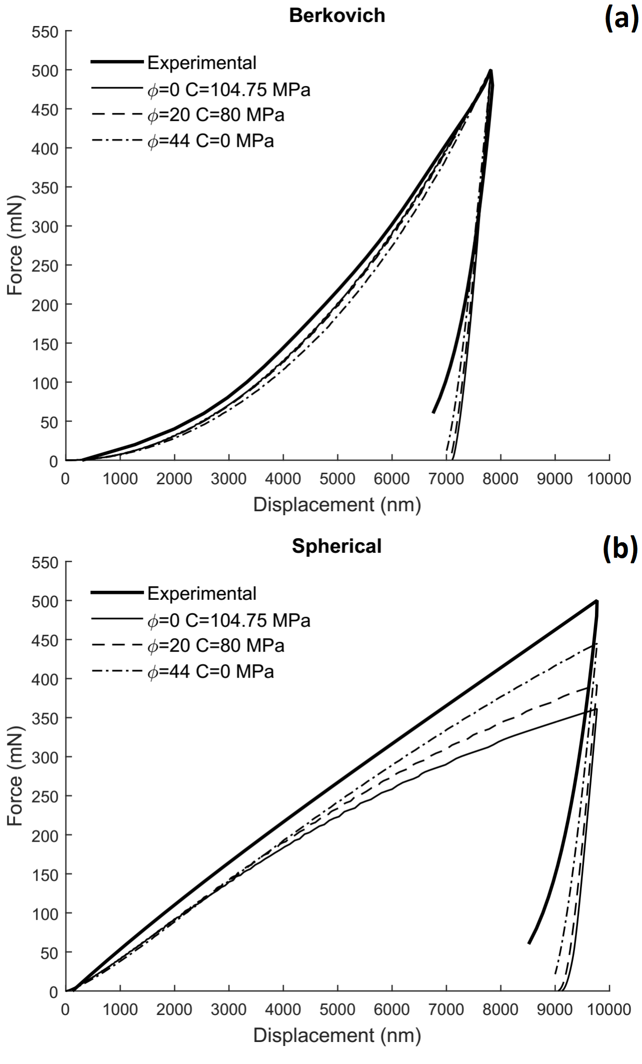

Figure 5.21: The experimental and the different calibrated numerical load-displacement curves of Berkovich (a) and spherical (b) indenters for sample Wic-29.

Based on the spherical indenter results presented in Figure 5.21, it can be said that for this particular sample, the numerical results are not in good agreement with the experiment. This difference can be attributed to the assumption being made about the contact property. The vertical force being sensed by the indenter has contributions from both normal and tangential forces acting on the contact surface. Assuming a frictionless contact properties, results in no tangential contact force, which consequently ignores its contribution to the total vertical load applied on the indenter. Given the higher penetration depth in this sample, part of the contact surface for the spherical indenter is noticeably steep. In this part of the contact, the contribution of the tangential force in the total vertical force is significant, which is being ignored in the modelling. It should be noted that the numerical simulations showed that the load-displacement of the Berkovich indenter is not highly sensitive to the frictional contact (Sarris and Constantinides, 2013).

There is no study in the literature which provides a good estimation on the friction coefficient between the indenter and a shale sample. The roughness of the surface for the tested shale samples in this work was evaluated in Chapter 2, and found in the order of 100 nm. This value is not comparable to the roughness normally measured on polymers and metal samples which is usually around a few nano meters (see the AFM test results for standard HOPG-12M sample in Chapter 2). Given the fact that the main component of shale is clay, there may even be an adhesion force acting between the clay and the indenter.

Several studies attempted to investigate the friction and adhesion between clay and a steel/glass surface (Littleton, 1976; Lemos and Vaughan, 2000; Basmenj *et al.*, 2016). They reported a friction coefficient of 0.2 to 0.35 for the contact between a smooth glass and a low plasticity clay. Two values of 0.2 and 0.3 are considered in the simulations of indentation test, carried out on the Wic-29 sample. In addition, the previous simulations are also repeated with a frictional contact. The experimental curves for the Had-27 and Har-46 samples cannot be produced using the contact friction of 0.3. Therefore, a value around 0.2 should be more realistic in this case. Figure 5.22 shows the new calibrated load-displacement curves for sample Wic-29 with frictional contact. It can be seen that both tests can be well matched by considering a friction coefficient for the contact surface. The significant change observed when a contact friction is added, reveals the importance of this parameter. Table 5.9 provides the new calibration parameters for all the samples. It can be concluded that the effect of friction on sample Had-27 and Har-46 is much lower which shows that increase in the penetration depth enhances the effect of contact friction. Therefore, it is critical to pay attention to the indentation depth and avoid excessive penetration, with respect to the tip radius for the spherical indenter. For instance, in a study by Seltzer *et al.* (2011), in which a spherical tip was successfully adopted to study the elastic response of pressure-sensitive polymers, the maximum ratio of penetration depth to the tip radius is 0.1, while for sample Wic-29, it is almost 0.36.

Another issue revealed from the results obtained for sample Wic-29 (Table 5.7) is that the resulted UCS value from the calibrated parameters is completely within the range of UCS for soft shale core samples, reported in the literature. In fact, this can be considered as a promising result for the possibility of using indentation tests for the elastoplastic characterisation of shale samples, provided that sufficient level of load is applied. Clearly, further study and comparison of material parameters obtained by indentation tests with core sample data are essential to approve this hypothesis.

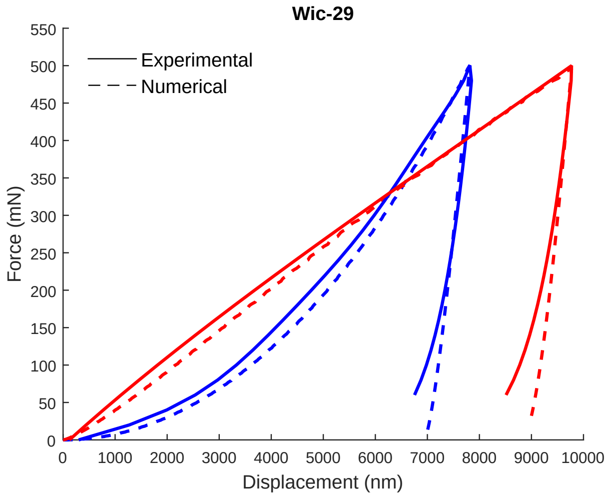

Figure 5.22: The experimental and the calibrated numerical load-displacement curves with a contact friction of 0.2 for both Berkovich (blue) and spherical (red) indenters.

Table 5.9: The input and the final calibrated parameters of the indentation test on all the samples with frictional contact.

sample	Known parameters			Calibrated parameters		
	E (GPa)	ν	μ	ϕ	C (MPa)	UCS (MPa)
Had-27	Berk. 46.865 Spher. 43.043	0.3	0.2	0	293	586
Har-46	Berk. 24.480 Spher. 22.841	0.3	0.2	0	105.5	211
Wic-29	Berk. 12.74 Spher. 12.74	0.3	0.2	18.27	21	58
Wic-29	Berk. 12.74 Spher. 12.74	0.3	0.3	15.3	25.2	66

By comparing the numerical and the experimental results at the unloading stage, it can be understood that these results are only matched at the beginning of this stage. In fact, the experimental unloading curve is concave, which can be interpreted as a gradual reduction in the elastic stiffness. However, the assumption of linear elasticity in the modelling produces a straight unloading path. An explanation could be suggested based on the time-dependent response of shale samples. Comparing unloading curves for two different samples with a large difference in their stiffness and time-dependent response (see Chapter 3) in Figure 5.19 and 5.22, it can be observed that this nonlinear response is quite noticeable in both samples. Therefore, the creep phenomenon may not be the influential factor that contributes to this nonlinear unloading curve. The cyclic behaviour of rocks and concrete have been investigated through several loading/unloading steps before and after their peak failure point (Aslani and Jowkarmeimandi, 2012; Liang *et al.*, 2012; Yang *et al.*, 2015). Figure 5.23 shows the stress-strain path for cyclic uniaxial compression tests on sandstone and concrete samples. As it can be seen, the unloading curves in these samples showed the same nonlinear behaviour. Sima *et al.* (2008) explained this response by the presence of damage and microcracks in concrete samples. The loading and reloading stages cause closing and opening of the microcracks, which results in different responses. The same explanation could be provided for indentation test on shales. That is why even in sample Had-27, which has a very low creep response, the unloading curve is concave. In fact, in the early stage of unloading, the damage fractures are still closed and the elastic response of the material beneath the indenter is still close to the intact sample. By continuing the unloading, the induced fractures are opened and consequently, the overall material stiffness reduces.

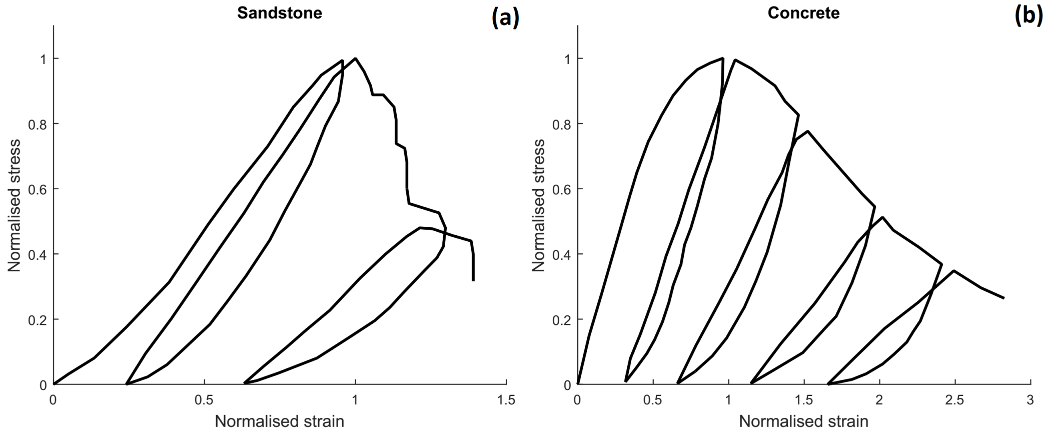

Figure 5.23: The stress-strain curves of cyclic loading on sandstone (a) and concrete (b) (stress and strain are normalised based on their values at the first peak strength) (Aslani and Jowkarmeimandi, 2012; Yang *et al.*, 2015).

5.5 Summary and conclusion

In this study, the possibility of using indentation testing in order to extract plasticity parameters of shales was investigated. Numerical simulation was used to conduct inverse analysis on the experimental data. As the indentation test involves contact, penetration and geometrical nonlinearity, the recently developed numerical technique known as the Material Point Method was adopted for this purpose.

The developed MPM code was initially validated through several examples. Both constitutive models and the large deformation formulation were assessed, against analytical solutions and ABAQUS, a commercial FEM package. Finally, the highly nonlinear problem of the penetration of a circular footing was simulated and compared with ABAQUS results. Very good agreements were observed in the validation examples. In addition, the capability of the MPM code was demonstrated against mesh-based methods by its unconditional stability subjected to excessive deformation.

Through several simulations, it was shown that for a shale-like material with pressure sensitive plastic behaviour, the load-displacement curve obtained by an indenter geometry can be reproduced with different combinations of internal friction angle and cohesion. In fact, there are infinite combinations of plastic parameters that can produce the same load-displacement curve. In order to mitigate this problem, a second indenter geometry was suggested. It was then illustrated that if two sets of properties produce identical indentation curve, their results would not be matched for an indentation test with another type of indenter. This was used as the basis to calibrate the unique set of plastic parameters of shale samples.

Inverse analysis of indentation test on shale samples was conducted by assuming only two material unknowns, internal angle of friction and cohesion. The reduced modulus was extracted from unloading curves and the values of Poisson's ratio and contact friction were assumed. In addition, no time dependent response was considered. Initially, the simulations were carried out by considering no friction in the contact. The calibration process was conducted simultaneously for both load-displacement curves, obtained from Berkovich and spherical indenters, for the three Posidonia shale samples. The sample Had-27 which shows a high elastic moduli (around 50 GPa), was calibrated as a cohesive material with a high value of the cohesive strength, compared to core scale data. The same issue was observed with sample Har-46, which is much softer than sample Had-27, with an elastic modulus of around 25 GPa, and showed a cohesive response, with slight mobilization of the friction angle. The final sample was a very soft shale with elastic modulus of around 14 GPa and high organic content. On this sample, the penetration depth increased significantly using the same maximum loading force. The load-displacement curve for the Berkovich indenter was fitted using two extreme cases of cohesive and cohesionless plastic behaviours. However, none of them could finally match with the curve of the spherical indenter. The main reason for this observation, is the effect of contact friction. Considering values of 0.2-0.3 based on several studies on the contact friction of clay and glass/steel, a set of pressure sensitive properties can be fitted to both experimental curves. Adopting the value of 0.2 for contact friction, slightly changed the quantitative results for sample Had-27 and Har-46, but the qualitative observations remained the same. However, a reasonable set of properties, comparable with the reported data in the literature were obtained on the soft sample of Wic-29.

The obtained results from numerical analysis of indentation tests are in agreement with well-established observations in the field of rock mechanics. For instance, it is well-understood that rock strength is highly scale dependent and under low confining pressure, hard rock behaviour is cohesive and the friction angle requires a certain level of damage to mobilise. Therefore, considering the cohesive and high strength behaviour of sample Had-27, it can be concluded that the indentation test on this sample cannot affect its representative volume element and the level of damage is not high enough to activate the internal friction angle. By increasing the penetration depth on sample Har-46 and consequently the deformation in the samples, the internal friction angle was slightly activated. On the other hand, on the softer sample of Wic-29, where the penetration depth was relatively high compared to the other samples, a reasonable set of values for cohesion and internal friction angle was calibrated; which gives a UCS value comparable with the reported data on core samples in the literature.

In general, the material point method was proven to be a very powerful tool for numerical simulation of problems involving penetration and large deformation, with no instability caused by geometrical non-linearity. In addition, it can be said that the inverse analyses of the indentation tests with maximum load of 500 mN on shale samples, with reduced elastic moduli of around 50 and 25 GPa were not successful for the evaluation of cohesion and internal friction angle. However, the back calculated values of cohesion, internal friction angle and the corresponding UCS for the sample with reduced elastic modulus of 14 GPa, are in the ranges being reported in the literature. The potential of the proposed approach for further characterisation of the strength parameters of shale rocks is clear but an increase in the load capacity of indentation machines also seems essential.

References

Abou-Chakra Guery A., Cormery F., Shao J.F., Kondo D. 2008a. A micromechanical model of elastoplastic and damage behavior of a cohesive geomaterial. *International Journal of Solids Structure*, **45**(5), 1406-1429.

Abou-Chakra Guery A., Cormery F., Shao J.F., Kondo D. 2008b. A micromechanical model for the elasto-viscoplastic and damage behavior of a cohesive geomaterial. Physics and Chemistry of the Earth, Parts A/B/C, **33**(1), S416-S421.

Andersen S., Andersen L. 2010. Analysis of spatial interpolation in the material-point method. *Computers and Structures*, **88**, 506-518.

Antunes J.M., Menezes L.F., Fernandes J.V. 2006. Three-dimensional numerical simulation of Vickers indentation tests. *International Journal of Solids and Structures*, **43**, 784-806.

Aslani F., Jowkarmeimandi R. 2012. Stress-strain model for concrete under cyclic loading. *Magazine of Concrete Research*, **64**(8), 673–685.

Bobko C., Ulm F.J. 2008 The nano-mechanical morphology of shale. *Mechanics of Material*, **40**, 318-337.

Bardenhagen S.G., Brackbill J.U., Sulsky D. 2000. The material-point method for granular materials. *Computer methods in applied mechanics and engineering*, **187**, 529-541.

Bardenhagen S.G., Guilkey J.E., Roessig K.M., Brackbill J.U., Witzel W.M., Foster J.C. 2001. An Improved contact algorithm for the material point method and application to stress propagation in granular material. *Computer Modeling in Engineering and Sciences*, **2**(4), 509-522.

Bardenhagen, SG., Kober, E.M. 2004. The generalized interpolation material point method. *Computer Modeling in Engineering and Sciences*, **5**(6), 477–495.

Barthelemy J.F., Dormieux L., 2004. A micromechanical approach to the strength criterion of Drucker-Prager materials reinforced by rigid inclusions. *International Journal for Numerical and Analytical Methods in Geomechanics*, **28**, 565–582.

Basmenj A.K., Ghafoori M., Cheshomi A., Azandariani Y.K. 2016. Adhesion of clay to metal surface; Normal and tangential measurement. *Geomechanics and Engineering*, **10**(2), 125-135.

Bieniawski Z.T. 1968. The effect of specimen size on compressive strength of coal. *International Journal of Rock Mechanics and Mining Sciences*, **5**, 325-335.

Bennett K.C., Berla L.A., Nix W.D., Borja R.I. 2015. Instrumented nanoindentation and 3D mechanistic modeling of a shale at multiple scales. *Acta Geotechnica*, **10**, 1-14.

Beuth L., Wieckowski Z., Vermeer P.A. 2011. Solution of quasi-static large-strain problems by the material point method. *International Journal for Numerical and Analytical Methods in Geomechanics*, **35**, 1451-1465.

Beuth, L. 2012. Formulation and application of a quasi-static Material Point Method. Ph.D. Thesis, University of Stuttgart.

Bucaille J.L., Stauss S., Felder E., Michler J. 2003. Determination of plastic properties of metals by instrumented indentation using different sharp indenters. *Acta Materialia*, **51**, 1663–1678.

Bui H.H., Fukagawa R., Sako K., Ohno S. 2008. Lagrangian meshfree particles method (SPH) for large deformation and failure flows of geomaterial using elastic–plastic soil constitutive model. *International Journal for Numerical and Analytical Methods in Geomechanics*, **32**, 1537–1570.

Bui H.H., Kodikara J.A, Pathegama R., Bouazza A., Haque A. 2013. Large deformation and post-failure simulations of segmental retaining walls using mesh-free method (SPH). Proceedings of the 18th International Conference on Soil Mechanics and Geotechnical Engineering, Paris, 687-690.

Buzzi O., Pedroso D.M., Giacomini A. 2008. Caveats on the Implementation of the Generalized Material Point Method. *Computer Modeling in Engineering and Sciences*, **1**(1), 1-21.

Cheng Y.T., Cheng C.M. 2004. Scaling, dimensional analysis, and indentation measurements. *Materials Science and Engineering R*, **44**,91-149.

Cho J.W., Kima H., Jeon S., Min K.B. 2012. Deformation and strength anisotropy of Asan gneiss, Boryeong shale, and Yeoncheon schist. *International Journal of Rock Mechanics and Mining Sciences*, **50**, 158-169.

Coetzee C.J., Vermeer P.A., Basson A.H. 2005. The modelling of anchors using the material point method. *International Journal for Numerical and Analytical Methods in Geomechanics*, **29**, 879-895.

Dao M., Chollacoop N., Van Vliet K.J., Venkatesh T.A., Suresh S. 2001. Computational modelling of the forward and reverse problems in instrumented sharp indentation. *Acta materials*, **49**, 3899-3918.

Diederichs M.S., Kaiser P.K., Martin C.D. 2000. The use of discrete element simulation to illuminate brittle rock failure process. In Proceedings of the 53rd Canadian Geotechnical Conference, Montreal, Canada, 447-454.

Diederichs M.S. 2007. Mechanistic interpretation and practical application of damage and spalling prediction criteria for deep tunnelling. *Canadian Geotechnical Journal*, **44**(9), 1082-

1116.

Esterhuizen G.S., Dolinar D.R., Ellenberger J.L. 2011. Pillar strength in underground stone mines in the United States. *International Journal of Rock Mechanics and Mining Sciences*, **48**, 42-50.

Ewy R.T., Bovberg C.A., Stankovic R.J. 2010. Strength anisotropy of mudstones and shales. 44^{th} US Rock Mechanics Symposium and 5^{th} U.S.-Canada Rock Mechanics Symposium, held in Salt Lake City, UT June 27-30.

Goodarzi M., Rouainia M., Aplin A.C. 2016. Numerical evaluation of mean-field homogenisation methods for predicting shale elastic response. *Computational Geoscience*.

Goodarzi M., Rouainia M., Aplin A.C. Cubillas P., de Block M. 2017. Predicting the elastic response of organic-rich shale using nanoscale measurements and homogenisation methods. *Geophysical Prospecting*.

Goodarzi M., Rouainia M. 2017. Modelling slope failure using a quasi-static MPM with a non-local strain softening approach. *Procedia Engineering*, **175**, 220-225.

Guo W.C., Rauchs G., Zhang W.H., Ponthot J.P. 2010. Influence of friction in material characterization in microindentation measurement. *Journal of Computational and Applied Mathematics*, **234**, 2183-2192.

Hajiabdolmajid V.R., Kaiser P.K., Martin C.D. 2002 Modelling brittle failure of rock. *International Journal of Rock Mechanics and Mining Sciences*, **39**, 731-741.

Hajiabdolmajid V.R., Kaiser P.K., Martin C.D. 2003. Mobilised strength components in brittle failure of rock. *Geotechnique*, **53**(3), 327-336.

Hamed F.M., 2014. Formulation of a dynamic Material Point Method and applications to soil–water–geotextile Systems. Ph.D. Thesis, University of Stuttgart.

Hoek E., Brown E.T. 1980. Underground excavations in Rock. London: Institution of Mining and Metallurgy.

Hu Y., Randolph M.F. 1998. A practical numerical approach for large deformation problems in soil. *International Journal for Numerical and Analytical Methods in Geomechanics*, **22**, 327-350.

Hustruild W.A. 1976. Review of coal pillar strength formulas. *Rock Mechanics and Rock Engineering*, **8**(2), 115-145.

Jackson R., Lau J.S.O. 1990. The effect of specimen size on the laboratory mechanical properties of Lac du Bonnet grey granite. in: Cunha AP, editor. Scale effects in rock masses, 165–174.

Kumar V. 2012. Geomechanical Characterization of Shale Using Nano-indentation. MSc dissertation, University of Oklahoma.

Kumar V., Sondergeld C.H., Rai C.S., 2012. Nano to macro mechanical characterization of shale. SPE Annual technical conference and exhibition, San Antonio, Texas, USA. SPE 159804.

Lee J.H., Kim T., Lee H. 2010. A study on robust indentation techniques to evaluate elastic–plastic properties of metals. *International Journal of Solids and Structures*, **47**, 647-664.

Lemos L.J.L., Vaughan P.R. 2000. Clay-interface shear resistance. *Geotechnique*, **50**(1), 55-64.

Li S., Hao W., Liu W.K. 2000. Mesh-free simulations of shear banding in large deformation. *International Journal of Solids and Structures*, **37**, 7185-7206.

Liang S.,Weiqun L., Cuijun J., Haonan L. 2011. Constitutive model of scale effects in uniaxial compression for gas-saturated coal. *Procedia Engineering*, **26**, 166-172.

Liang W., Zhang C., Gao H., Yang X., Xu S., Zhao Y. 2012. Experiments on mechanical properties of salt rocks under cyclic loading. *Journal of Rock Mechanics and Geotechnical Engineering*, **4**(1), 54-61.

Lin J., Xie S.Y., Shao J.F., Kondo D. 2012. A micromechanical modeling of ductile behavior of a porous chalk: Formulation, identification, and validation. *International Journal for Numerical and Analytical Methods in Geomechanics*, **36**, 1245-1263.

Littleton I. 1976. An experimental study on the adhesion between clay and steel. *Journal of Terramechanics*, **13**(3), 141-152.

Ma S., Zhang X., Qiu X.M. 2009. Comparison study of MPM and SPH in modeling hypervelocity impact problems. *International Journal of Impact Engineering*, **36**, 272-282.

Magnenet V., Auvray C., Djordem S., Homand F. 2009. On the estimation of elastoplastic properties of rocks by indentation tests. *International Journal of Rock Mechanics and Mining Sciences*, **46**, 635-642.

Magnenet V., Giraud A., Homand F. 2008. Parameter sensitivity analysis for a Drücker–Prager model following from numerical simulations of indentation tests. *Computational Materials Science*, **44**, 385-391.

Meier T., Ryback E., Reinicke A., Dresen G. 2013. Influence of borehole diameter on the formation of borehole breakouts in black shale. *International Journal of Rock Mechanics and Mining Sciences*, **62**, 74-85.

Meier T., Ryback E., Backers T., Dresen G. 2015. Influence of Bedding Angle on Borehole Stability: A Laboratory Investigation of Transverse Isotropic Oil Shale. *Rock Mechanics and Rock Engineering*, **48**(4), 1535-1546.

Min L., Wei-min C., Nai-gang L., Ling-Dong W. 2004. A numerical study of indentation using indenters of different geometry. *Journal of Material Research*, **19**(1), 73-78.

Narin J.A., Guilkey J.E. 2015. Axisymmetric form of the generalized interpolation material point method. *International Journal of Numerical Methods in Engineering*, **101**, 127-147.

Nazem M., Sheng D., Carter J.P. 2006. Stress integration and mesh refinement in numerical solutions to large deformations in geomechanics. *International Journal for Numerical Methods in Engineering*, **65**, 1002-1027.

Nazem M., Sheng D., Carter J.P., Sloan S.W. 2008. Arbitrary-Lagrangian-Eulerian method for large-deformation consolidation problems. *International Journal for Numerical and Analytical Methods in Geomechanics*, **32**, 1023-1050.

Qiu G., Henke S., Grabe J. 2010. Application of a Coupled Eulerian-Lagrangian approach on geomechanical problems involving large deformations. *Computers and Geotechnics*, **38**, 30-39.

Rauchs G., Bradon J. 2011. Identification of elasto-viscoplastic material parameters by indentation testing and combined finite element modelling and numerical optimization. *Finite Elements in Analysis and Design*, **47**, 653-667.

Rojat F., Labiouse V., Kaiser P.K., Descoeudres F. 2009. Brittle Rock Failure in the Steg Lateral Adit of the Lotschberg Base Tunnel. *Rock Mechanics and Rock Engineering*, **42**, 341-359.

Rybacki E., Reinicke A., Meier T., Makasi M., Dresen G. 2015. What controls the mechanical properties of shale rocks? - Part I: Strength and Young's modulus. *Journal of Petroleum Science and Engineering*, **135**, 702-722.

Sarris E., Constantinides G. 2013. Finite element modeling of nanoindentation on C-S-H: Effect of pile-up and contact friction. *Cement and Concrete Composites*, **36**, 78-84.

Seltzer R., Cisilino A.P., Frontini P.M., Mai Y.W. 2011. Determination of the Drucker–Prager parameters of polymers exhibiting pressure-sensitive plastic behaviour by depth-sensing indentation. *International Journal of Mechanical Sciences*, **53**, 471-478.

Shen W.Q., Shao J.F., Kondo D., Gatmiri B. 2012. A micro-macro model for clayey rocks with a plastic compressible porous matrix. *International Journal of Plasticity*, **36**, 64-85.

Shen W.Q., Kondo D., Dormieux L., Shao J.F. 2013. A closed-form three scale model for ductile rocks with a plastically compressible porous matrix. *Mechanics of Materials*, **59**, 73-86.

Steffen M., Kirby R.M. erzins M. 2008. Analysis and reduction of guadratic errors in the Material Point Method (MPM). *International Journal of Numerical Methods in Engineering*, **76**(6), 922-948.

Solowski W.T., Sloan S.W. 2015. Evaluation of material point method for use in geotechnics. *International Journal for Numerical and Analytical Methods in Geomechanics*, **39**, 685-701.

Sulsky D., Chen Z., Schreyer H.L. 1994. A particle method for history–dependent materials. *Computer Methods in Applied Mechanics and Engineering*, **118**, 179-196.

Sulsky D., Schreyer H.L., 1996. Axisymmetric form of the material point method with applications to upsetting and Taylor impact problems. *Computer Methods in Applied Mechanics and Engineering*, **139**, 409-429.

Tho K.K., Swaddiwudhipong S., Liu Z.S., Zeng K., Hua J. 2004. Uniqueness of reverse analysis from conical indentation tests. *Journal of Material Research*, **19**(8), 2498-2502.

Thuro K., Plinninger R.J., Zah S., Shultz S. 2001. Scale effect in rock strength properties, part 1: Unconfined compressive test and Brazilian test. In: Sarkka P, Eloranta J, editors. Rock mechanics - a challenge for society, 169–174.

Ulm F.J., Abousleiman Y. 2006. The nanogranular nature of shale. *Acta Geotechnica*, **1**, 77-88.

Yang S.Q., Ranjith P.G., Haung Y.H., Yin P.F., Jing H.W., Gui Y.L. 2015. Experimental investigation on mechanical damage characteristics of sandstone under triaxial cyclic loading. *Geophysical Journal International*, **201**(2), 662-682.

Zhang Q., Zhu H., Zhang L., Ding X. 2011. Study of scale effect on intact rock strength using particle flow modeling. *International Journal of Rock Mechanics and Mining Sciences*, **48**, 1320-1328.

Chapter 6

Summary and conclusion

6.1 Key results

This thesis is a comprehensive evaluation of the alternative approaches of core scale testing for quantifying the mechanical behaviour of shale rocks. In the past decades, large studies has been directed at use of the indentation test and micromechanical modelling, as alternative methods in predicting the elastic response of shale rocks. Usually, in these studies, the methods are carried out on a couple of shale samples and relatively good results are reported. However, very limited discussions on the applicability and limitation of these methods are provided. It is also not clearly stated, whether these methods can be generally used in different shale rocks. For instance, the wide variation in the proposed micromechanical modelling could further support the idea that there is no unique and generalized approach. The variability in the mechanical properties of clay particles, organic matter and their role in shale microstructure add more complexity to the use of micromechanical modelling. In addition, the majority of the studies are focused on elastic response and not much attention was paid to the elastoplastic behaviour. Here, both small scale testings on shale cuttings and micromechanical modelling were studied, and the key results and findings will be reported in the following.

At first, the mechanical response of each constituent inside the shale microstructure was investigated. This can provide the essential input data for micromechanical modelling and also gives some insight on the origin of macroscopic behaviours. The PeakForce QNM® as a non-destructive test with a resolution of a few nanometres was adopted in order to directly measure the elastic response of the clay matrix, silt grains and organic matter. Through this part of the study, some key findings have been achieved. In order to have a reliable correlation between mechanical measurement and the different constituents, nanomechanical mapping can be combined with imaging techniques such as SEM, using back scattered electron (BSE) imaging, chemical analyses using energy dispersive spectrometry (EDS), and topographical map. Measurement over the silt inclusions showed that these constituents are almost isotropic in elastic response. The clay matrix on the other hand showed significant anisotropy in the scale of a few nanometers. The ratio of this anisotropy is comparable with the data obtained on core samples. These findings confirmed two key points. First, the widely used assumption of isotropic elastic silt inclusions in micromechanical modeling was validated using direct measurement. Second, it was observed that the clay matrix is the main source of anisotropy in shale rocks. This further emphasizes that assuming spherical shape for silt inclusions is acceptable, as they do not significantly influence the macroscopic anisotropy of shales.

In the next step, the organic matter was the target of nanomechanical mapping. The measurements were conducted on two shale samples with different thermal maturity levels. It was found that a stiff silicon nitride tip, which is inexpensive compared to a diamond tip, is suitable for nanomechanical measurement on organic matter, being relatively sharp and having a suitable range of measurement for this constituent. It was not possible to target kerogen, as this phase is deeply mixed within the clay matrix. Therefore, statistical analysis was performed on the whole data set to extract the values of elastic modulus related to kerogen. Considering a Poisson's ratio of 0.3, two values of 5.9 and 10.35 GPa were determined for immature and mature kerogen respectively, in Posidonia shale samples. These values could be critical input data for homogenisation methods.

Although the indentation test has been used on shale samples in a small number of studies, the reliability of this method for the case of shale rocks, has not yet been investigated. There are several factors involved in this test, such as tip geometry, loading-unloading rate and holding time at the maximum penetration or load, whose effects on the results should be evaluated. The time-dependent response of shale rocks could raise concerns regarding the influence of these parameters in the indentation test. Two different tips, spherical and sharp Berkovich, were adopted in this study. Different loading-unloading rates were also selected. Based on the results, some key points can be highlighted.

The indentation test was shown to be a robust experiments to estimate the elastic modulus of shale samples and could clearly quantify the level of anisotropy, however, some issues were observed when the stiffness of the sample increases. For shales with indentation modulus above 30 GPa, the standard deviation of the measured data increased significantly. This is partly because of stiffer samples, for which the penetration depth is smaller under the same maximum load, which consequently reduces the contact area. This means that, the volume of the shale microstructure affected by each indent is reduced and the chance of recording uniform and representative behaviour is less. SEM imaging also shows that, in one of the stiff samples, the size of the silt inclusions are as big as 20 μm which is comparable with the contact area in this sample. In fact, such big grains hinder accurate measurement over the whole shale microstructure. As a maximum force of 500 mN was selected here, which is even higher than the reported maximum force in the literature (400 mN), these observations could provide a better understanding on the range of applicability of current indentation machines for shale rocks.

Regarding time-dependent behaviour, two samples with the same clay content but different organic matter content showed highly different creep responses. This observation clarifies that the creep behavior is controlled by both clay and TOC. The amount of creep deformation was plotted against clay+TOC content, and the same nonlinear correlation that was reported on core samples was observed. Conducting the creep test in both directions for one of the samples also revealed that the level of anisotropy for creep response was almost identical to the elastic anisotropy. In addition, it was observed that the elastic response is almost independent of the time-dependent behaviour (loading/unloading rate). This is important as it allows for determination of creep behaviour and elastic properties simultaneously.

After two levels of experimental studies on shale cuttings, micromechanical modelling was studied as a theoretical mathematical-based approach towards shale characterisation. In summary, Chapter 2 provides some information, such as elastic properties of organic matters, as input data for this mathematical modelling and the indentation data obtained in Chapter 3 can be used to validated the predicted mechanical response for shale by these formulations.

First, attention was paid to evaluating the theoretical capability of some of these formulations. A comprehensive numerical modelling of virtual and simplified shale microstructures was conducted in order to provide an understanding of the limitations and the range of applicability of different homogenisation formulations. Some key observations can be mentioned regarding the micromechanical modelling. Combining the results from virtual microstructures with the experimental observations, it was concluded that the Self-Consistent Scheme is a suitable method to homogenise the elastic response of porous clay. In the second level of shale microstructure, where the silt inclusions are mixed within the porous clay matrix, both the Self-Consistent Scheme and the Mori-Tanaka method, provide relatively close predictions to the numerical results. However, it was observed that by increase in the inclusion volume fractions the prediction error grows, and a limit of 40% can be suggested for the range of applicability of MT and SCS. The mentioned observations have been proven by using a homogenisation technique to predict some shale elastic properties available in the literature, and also the data set generated in this study in Chapter 3. A key point in the proposed formulation is that clay particles were assumed to be intrinsically anisotropic to reproduce shale anisotropy and kerogen was also mixed within the porous clay matrix similar to pores. In addition, it was shown that the use of the measured kerogen modulus in this study (5.9 GPa), in the homogenisation method can result in much better prediction of the macroscopic elastic properties than adopting the proposed value in the literature (8 GPa). In general, it can be concluded that relatively good predictions can be obtained by this micromechanical modelling, provided that shale's composition is well characterised and suitable formulations are used. It should be noted that different complexities such as shape effect for silts, kerogen and pores can be simply added to the homogenisation formulation in order to improve the predicted results.

In the final stage of this study, the attention was paid to the feasibility of extracting elasto-plastic behaviour of shales using indentation test. The idea is based on numerical simulation of indentation test and back-calculation of the plasticity parameters by fitting numerical load-displacement curve with the experimental one. A robust numerical tool is required in order to simulate the large penetration problem of indentation, which is not simply possible by using conventional mesh-based methods. The Material Point Method known as MPM was programmed and verified for this purpose.

An interesting point regarding the MPM formulation is that it is unconditionally stable in large deformation problems with no issues caused by excessive mesh distortion. However, it should be noted that the MPM computational time is higher than the conventional Finite Element Method. It was also pointed out that the main problem in inverse analysis of indentation test is that the load-displacement curve is not unique for a pressure sensitive material with at least two plasticity parameters. This problem can be solved by using two different tip geometries which is also applied in this study. With two indentation curves, it is possible to uniquely back-calculate the two unknowns of pressure-sensitive material models.

The key observations regarding the inverse analysis results are: for samples with higher stiffness (above 30 GPa), where the penetration depth is smaller, the plastic behaviour is only cohesive and the back-calculated cohesion is too high compared to core scale observations. For the softer sample (with indentation modulus around 14 GPa), where penetration was much greater, both friction and cohesion was mobilised. The value of uniaxial compression strength determined by this technique for the soft sample was quite comparable with the core sample data reported in the literature. Moreover, the simulations revealed that a friction coefficient between indenter and shale sample is required in order to have reasonable results. This value was here selected as 0.2 and 0.3 based on experimental study on clay-metal/glass contact.

These observations are consistent with the theory which states that cohesion in rock is instantly mobilised but some level of damage is required to mobilise the internal friction angle. The high value of cohesion can also be related to the well-known problem of scale effects in rock mechanics. As plastic response is highly controlled by defects in the material, a large volume of rock is required in order to contain enough defects to represent the whole microstructure. To conclude, it can be said that the material volume affected by the indenter in the current indentation machines (maximum force of 500 mN), is not enough to be a representative volume element for plastic behaviour. However, this result showed that the possibility of using inverse analysis of indentation test for elastoplastic characterisation of shale cuttings exists, provided that sufficient level of penetration or load is applied in the tests.

6.2 Future work

During this study, many aspects of both small scale experiments and micromechanical modelling for shale rocks were better clarified. The capability and limitation of PeakForce QNM® and indentation test were deeply studied. Micromechanical modelling was theoretically and practically evaluated. Finally, a sophisticated numerical modelling for the inverse analysis of indentation test on shale samples was conducted. Now in the light of this study, it is possible to suggest some ideas for the future works.

Here, the mechanical measurements have covered two scales of a few nanometers and a few micrometers. We believe this study can be completed by repeating these stages for shale cuttings for which core scale measurements are also available. Indentation results, micromechanical modelling and the inverse analysis can be compared with core scale triaxial or Ultra-sonic Pulse Velocity tests.

It was shown that the elastic properties of organic matter changes with its maturity, and it is very important to use an adequate value for this parameter in micromechanical modelling of organic rich shale. It is of interest to continue the research in this direction and generate a data bank of elastic moduli for organic matter with different composition and thermal maturity.

In addition, it is of interest to study the mechanical behaviour of rocks in their in situ state which includes higher temperature and fully saturated condition. Creep response and kerogen chemical components are well known to be affected by temperature. Clay particle are also sensitive to water saturation. Both conditions are possible to be considered in core scale testing; however, for very small scale experiments, a slight change in temperature, due to artificial heating or the presence of water, could affect the machine calibration significantly. To the best of our knowledge, at the moment the technological issues of this problem are solved and it is possible to conduct both PeakForce QNM® and indentation in high temperature along with indentation testing on submerged samples. It could be highly recommended to conduct these small scale tests under the in situ conditions of shale layers.

Appendix A

Additional matrices for homogenisation formulation

A.1 Hill's tensor

For the case of local and global isotropic behaviour with spherical inclusions, the Hill's tensor is obtained as follows:

$$\mathbb{P}^0_{\mathrm{I_r}} = \frac{\beta_0}{2\mu_0}\mathbb{K} + \frac{\alpha_0}{3\kappa_0}\mathbb{J} \tag{A.1}$$

$$\alpha_0 = \frac{3\kappa_0}{3\kappa_0 + 4\mu_0} \tag{A.2}$$

$$\beta_0 = \frac{6(\kappa_0 + 2\mu_0)}{5(3k_0 + 4\mu_0)} \tag{A.3}$$

where κ_0 and μ_0 are the clay matrix bulk and shear moduli, respectively. $\mathbb{K}$ and $\mathbb{J}$ denote the spherical and deviatoric isotropic operators which are defined as follows:

$$\mathbb{J} = \frac{1}{3} I \times I \tag{A.4}$$

$$\mathbb{K} = \mathbb{I} - \mathbb{J} \tag{A.5}$$

where I and $\mathbb{I}$ are the second and forth order identity tensors, respectively.

For spherical inclusions in a transversely isotropic matrix, the five independent components of Hill's tensor are as followings:

$$\begin{aligned}
P^0_{11} = \frac{1}{16}\int_{-1}^{1} &-(-5C^0_{11}x^4C^0_{33} - 3C^0_{12}x^2C^0_{33} \\
&-3C^0_{12}x^4C^0_{44} + 3C^0_{12}x^4C^0_{33} + 5C^0_{11}x^4C^0_{44} \\
&-10C^0_{11}x^2C^0_{44} + 2x^4(C^0_{13})^2 + 8C^0_{44}x^4C^0_{33} \\
&-6x^4(C^0_{44})^2 + 4C^0_{44}x^4C^0_{13} + 6C^0_{12}x^2C^0_{44} \\
&+5C^0_{11}C^0_{44} + 5C^0_{11}x^2C^0_{33} - 4C^0_{44}x^2C^0_{13} \\
&+6x^2(C^0_{44})^2 - 2x^2(C^0_{13})^2 - 3C^0_{12}C^0_{44})\frac{x^2-1}{D_1}dx
\end{aligned} \tag{A.6}$$

$$\begin{aligned}
P^0_{12} = \frac{1}{16}\int_{-1}^{1} &(C^0_{11}C^0_{44} - 2C^0_{11}x^2C^0_{44} \\
&+C^0_{11}x^2C^0_{33} + C^0_{12}C^0_{44} - 2C^0_{12}x^2C^0_{44} \\
&+C^0_{12}x^2C^0_{33} + C^0_{11}x^4C^0_{44} - C^0_{11}x^4C^0_{33} \\
&+C^0_{12}x^4C^0_{44} - C^0_{12}x^4C^0_{33} - 2x^2(C^0_{44})^2 \\
&+2x^4(C^0_{44})^2 - 4C^0_{44}x^2C^0_{13} + 4C^0_{44}x^4C^0_{13} \\
&-2x^2(C^0_{13})^2 + 2x^4(C^0_{13})^2)\frac{x^2-1}{D_1}dx
\end{aligned} \tag{A.7}$$

$$P^0_{13} = \frac{1}{4}\int_{-1}^{1}(x^2-1)x^2(C^0_{44} + C^0_{13})\frac{1}{D_2}dx \tag{A.8}$$

$$\begin{aligned}
P^0_{44} = \frac{1}{16}\int_{-1}^{1} &(4C^0_{11}x^2C^0_{44} - 8C^0_{44}x^4C^0_{13} \\
&-2x^4(C^0_{13})^2 - C^0_{12}x^4C^0_{33} - 8C^0_{11}x^4C^0_{44} \\
&+3C^0_{11}x^4C^0_{33} + 4C^0_{11}x^4C^0_{13} - 4C^0_{12}x^4C^0_{13} \\
&+2C^0_{12}x^6C^0_{13} - 2C^0_{11}x^6C^0_{13} + C^0_{12}x^6C^0_{11} \\
&-3C^0_{12}x^4C^0_{11} + 3C^0_{12}x^2C^0_{11} - 2C^0_{11}x^2C^0_{13} \\
&+2C^0_{12}x^2C^0_{13} + 8C^0_{44}x^6C^0_{13} - 3C^0_{11}x^6C^0_{33} \\
&+4C^0_{44}x^6C^0_{33} + 4C^0_{11}x^6C^0_{44} + C^0_{12}x^6C^0_{33} \\
&+3x^4(C^0_{11})^2 - x^6(C^0_{11})^2 + 2x^6(C^0_{13})^2 \\
&-3x^2(C^0_{11})^2 + (C^0_{11})^2 - C^0_{12}C^0_{11})\frac{1}{D_1}dx
\end{aligned} \tag{A.9}$$

$$P_{33}^0 = \frac{1}{2}\int_{-1}^{1} x^2(x^2C_{44}^0 - x^2C_{11}^0 + C_{11}^0)\frac{1}{D_2}dx \tag{A.10}$$

where

$$\begin{aligned} D_1 = & -2(C_{11}^0)^2x^4C_{33}^0 + 2(C_{44}^0)^2x^6C_{33}^0 - 4(C_{44}^0)^2x^4C_{11}^0 \\ & -3(C_{11}^0)^2x^2C_{44}^0 + (C_{11}^0)^2x^2C_{33}^0 + 2(C_{44}^0)^2x^2C_{11}^0 \\ & -2(C_{13}^0)^2x^4C_{44}^0 - (C_{13}^0)^2x^6C_{11}^0 + 2(C_{13}^0)^2x^4C_{11}^0 \\ & +4(C_{44}^0)^2x^6C_{13}^0 - 2(C_{13}^0)^2x^4C_{12}^0 + 2(C_{13}^0)^2x^6C_{44}^0 \\ & +3(C_{11}^0)^2x^4C_{44}^0 + (C_{13}^0)^2x^6C_{12}^0 - (C_{11}^0)^2x^6C_{44}^0 \\ & +2(C_{44}^0)^2x^6C_{11}^0 + (C_{11}^0)^2x^6C_{33}^0 - (C_{13}^0)^2x^2C_{11}^0 \\ & -4(C_{44}^0)^2x^4C_{13}^0 + (C_{13}^0)^2x^2C_{12}^0 + (C_{11}^0)^2C_{44}^0 \\ & -C_{12}^0C_{11}^0C_{44}^0 - x^6C_{12}^0C_{11}^0C_{33}^0 + 4x^4C_{44}^0C_{11}^0C_{13}^0 \\ & -2x^2C_{11}^0C_{44}^0C_{13}^0 - 4x^4C_{12}^0C_{44}^0C_{13}^0 + 2x^2C_{12}^0C_{44}^0C_{13}^0 \\ & +2x^6C_{12}^0C_{44}^0C_{13}^0 - 2x^6C_{11}^0C_{44}^0C_{13}^0 - 3x^6C_{11}^0C_{44}^0C_{33}^0 \\ & +2x^4C_{12}^0C_{11}^0C_{33}^0 - x^4C_{12}^0C_{44}^0C_{33}^0 - 3x^4C_{12}^0C_{11}^0C_{44}^0 \\ & -x^2C_{12}^0C_{11}^0C_{33}^0 + 3x^2C_{12}^0C_{11}^0C_{44}^0 + 3x^4C_{44}^0C_{11}^0C_{33}^0 \\ & +x^6C_{12}^0C_{11}^0C_{44}^0 + x^6C_{12}^0C_{44}^0C_{33}^0 \end{aligned} \tag{A.11}$$

$$\begin{aligned} D_2 = & 2C_{44}^0x^4C_{13}^0 + C_{44}^0x^4C_{33}^0 + C_{44}^0x^4C_{11}^0 \\ & -2C_{44}^0x^2C_{13}^0 - 2C_{11}^0x^2C_{44}^0 + C_{44}^0C_{11}^0 \\ & +x^4(C_{13}^0)^2 - C_{11}^0x^4C_{33}^0 - x^2(C_{13}^0)^2 + C_{11}^0x^2C_{33}^0 \end{aligned} \tag{A.12}$$

A.2 GSCS' shear modulus

For a composite with isotropic matrix and spherical inclusions, the GSCS shear modulus can be expressed using the following three constants:

$$\begin{aligned} A = & 8(\frac{\mu_i}{\mu_0} - 1)(4 - 5v_0)\eta_1 f_i^{\frac{10}{3}} - 2(63(\frac{\mu_i}{\mu_0} - 1)\eta_2 + 2\eta_1\eta_3)f_i^{\frac{7}{3}} \\ & +252(\frac{\mu_i}{\mu_0} - 1)\eta_2)\eta_2 f_i^{\frac{5}{3}} - 50(\frac{\mu_i}{\mu_0} - 1)(7 - 12v_0 + 8v_0^2)\eta_2 f_i \\ & +4(7 - 10v_0)\eta_2\eta_3 \end{aligned} \tag{A.13}$$

$$B = -4(\frac{\mu_i}{\mu_0} - 1)(1 - 5v_0)\eta_1 f_i^{\frac{10}{3}} + 4(63(\frac{\mu_i}{\mu_0} - 1)\eta_2 + 2\eta_1\eta_3) f_i^{\frac{7}{3}}$$
$$-504(\frac{\mu_i}{\mu_0} - 1)\eta_2)\eta_2 f_i^{\frac{5}{3}} + 150(\frac{\mu_i}{\mu_0} - 1)(3 - v_0)v_0\eta_2 f_i \tag{A.14}$$
$$+3(15v_0 - 7)\eta_2\eta_3$$

$$C = 4(\frac{\mu_i}{\mu_0} - 1)(5v_0 - 7)\eta_1 f_i^{\frac{10}{3}} - 2(63(\frac{\mu_i}{\mu_0} - 1)\eta_2 + 2\eta_1\eta_3) f_i^{\frac{7}{3}}$$
$$+252(\frac{\mu_i}{\mu_0} - 1)\eta_2 f_i^{\frac{5}{3}} + 25(\frac{\mu_i}{\mu_0} - 1)(v_0^2 - 7)\eta_2 f_i \tag{A.15}$$
$$-(7 + 5v_0)\eta_2\eta_3$$

with

$$\eta_1 = (\frac{\mu_i}{\mu_0} - 1)(49 - 50v_i v_0) + 35(\frac{\mu_i}{\mu_0})(v_i - 2v_0) + 35(2v_i - v_0) \tag{A.16}$$

$$\eta_2 = 5v_i(\frac{\mu_i}{\mu_0} - 8) + 7(\mu_i + \mu_0 + 4) \tag{A.17}$$

$$\eta_3 = (\frac{\mu_i}{\mu_0})(8 - 10v_0) + (7 - 5v_0) \tag{A.18}$$

where μ is the shear modulus, v is the Poisson's ratio, f is the volume fraction and the subscripts 0 and i refer to the matrix and inclusions, respectively.

Appendix B

Material Point Method formulations

B.1 Basic formulations of Material Point Method

MPM can be categorized as an Arbitrary Lagrangian Eulerian extension over original FEM formulation. In every step, all state variables on material points are mapped over the arbitrary background computational mesh. The rest of the calculation is the conventional explicit FEM. The new nodal values are then re-mapped on the material points. The arbitrary background mesh can be reset to its original position or a new mesh can be generated. Figure B.1 shows how the particles, in a Lagrangian formulation move through the Eulerian mesh.

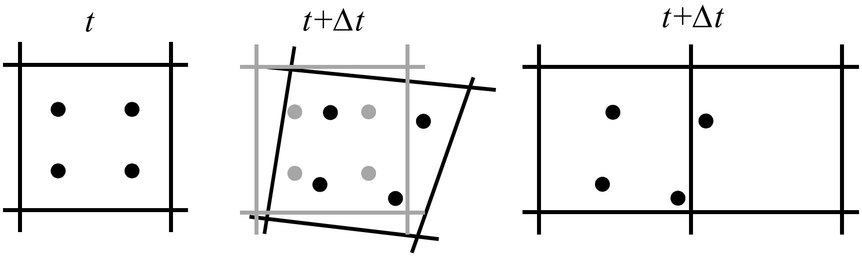

Figure B.1: Description of a continuum using MPM.

Assuming that the particle quantities such as position, mass, external force, volume, velocity, stress and strain $\{\boldsymbol{x}_p^t, M_p, \mathbf{f}_p^t, V_p^t, \mathbf{v}_p^t, \boldsymbol{\sigma}_p^t, \boldsymbol{\varepsilon}_p^t\}$, have been obtained (initialised) at time t, the nodal values for mass and momentum can be obtained as:

$$m_n^t = \sum_{p=1}^{n_p} N_n(\boldsymbol{x}_p^t) M_p; \qquad m_n^t \mathbf{v}_n^t = \sum_{p=1}^{n_p} N_n(\boldsymbol{x}_p^t) M_p \mathbf{v}_p^t \tag{B.1}$$

where N is the shape function which could be the conventional FEM, GIMP or Spline shape functions and n_p is the total number of material points that contribute to the node n.

The nodal external and internal forces follow straightforwardly as:

$$\mathbf{f}_n^{ext,t} = \sum_{p=1}^{n_p} N_n(\boldsymbol{x}_p^t)\mathbf{f}_p^t; \qquad \mathbf{f}_n^{int,t} = -\sum_{p=1}^{n_p} V_p^t \boldsymbol{\sigma}_p^t \nabla N_n(\boldsymbol{x}_p^t) \tag{B.2}$$

where ΔN is the first derivative of the shape functions and $\boldsymbol{\sigma}_p$, in plane strain analysis, has three nonzero components of $\{\sigma_{xx}, \sigma_{yy}, \sigma_{xy}\}$.

The total nodal forces $\mathbf{f}_n^{\text{tot},t} = \mathbf{f}_n^{\text{ext},t} + \mathbf{f}_n^{\text{int},t}$ and nodal momentum are subsequently used in conjunction with the widely used explicit Euler forward time scheme to update the particle velocities at time $t + \Delta t$ as follows:

$$\mathbf{v}_p^{t+\Delta t} = \mathbf{v}_p^t + \Delta t \sum_{n=1}^{n_n} N_n(\boldsymbol{x}_p^t)\mathbf{f}_n^{tot,\text{t}}/m_n^t \tag{B.3}$$

where n_n is the total number of nodes, to them material point p contributes. The nodal velocity will then be updated using the new material points velocity.

$$\mathbf{v}_n^{t+\Delta t} = \sum_{p=1}^{n_p} N_n(\boldsymbol{x}_p^t) M_p \mathbf{v}_p^{t+\Delta t}/m_n^t \tag{B.4}$$

and new particle positions

$$\boldsymbol{x}_p^{t+\Delta t} = \boldsymbol{x}_p^t + \Delta t \sum_{n=1}^{n_n} N_n(\boldsymbol{x}_p^t)\mathbf{v}_n^{t+\Delta t} \tag{B.5}$$

In view of Equation (B.4), the velocity gradient of the particles can be further re-written as:

$$\mathbf{L}_p^{t+\Delta t} = \nabla \mathbf{v}_p^{t+\Delta t} = \sum_{n=1}^{n_n} \nabla N_n(\boldsymbol{x}_p^t)\mathbf{v}_n^{t+\Delta t} \tag{B.6}$$

and the corresponding deformation gradients operators of the finite strain situations can be directly obtained as:

$$\mathbf{F}_p^{t+\Delta t} = (\mathbf{I} + \mathbf{L}_p^{t+\Delta t}\Delta t)\mathbf{F}_p^t \tag{B.7}$$

and the volume changes are updated at the particle level according to:

$$V_p^{t+\Delta t} = det(\mathbf{F}_p^{t+\Delta t})V_p^0 \tag{B.8}$$

To account for large strain condition, the Jaumann stress rate is used to update particle stresses as follows:

$$\boldsymbol{\sigma}_p^{t+\Delta t} = \boldsymbol{\sigma}_p^t + (\boldsymbol{\sigma}_p^t \boldsymbol{\omega}_p^{t+\Delta t} - \boldsymbol{\omega}_p^{t+\Delta t}\boldsymbol{\sigma}_p^t) + \mathbb{D} : \Delta\boldsymbol{\varepsilon}_p^{t+\Delta t} \tag{B.9}$$

$$\Delta\boldsymbol{\varepsilon}_p^{t+\Delta t} = \frac{\Delta t}{2}(\mathbf{L}_p^{t+\Delta t} + (\mathbf{L}_p^{t+\Delta t})^T) \tag{B.10}$$

$$\boldsymbol{\omega}_p^{t+\Delta t} = \frac{\Delta t}{2}(\mathbf{L}_p^{t+\Delta t} - (\mathbf{L}_p^{t+\Delta t})^T) \tag{B.11}$$

where $\Delta\boldsymbol{\varepsilon}_p$ is the incremental linear strain, $\boldsymbol{\omega}_p$ is the rotation matrix and $\mathbb{D}$ is the stiffness tensor related to the constitutive model.

The explicit MPM is inherently a dynamic formulation. In order to adopt this method for the case of quasi-static problem, a damping algorithm is required to reduce the nodal acceleration and force the system to reach to equilibrium. Here, the well-known local damping proposed by Cundall (1987), was adopted for this purpose. In this damping algorithm, a proportion of the total nodal force in the opposite direction of the nodal velocity is added to the total force.

$$\mathbf{f}_n^{damping} = \alpha\,\mathbf{f}_n^{tot}\, sing(\mathbf{v}_n) \tag{B.12}$$

$$sing(\mathbf{v}_n) = \frac{\mathbf{v}_n}{|\mathbf{v}_n|} \tag{B.13}$$

where α is a value between 0 to 1 and called damping coefficient. Low values for this coefficient increase the computational time, as more iterations are required to damp the nodal inertia. However, very high values hinder the force propagation through the medium. Based on author's experience, values around 0.7-0.8 is suitable for most of MPM applications.

The presented formulation can be simply used for both two dimensional plain strain/stress analysis. For axisymmetric condition, some modifications have be considered. The conventional FEM shape functions are applicable in axisymmetric MPM with mixed integration. The particle volume, however, should be re-defined:

$$V_p = R_p A_p \tag{B.14}$$

where A_p is the area of the particle voxel on the 2D plane of the model, which is also equal to the particle volume in plain strain analysis and R_p is the distance of the center of the particle voxel from the axis of symmetry. Moreover, four nonzero stress components contribute to the internal forces which require axisymmetric shape function derivatives. The internal forces in cylindrical coordinates can be calculated as:

$$\boldsymbol{\sigma}_p = \{\sigma_{rr}, \sigma_{zz}, \sigma_{rz}, \sigma_{\theta\theta}\} \tag{B.15}$$

$$(f_r)_n^{int,t} = -\sum_{p=1}^{n_p} V_p^t \left((\boldsymbol{\sigma}_{rr})_p^t \, N_{n,r}(\boldsymbol{x}_p^t) + (\boldsymbol{\sigma}_{rz})_p^t \, N_{n,z}(\boldsymbol{x}_p^t) + (\boldsymbol{\sigma}_{\theta\theta})_p^t \frac{N_n(\boldsymbol{x}_p^t)}{R_p} \right) \tag{B.16}$$

$$(f_z)_n^{int,t} = -\sum_{p=1}^{n_p} V_p^t \left((\boldsymbol{\sigma}_{zz})_p^t \, N_{n,z}(\boldsymbol{x}_p^t) + (\boldsymbol{\sigma}_{zr})_p^t \, N_{n,r}(\boldsymbol{x}_p^t) \right) \tag{B.17}$$

The in-plane strain components in axisymmetric analysis are similar to the ones obtained for plane strain formulation and can be calculated using Eq. B.10. However, the out-plane strain component is not zero and can be determined as following:

$$(\boldsymbol{\varepsilon}_{\theta\theta})_p^{t+\Delta t} = \Delta t \sum_{n=1}^{n_n} \left((v_r)_n^{t+\Delta t} \, \frac{N_n(\boldsymbol{x}_p^t)}{R_p} \right) \tag{B.18}$$

B.2 MPM contact algorithm

The MPM formulation is based on a single-valued velocity field, which means all the bodies are mapped over one computational mesh. This means if two bodies are in contact, they are treated as one body. The calculation over this velocity field automatically satisfies the no-slip and no-penetration conditions, and it is called center-of-mass velocity field ($\mathbf{v}_n$) as its values obtained through a mass weighting procedure given in Eq. B.1. The MPM contact algorithm for no-slip condition starts by adding a separate velocity field for each body (${}^i\mathbf{v}_n$). In order to determine this velocity field, the same weighting procedure is carried out over each body, while ignoring the presence of the other bodies. The ${}^i\mathbf{v}_n$ has to be modified to account for the imposed boundary conditions due to the contact between bodies. The required modifications can be calculated by comparing the field ${}^i\mathbf{v}_n$ with the center-of-mass field. This is called the multi-velocity field-based contact algorithm (Bardenhagen *et al.*, 2000).

The first step in contact algorithms is the contact detection. Two criteria have to be satisfied at any nodes to be considered for contact modification. They only need to be checked over the so-called active nodes which are involved with body i. First the velocity on the active nodes on the field ${}^i\mathbf{v}_n$ are compared with the $\mathbf{v}_n$, to check whether these nodes are mutual between two bodies. If the nodal velocities are different on two fields, the node is called contact node. Second, it should be determined if the two bodies are approaching or separating on the contact nodes. No modification in velocity field ${}^i\mathbf{v}_n$ is required if the bodies are separating. Eq. B.30

and B.20 summarize two criteria for contact node detection.

$$\begin{cases} {}^{i}\mathbf{v}_n = \mathbf{v}_n & No\ modification \\ {}^{i}\mathbf{v}_n \neq \mathbf{v}_n & Contact\ node \end{cases} \tag{B.19}$$

$${}^{i}\mathbf{v}_n \neq \mathbf{v}_n \Rightarrow \begin{cases} ({}^{i}\mathbf{v}_n - \mathbf{v}_n) \cdot {}^{i}\mathbf{n}_n > 0 & Approaching \\ ({}^{i}\mathbf{v}_n - \mathbf{v}_n) \cdot {}^{i}\mathbf{n}_n \leq 0 & Separating \end{cases} \tag{B.20}$$

where ${}^{i}\mathbf{n}_n$ is the unit outward vector normal to the surface of the body i at node n. A good estimation of the surface normal is an important factor on the accuracy of the contact algorithm, as both contact calculation and detection depend on it. Lemiale *et al.* (2010) proposed to use mass-weighted shape function gradient to calculate this normal. Same idea was adopted and modified here with volume-weighted shape function gradient and the particle radius to account for axisymmteric condition.

$${}^{i}\mathbf{n}_n = \frac{\sum\limits_{p=1}^{n_p} V_p \nabla N_n(\boldsymbol{x}_p)/R_p}{\left|\sum\limits_{p=1}^{n_p} V_p \nabla N_n(\boldsymbol{x}_p)/R_p\right|} \tag{B.21}$$

here the summation is performed over the MPs belonging to the body i. It should be noted that for the nodes located on the axis of symmetry, the component of the volume-weighted shape function gradient, which is normal to the axis, should be set to zero. This is a fictitious value produced because of ignoring the other half of the model. Eq. B.21 can also be used for plane strain condition provided that $R_p = 1$.

The explicit nature of MPM formulation allows for handling of the normal and tangential forces on the contact surface, separately. The center-of-mass velocity field prevents penetration; therefore, it is natural choice to change the velocity component normal to the contact surface on contact nodes to the same value derived from $\mathbf{v}_n$. Thus, the new contact nodes' velocity, ${}^{i}\widetilde{\mathbf{v}}_n$, for body i is

$${}^{i}\widetilde{\mathbf{v}}_n \cdot {}^{i}\mathbf{n}_n = \mathbf{v}_n \cdot {}^{i}\mathbf{n}_n \tag{B.22}$$

$${}^{i}\Delta\mathbf{v}_n^{norm} = \left[({}^{i}\mathbf{v}_n - \mathbf{v}_n) \cdot {}^{i}\mathbf{n}_n\right] {}^{i}\mathbf{n}_n \tag{B.23}$$

$${}^{i}\widetilde{\mathbf{v}}_n = {}^{i}\mathbf{v}_n -{}^{i} \Delta\mathbf{v}_n^{norm} \tag{B.24}$$

where the ${}^i\Delta\mathbf{v}_n^{norm}$ is the component of the difference between velocity field of a single body and the center-of-mass velocity field being normal to the contact surface.

If the contact is frictionless, no more modification is required. However, in case of frictional contact, the ${}^i\Delta\mathbf{v}_n^{norm}$ should be converted to its equivalent normal contact force (Eq. B.25). This force is then used to calculate the frictional force in the contact.

$$
{}^i\mathbf{f}_n^{norm} = -\frac{m_n}{\Delta t}\ {}^i\Delta\mathbf{v}_n^{norm} \tag{B.25}
$$

The tangential component of ${}^i\mathbf{v}_n - \mathbf{v}_n$ and its equivalent tangential contact force can be obtained as followings:

$$
{}^i\Delta\mathbf{v}_n^{tang} = \left({}^i\mathbf{v}_n - \mathbf{v}_n\right) - {}^i\Delta\mathbf{v}_n^{norm} \tag{B.26}
$$

$$
{}^i\mathbf{f}_n^{tang} = -\frac{m_n}{\Delta t}\ {}^i\Delta\mathbf{v}_n^{tang} \tag{B.27}
$$

In Coulomb friction model, the tangential force cannot exceed the friction force, so the maximum allowed magnitude of tangential force and its proportional tangential velocity are:

$$
\left|{}^i\mathbf{f}_n^{tmax}\right| = -\mu\ \left|{}^i\mathbf{f}_n^{norm}\right| \tag{B.28}
$$

$$
\Delta{}^i\mathbf{v}_n^{tmax} = \mu\ \left[\left({}^i\mathbf{v}_n - \mathbf{v}_n\right)\cdot{}^i\mathbf{n}_n\right]\ \frac{{}^i\Delta\mathbf{v}_n^{tang}}{\left|{}^i\Delta\mathbf{v}_n^{tang}\right|} \tag{B.29}
$$

where μ is the friction coefficient along the contact. The velocity field for body i can then be updated as follow:

$$
\begin{cases}
{}^i\widetilde{\mathbf{v}}_n = {}^i\mathbf{v}_n - \Delta{}^i\mathbf{v}_n^{norm} - \Delta{}^i\mathbf{v}_n^{tang} & \left|{}^i\mathbf{f}_n^{tang}\right| \leq \left|{}^i\mathbf{f}_n^{tmax}\right| \\
{}^i\widetilde{\mathbf{v}}_n = {}^i\mathbf{v}_n - \Delta{}^i\mathbf{v}_n^{norm} - \Delta{}^i\mathbf{v}_n^{tmax} & \left|{}^i\mathbf{f}_n^{tang}\right| > \left|{}^i\mathbf{f}_n^{tmax}\right|
\end{cases} \tag{B.30}
$$

It is quite straightforward to modify this algorithm to account for cohesive contact, or when the shear stress along the contact is limited to the material's maximum shear stress, such as in undrained clay (Ma *et al.*, 2014).

References

Bardenhagen S.G., Brackbill J.U., Sulsky D. 2000. The material-point method for granular materials. *Computer methods in applied mechanics and engineering*, **187**, 529-541.

Cundall P.A. 1987. Distinct element models of rock and soil structure. In Analytical and Computational Methods in Engineering Rock Mechanics, Allen and Unwin, London, 129–163.

Lemiale V., Nairn J., Hurmane A. 2010. Material Point Method simulation of equal channel angular pressing involving large plastic strain and contact through sharp corners. *Computer Modeling in Engineering and Sciences*, **70**(1), 41-66.

Ma J., Wang D., Randolph M.F. 2014. A new contact algorithm in the material point method for geotechnical simulations. *International Journal for Numerical and Analytical Methods in Geomechanics*, **38**(11), 1197-1210.